Cosmogenic ^{3}He in terrestrial rocks: a review

P.-H. Blard*

CRPG, CNRS, Université de Lorraine, 54000, Nancy, France

*Email: blard@crpg.cnrs-nancy.fr

17,500 words

19 figures

1 Table

3 Supplementary Tables:

- Supp. Table 1: Magmatic ^{4}He concentrations database https://doi.org/10.24396/ORDAR-89

- Supp. Table 2: Excel spreadsheet for computing radiogenic ^{4}He and nucleogenic ^{3}He https://doi.org/10.24396/ORDAR-90

- Supp. Table 3: ^{3}He/^{10}Be cross-calibrated production rates database https://doi.org/10.24396/ORDAR-91

Keywords: cosmogenic ^{3}He; magmatic ^{3}He; isochrons; exposure age; production rates; ^{3}He/^{10}Be cross-calibration

Abstract

This review article summarizes the state of the art of cosmogenic ^{3}He (^{3}He$_c$), with a focus on the most efficient methods and strategies for measuring this cosmogenic noble gas in the terrestrial minerals. Our ability to accurately and precisely measure cosmogenic ^{3}He in minerals is mainly constrained by the level of the non-cosmogenic ^{3}He background (i.e., magmatic, radiogenic, nucleogenic, and atmospheric ^{3}He), and thus by the geological characteristics of the samples. Constructing ^{3}He vs ^{4}He isochrons by analyzing several aliquots from the same surface sample constitutes a useful and overlooked method. Isochrons can be applied to mineral samples with homogeneous radiogenic ^{4}He concentration and variable magmatic helium concentrations. This method also allows the direct and joint determination of the cosmogenic ^{3}He concentration and the magmatic ^{3}He/^{4}He ratio, precluding the often-complicated step of vacuum crushing. I perform numerical modeling to explore the impact of the non-cosmogenic ^{3}He components on the final uncertainties and detection limits of ^{3}He$_c$ measurement. Reducing the magmatic component by selecting phenocrysts in the 100–500 μm size fraction improves the precision of cosmogenic ^{3}He analyses. Moreover, it is important to measure U, Th, and Li concentrations in the analyzed minerals and their host rocks to ensure proper corrections for radiogenic ^{4}He and nucleogenic ^{3}He, improving both the accuracy and precision of the method. I discuss the most important aspects of analytical techniques, including the key parameters of noble gas mass spectrometry that result in accurate and precise helium isotopic measurements.

I also review ^{3}He$_c$ production rates and their spatial variability: the global database of absolute calibration sites yields a world-wide average ^{3}He$_c$ production rate in olivine and pyroxene of 124 ± 11 at g^{-1} yr^{-1} using the LSD scaling and the online CREp calculator (https://crep.otelo.univ-lorraine.fr/#/). Cross-calibrations against ^{10}Be indicate that the ratio of the production rate of ^{3}He$_c$ in olivine/pyroxene to that of ^{10}Be in quartz is 33 ± 2 and increases by less than 7% between sea level and 5,000 m elevation. This important observation demonstrates that ^{3}He in olivine/pyroxene and ^{10}Be in quartz are accurately scaled with existing models and can hence be considered as synchronized chronometers. However, ^{3}He$_c$/^{10}Be cross-calibrations based on ^{3}He$_c$ in accessory minerals (zircon, garnet, kyanite, apatite) yield unexpectedly high ^{3}He/^{10}Be production ratios of 40–60 above 3,000 m elevation. As the capture of cosmogenic thermal neutrons by ^{6}Li is unlikely to explain this excess, other mechanisms are required, such as ^{3}He$_c$ inherited from previous exposure episodes, unrecognized specific reaction pathways, or the impact of snow cover. New cross-calibration data obtained by

67   measuring ^3He_c against other cosmogenic nuclides (^{14}C, ^{36}Cl, ^{21}Ne, ^{53}Mn) in different settings

68   will advance our understanding of cosmogenic nuclide production rates and improve the

69   accuracy and precision of applications relying on cosmogenic ^3He. Other improvements could

70   extend the applicability of the ^3He geoscientific toolbox; for example, coupling ^3He with

71   radioactive cosmogenic nuclides (^{10}Be, ^{14}C, ^{36}Cl, ^{53}Mn) will allow paleoaltimetry or the

72   determination of burial ages or paleo-depths in intermediate and mafic terrains.

73

74

Contents

1. Introduction

In-situ cosmogenic nuclides are nuclides in rocks and minerals that are produced through nuclear reactions upon bombardment by high energy (>1 MeV) cosmic particles. Because cosmogenic nuclide concentrations in minerals depend on the amount of time the minerals were exposed at Earth's surface, they represent a powerful and wide array of geochronometric tools with applications in geomorphology, paleoclimatology and geohazard analysis (Fig. 1). Although a large body of literature is dedicated to radioactive cosmogenic nuclides (^{10}Be, ^{26}Al, and ^{36}Cl), less attention has been given to cosmogenic noble gases (^{3}He and ^{21}Ne): in 2020, articles relying on cosmogenic ^{3}He and ^{21}Ne only represented 12% and 10%, respectively, of the ~2,700 publications involving any type of in-situ cosmogenic nuclides (source: Web of Science). ^{3}He is nonetheless an interesting alternative to ^{10}Be for quartz-poor lithologies because it is present in measurable concentrations in minerals that are not suited to ^{10}Be or ^{26}Al analyses, such as those in mafic rocks (olivine, pyroxene). ^{3}He is also measurable in accessory minerals in silica-rich lithologies (zircon, apatite, iron oxides). Moreover, because of their nuclear stability, cosmogenic noble gases can, in theory, be used to analyze events that occurred beyond tens of millions of years ago (e.g. Sartégou et al., 2020) and are thus ideal complements to radioactive cosmogenic isotopes, which decay over shorter durations.

Since the discovery of terrestrial cosmogenic ^{3}He more than 30 years ago by Mark Kurz and others (Craig and Poreda, 1986; Kurz, 1986a), significant progress following the pioneer studies of Cerling and Craig (1994) has developed cosmogenic ^{3}He into a pertinent geological probe. Over the last decades, dozens of studies have used cosmogenic ^{3}He to date and quantify a large variety of Earth processes (Figs. 1, 2), such as the timing of volcanic eruptions (e.g. Kurz et al., 1990), fault kinetics (e.g. Fenton et al., 2001), denudation rates (e.g. Puchol et al., 2017), paleoclimatology (e.g. Martin et al., 2018), paleoaltimetry (e.g. Blard et al., 2006a), dating surfaces that are millions of years old (e.g. Margerison et al., 2005), or tsunami hazard analyses (e.g. Ramalho et al., 2015).

The measurement of cosmogenic ^{3}He requires specific facilities and apparatuses that are currently available in several noble gas laboratories worldwide (e.g. Caltech, Pasadena, USA; CRPG, Nancy, France; SUERC, Glasgow, UK; ETH, Zurich, Switzerland; GFZ, Potsdam, Germany; BGC, Berkeley, USA; LDEO, Palisades, USA). However, because not all minerals are suitable for cosmogenic ^{3}He analysis, the reliability of cosmogenic ^{3}He data depends directly on the nature and geological history of the analyzed rocks. Because these methodological aspects have been disseminated in various specialized papers (Blard et al., 2008; Blard and Farley, 2008; Blard and Pik, 2008; Farley et al., 2006; Goehring et al., 2010;

Kurz, 1986a, b; Larsen et al., 2019, 2021; Martin et al., 2017; Protin et al., 2016; Shuster et al., 2004; Trull et al., 1991), this article summarizes the most important theoretical and methodological aspects of cosmogenic ^{3}He analyses by reviewing the current state of the art and the best strategies for accurately and precisely measuring cosmogenic ^{3}He concentrations.

I begin with a short history of the scientific breakthroughs that led to the discovery of terrestrial cosmogenic ^{3}He (^{3}He$_c$), then describe the different sources and production pathways of ^{3}He and ^{4}He in minerals. I then present methodological guidelines about the theoretical and practical aspects of ^{3}He analyses in mafic minerals (olivine and pyroxene), with the objective of attaining the best precision and accuracy. For a given sample, our ability to detect cosmogenic ^{3}He is determined by its non-cosmogenic ^{3}He background, and then by its geological characteristics. I hence perform numerical modeling to explore the impact of these non-cosmogenic ^{3}He components on the total uncertainties. Then, I present the most important aspects of analytical techniques for helium measurements. Finally, I review and discuss our knowledge of the ^{3}He$_c$ production rate and its spatial variability, relying on published calibration sites and cross-calibrations against other cosmogenic nuclides, notably ^{10}Be, ^{36}Cl and ^{21}Ne. I also explore potential new applications based on the coupling of ^{3}He$_c$ with radioactive cosmogenic nuclides (^{10}Be, ^{36}Cl, ^{53}Mn).
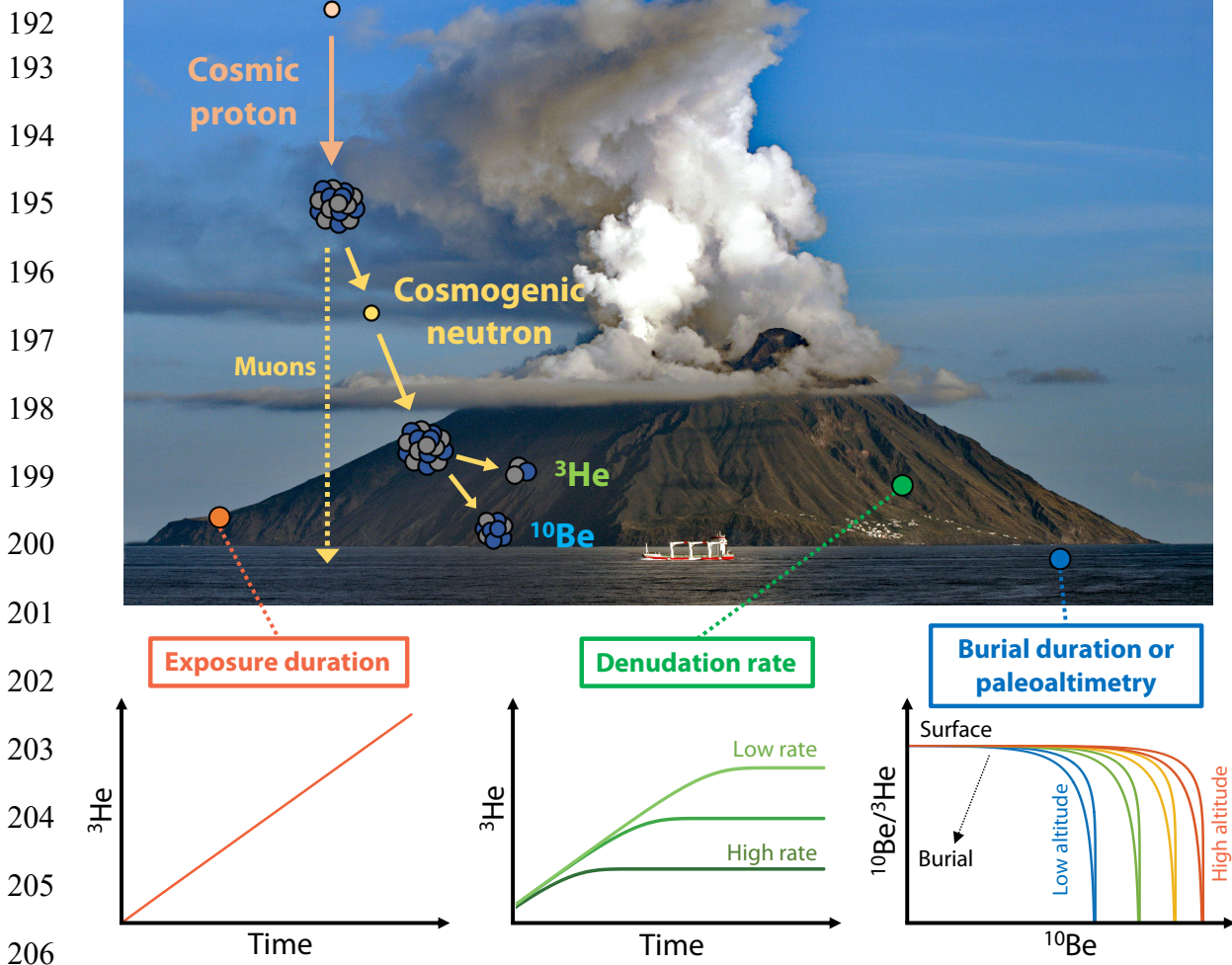
Figure 1. Principles of cosmogenic ^{3}He production and its main applications. ^{3}He$_c$ is produced by spallation reactions induced by high-energy cosmogenic neutrons (> 10 MeV), low-energy cosmogenic neutrons (<1 keV) and muons. The three main applications of cosmogenic ^{3}He are determined by the geomorphological characteristics of the studied objects: 1) on non-eroded surfaces, cosmogenic ^{3}He concentrations measure exposure durations; 2) in eroding landscapes (active versants, rivers) that have reached steady-state (t > $\Lambda/(\rho\varepsilon)$), ^{3}He concentrations measure denudation rates; 3) when coupled with measurements of radioactive cosmogenic nuclides (e.g., ^{10}Be, $t_{1/2}$ = 1.4 Ma) in the same rock sample that is now buried beyond the penetration depth of cosmic particles, it is possible to determine paleoelevations, paleodepths, or measure burial durations. Picture of Stromboli volcano, Italy: © Jcb-caz-11, CC-BY-SA-4.0.

2. Basic concepts of in-situ terrestrial cosmogenic ^{3}He

2.1. Discovery of terrestrial cosmogenic ^{3}He

Until the mid-1980's, the presence of cosmogenic ^{3}He had only been documented in extraterrestrial materials such as lunar samples (e.g., Megrue, 1971) and meteorites (e.g., Fisher, 1972). These analyses were performed by melting samples under vacuum followed by He

224 analyses in a static, high-vacuum Nier-source mass spectrometer (Aldrich and Nier 1946; Kurz

225 1986a). During the 1970's and 1980's, however, noble gas systems switched from glass to fully

226 metal purification lines, lowering instrumental blanks and, hence, detection limits by 5 orders

227 of magnitude, from 10^8 atoms (Megrue 1967) to $<10^3$ atoms on modern instruments (e.g.,

228 Zimmermann et al., 2018).

229   In 1986, Mark Kurz and others demonstrated that cosmogenic ^3He was also detectable

230 in terrestrial rocks by analyzing olivines and pyroxenes from basalt samples exposed for about

231 500 kyr at the summit of Haleakalā volcano, Maui, Hawaii (Kurz, 1986a, 1986b; see also Craig

232 and Poreda, 1986). The compelling evidence for the presence of cosmogenic ^3He resulted from

233 their two-step analysis of He isotopes in olivine phenocrysts: first crushing the olivines in vacuo,

234 then fusing the remaining powder. The fused olivine yielded a $^3He/^4He$ ratio of 2,000 Ra (where

235 Ra = 1.384×10^{-6} is the atmospheric $^3He/^4He$ ratio; Kurz, 1986). Such a high value had never

236 been documented on Earth, as it is far above the highest $^3He/^4He$ ratios measured by crushing

237 mantle olivines, which preferentially release trapped mantellic helium ($^3He/^4He = 8$–30 Ra; e.g.,

238 Parman, 2007). The observed massive ^3He excess was thus interpreted as resulting from the

239 build-up of cosmogenic ^3He in the mantle silicates after they had reached the Earth's surface

240 and been exposed to cosmic rays. Additionally, relying on the fact that magmatic helium has a

241 homogenous isotopic composition in phenocrysts of a few grams, Kurz (1986a, 1986b)

242 proposed that the amount of ^4He released by melting can be used as a proxy for the

243 concentration of magmatic ^3He:

244

245          $$^3He_c = {}^3He_{tot} - {}^4He_{tot} \times ({}^3He/^4He)_{mag} , \qquad\qquad (1)$$

246

247 where $^3He_{tot}$ and $^4He_{tot}$ are the total ^3He and ^4He concentrations, respectively, and $({}^3He/^4He)_{mag}$

248 is the magmatic $^3He/^4He$ ratio estimated from vacuum crushing.

249

250 For decades, this two-step crushing and fusion protocol was used with Equation (1) to correct

251 for the magmatic ^3He component (e.g. Kurz et al., 1990; Licciardi et al., 1999). However,

252 several authors latter proposed that Equation (1) be modified to account for the presence of

253 radiogenic ^4He (Blard and Farley, 2008; Dunai and Wijbrans, 2000) to avoid overestimating

254 the magmatic ^3He contribution (see section 3).

255

256

257

2.2. Advantages and limitations of ^{3}He: an ideal complement to ^{10}Be

During the 1980's, progress in accelerator mass spectrometry (AMS) made it possible to measure in-situ cosmogenic ^{10}Be in hand-sized quartz samples (e.g., Klein et al., 1982; Litherland, 1980; Raisbeck et al., 1987). The nearly simultaneous discovery of cosmogenic ^{3}He in terrestrial samples thus ideally completed the spectrum of applications of these new geochronological tools because ^{3}He is suited to mafic minerals found in volcanic environments, whereas ^{10}Be is suited to silicic, quartz-rich environments. Although cosmogenic ^{3}He is produced in quartz, it is not retained in this mineral at Earth's surface temperatures (see section 2.4).

Moreover, ^{3}He has several specific advantages compared to other cosmogenic nuclides:

i) Because ^{3}He is a light isotope, the cross section of spallation reactions producing cosmogenic ^{3}He are less sensitive to the masses of target elements compared to other nuclides (Dunai, 2010). Consequently, compared to ^{21}Ne, ^{36}Cl, and ^{10}Be, the rate of ^{3}He$_c$ production by high-energy particles (>10 MeV) is less dependent on mineral chemical composition; indeed, empirical data show that olivine and pyroxene have the same ^{3}He$_c$ production rates (Cerling and Craig, 1994; Dunai, 2010; Fenton et al., 2009; Martin et al., 2017). That said, Fe-rich minerals, such as ilmenite and hematite, have lower spallogenic production rates (e.g. Larsen et al., 2019; Shuster et al., 2012), whereas in Li-rich (> 10 ppm) minerals, ^{3}He production may be enhanced by the capture of cosmogenic thermal neutrons (Dunai et al., 2007).

ii) ^{3}He has one of the largest production rate / detection limit ratios, which theoretically enables the detection of exposure episodes shorter than 100 years in the most favorable conditions, i.e. in the case of rocks poor in magmatic helium that erupted less than 10 ka (Niedermann, 2002).

iii) The nuclear stability of ^{3}He allows very old (>10 Ma) surfaces to be dated (e.g. Balter-Kennedy et al., 2020), whereas ^{10}Be and ^{36}Cl reach saturation after only ~5 Myr and ~1 Myr of exposure, respectively. Moreover, ^{3}He may be used to document geological events that occurred in the deep past, such as ancient exposure episodes that occurred several million years ago.

291   Nonetheless, the stability of ^{3}He also somewhat limits its utility: any exposure episode
292 may be recorded by cosmogenic ^{3}He, complicating the interpretation of scenarios with multiple
293 burial-exposure episodes. Moreover, the stability of ^{3}He implies that phenocrysts, especially
294 ones that crystallized several million years ago, may also accumulate significant amounts of
295 ^{3}He through other processes (e.g., Farley et al., 2006). These two properties may be considered
296 the "Achilles' heel" of cosmogenic ^{3}He, and it is fundamental that users take into account the
297 geological context of their samples, and notably the closure (U-Th-Sm)/^{4}He age of the analyzed
298 phenocrysts (see section 3): as closure age increases, so does the minimum measurable
299 exposure age.

300

301 **2.3. A useful geo-chronometer and probe for many applications in Earth surface science**
302   Cosmogenic ^{3}He is now one of the most commonly used cosmogenic nuclides because
303 it can date geological events and quantify numerous surface processes occurring in mafic
304 volcanic environments. Indeed, ^{3}He$_c$ covers a rather wide range of Earth science timescales,
305 from dating historical lava flows (<1 ka; e.g. Heineke et al., 2016) to the oldest known surface
306 exposure ages on Earth's surface (>10 Ma, e.g. Balter-Kennedy et al., 2020).
307   Thus, the questions addressed using cosmogenic ^{3}He have been numerous and intriguing
308 (Fig. 2), ranging from dating volcanic eruptions (e.g. Kurz et al., 1990; Marchetti et al., 2020)
309 reconstructing paleoglaciers dynamics (e.g. Blard et al., 2007; Bromley et al., 2011; Cerling
310 and Craig, 1994; Martin et al., 2018), fault kinematics (e.g. Fenton et al., 2001; Medynski et al.,
311 2016; Ritz et al., 2016), determining fluvial erosion rates (e.g. Ferrier et al., 2013; Litty et al.,
312 2021), and paleoaltimetry (e.g. Blard et al., 2005) to even more exotic and intriguing
313 applications, such as identifying paleo-tsunami deposits (e.g. Ramalho et al., 2015) or dating
314 ancient human footprints (e.g. Heineke et al., 2016).

Figure 2. Geological questions addressed using cosmogenic ^{3}He: (A) dating lava infilling and fault scarps in the Afar rift (Medynski et al., 2016), (B) determining denudation rates in rivers of Santo Antao island, Cabo Verde (Litty et al., 2021), (C) dating 11-ka volcanic ash with preserved human footprints (Heineke et al., 2016), (D) moraine geochronology in the Tropical Andes (Martin et al., 2020), and (E) dating of a giant tsunami 73 ka due to flank collapse on the volcanic island of Fogo, Cabo Verde (Ramalho et al., 2015).

As for any cosmogenic nuclide, the validity and the strength of a cosmogenic ^{3}He data is directly dependent on the quality of the geomorphological analysis and the representativeness of the collected samples. For example, in the case of surface exposure dating, it is essential to minimize the potential erosion or temporal cover. This can be achieved by selecting the flattest and highest surfaces, and by checking for clues of erosion, weathering or ash/soil cover (e.g. Cerling and Craig, 1994). Moreover, several mandatory field observations and sample characteristics must be noted, such as sample location (elevation, altitude, longitude), the topographic shielding (Dunne et al., 1999), sample thickness and density (Gosse and Phillips, 2001; Dunai, 2010). These data are key to computing accurate sample specific production rates, and, hence, consistent exposure ages or erosion rates.

2.4. None like it hot: why is cosmogenic ^{3}He mainly measured in olivines, pyroxenes, iron oxides and accessory minerals?

To record a complete exposure history, cosmogenic nuclides must be quantitatively retained in the mineral of interest. Because of its small size (atomic radius = 31×10^{-12} m), helium has relatively high diffusion rates in silicates: at 15 °C, its diffusivity is $\sim 10^{-14}$ to 10^{-13} cm^2 s^{-1} in quartz (Shuster et al., 2004; Tremblay et al., 2014) and $\sim 10^{-22}$ to 10^{-21} cm^2 s^{-1} in olivine (Blard et al., 2008; Delon et al., 2020). Figure 3 shows the remaining fraction of cosmogenic ^{3}He in 100-μm to 1-cm olivine and quartz grains continuously exposed at Earth's surface. Even if a 1-cm quartz grain is sufficiently large to retain enough ^{3}H$_e$ to record exposure durations up to 10^4 years, ^{3}He$_c$ is not quantitatively retained in submillimetric quartz at typical surface temperatures on Earth (Fig. 3C). This is confirmed by measured cosmogenic ^{3}He concentrations in < 1 mm quartz that are systematically lower than expected from other age constraints (Brook and Kurz, 1993; Cerling, 1990; Trull et al., 1991). Nonetheless, this partial retentivity can be exploited to determine paleotemperatures (Tremblay et al., 2014).

348
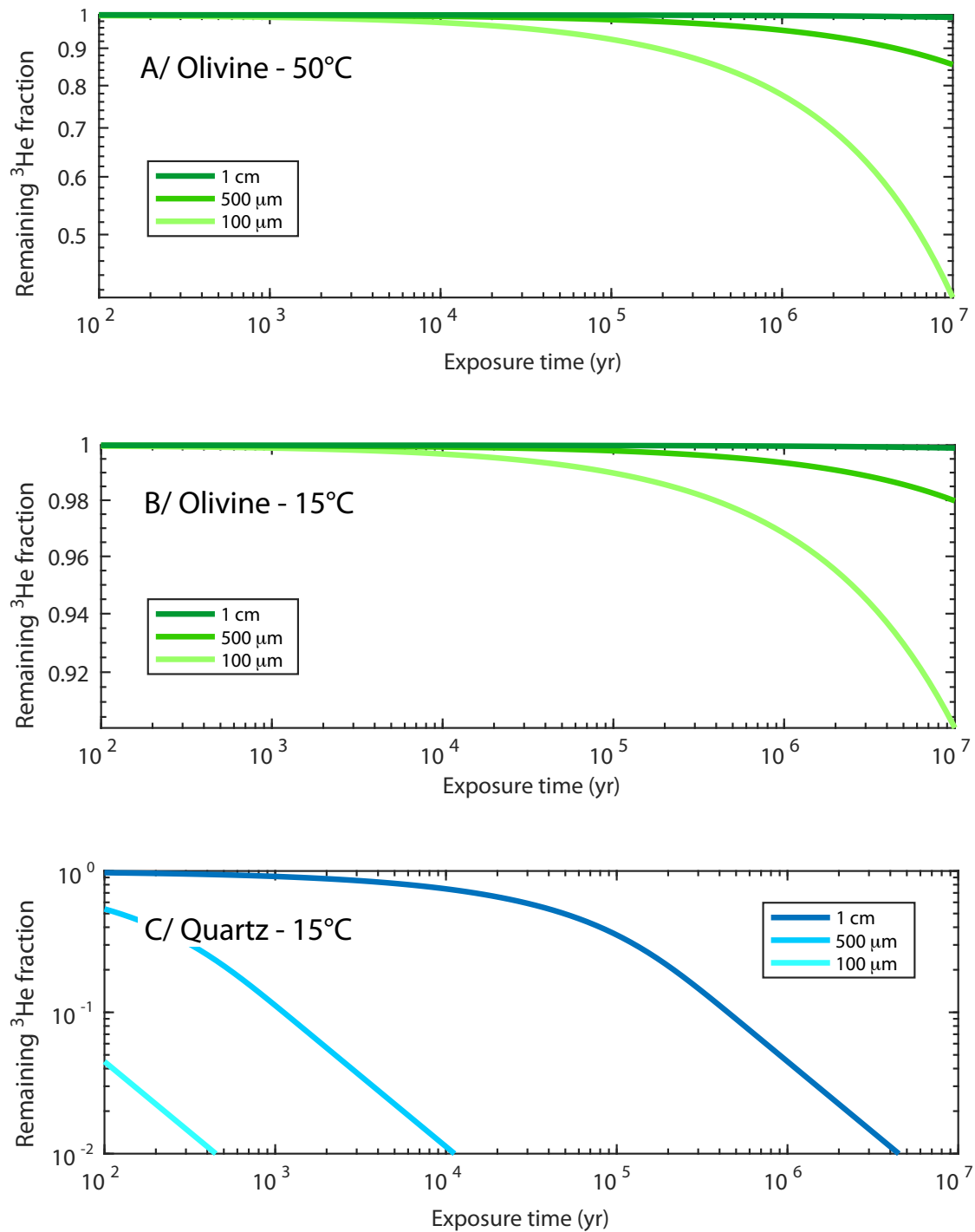
Figure 3. Modeled cosmogenic ^{3}He retention in minerals continuously exposed to cosmic rays: (A) olivine at 50 °C, (B) olivine at 15 °C, and (C) quartz at 15 °C. Note different *y*-axis scales in each plot. These curves were computed by solving the production-diffusion equation for spheres (Wolf et al., 1998) of various diameters (100 μm, 500 μm, and 1 cm). ^{3}He diffusion parameters are from low-temperature (<200 °C) diffusion experiments on quartz (Tremblay et al., 2014) and olivine (Delon et al., 2020).

355

356   In contrast, olivine behaves as a nearly closed system for exposure durations up to 10^5

357   years (Fig. 3A, B): even 100-μm grains continuously exposed at 50 °C lose less than 10% of

358   the ^{3}He produced. However, for exposure or paleoexposure ages older than 10^6 years, mineral

359   sizes and thermal histories should be carefully evaluated to avoid bias due to thermal losses.

360   Other minerals with helium diffusivities low enough to evolve as closed systems over

361   geological timescales at Earth's surface include pyroxene, hematite, magnetite, goethite, zircon,

362   and apatite (Amidon et al., 2008; Blard et al., 2008; Farley, 2018; Kober et al., 2005; Shuster

363   et al., 2012; Vasconcelos et al., 2019). In contrast, calcites demonstrated nearly open system

364   behavior at Earth's surface temperatures at the 10 ka time scale (Amidon et al., 2015; Cherniak

365   et al., 2015). The few available data moreover showed that helium diffusivity varies greatly

366   from a one calcite to another (Amidon et al., 2015).

367   Because olivine and pyroxene have high helium retentivity and are rather abundant in

368   intermediate and mafic rocks (generally 1–10% in andesites and basalts), they are considered

369   to be the most convenient mineral phases for ^{3}He$_c$ analyses, and are thus the most commonly

370   used (e.g. Blard et al., 2006; Bromley et al., 2014; Cerling and Craig, 1994; Goehring et al.,

371   2010; Kurz 1986b; Martin et al., 2017). These phases are also relatively poor in U and Th (<

372   10 ppm, (Blard and Farley, 2008)), and Li (< 10 ppm, (Amidon et al., 2009; Blard et al., 2013)),

373   implying the limited production of radiogenic ^{4}He and nucleogenic ^{3}He, respectively.

374

375

376   3. ^{3}He sources and correcting for non-cosmogenic ^{3}He

377

378   Helium has two stable isotopes: ^{3}He and ^{4}He. ^{3}He is by several order of magnitudes less

379   abundant than ^{4}He. Moreover, the ^{3}He/^{4}He ratio may significantly vary among geological

380   reservoirs. Various natural processes control the incorporation and production of ^{3}He and ^{4}He

381   in terrestrial minerals such as olivine and pyroxene (Fig. 4). It is thus fundamental to understand

382   the budgets of these isotopes to ensure accurate and precise estimates of cosmogenic ^{3}He

383   concentrations in minerals. Thus, in this section, I describe the different production pathways

384   of He isotopes and the most suited strategies to correct for non-cosmogenic ^{3}He sources. These

385   strategies are valid for measuring cosmogenic ^{3}He in any type of mineral sample, whatever the

386   application (dating surfaces, measuring erosion rates or burial ages; Fig. 1).

387

388

389

3.1. The global ^{3}He and ^{4}He budgets in terrestrial minerals

In terrestrial minerals, cosmogenic ^{3}He is mainly produced by spallation reactions involving high-energy (>1 MeV) cosmic particles (Lal 1987), but also by low-energy (<1 keV) thermal cosmogenic neutrons through ^{6}Li(n,α)^{3}He reactions (Dunai et al., 2007) and muons (Larsen et al., 2021; Nesterenok and Yakubovich 2016). These processes produce equivalent amounts of ^{3}He and ^{3}H, but because ^{3}H decays into ^{3}He with a half-life of 12 years, secular equilibrium can be assumed at the geological timescale, and the production of ^{3}H can be taken as that of ^{3}He (Lal, 1987). For simplicity, I hereafter assume that ^{3}He$_c$ includes all these "cosmogenic" production pathways.

^{3}He$_c$ is produced at a rate of about 125 at g^{-1} yr^{-1} at sea level and high latitude (Martin et al., 2017) and this rate increases with elevation, reaching ~2,500 at^{-1} g^{-1} yr^{-1} at 4,000 m elevation and high latitudes (Lal, 1991; Stone, 2000). Hence, geomorphological materials exposed at Earth's surface for 10^3 -10^6 years have ^{3}He$_c$ concentrations in the range of 10^5 to 10^9 at.g^{-1}. Modern analytical systems connected to the most recent Nier-source mass spectrometers (see sections 2.1 and 4) can measure such ^{3}He concentrations to an analytical precision of a few percent in mineral samples of ~10 mg to ~1 g. Nonetheless, the minimum detectable concentration of cosmogenic ^{3}He in a particular sample is determined by our ability to accurately and precisely determine the non-cosmogenic ^{3}He contributions in that sample, which become increasingly difficult as the He closure age of a mineral increases.

^{3}He has four known origins in minerals, each contributing variable ^{3}He concentrations (Fig. 4; Table 1):

i) Cosmogenic ^{3}He (^{3}He$_c$) is hosted in the matrix and its concentration increases with exposure age;

ii) Magmatic inherited ^{3}He (^{3}He$_{mag}$) is hosted in fluid/melt inclusions and the matrix, and its concentration is independent of time;

iii) Nucleogenic ^{3}He (^{3}He$_{nuc}$) is produced by neutron capture in ^{6}Li nuclei and their subsequent disintegration, is matrix-hosted, and its concentration increases with closure age (eruption and closure ages are similar in the case of volcanic rocks), and;

iv) Atmospheric ^{3}He (^{3}He$_{atm}$) is present as a contaminant on the surfaces of analyzed silicates and its concentration is time-independent.

423   In contrast, ^{4}He is 10^6 times more abundant than ^{3}He in the atmosphere and 10^5 times

424   more abundant in the mantle (e.g., Marty and Jambon 1987). Hence, although cosmogenic ^{4}He

425   is also produced in terrestrial rocks, the average non-cosmogenic ^{4}He concentrations in minerals

426   are so large that they hamper the detection of any cosmogenic ^{4}He excess. It is thus reasonable

427   to consider cosmogenic ^{4}He contributions as negligible. Thus, only three ^{4}He origins are

428   relevant to the ^{4}He budget of terrestrial minerals that have been exposed at the Earth's surface

429   (Fig. 4; Table 1):

430

431   i) Magmatic ^{4}He (^{4}He$_{mag}$) is fluid/melt inclusion- and matrix-hosted, and its

432   concentration is time-independent;
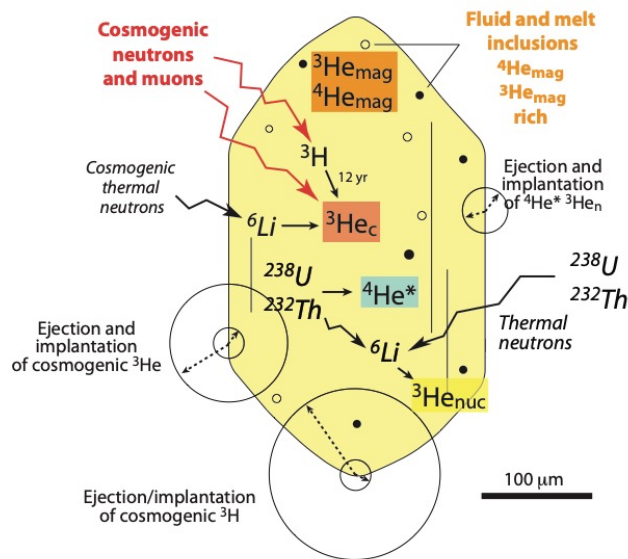
433   ii) Radiogenic ^{4}He (^{4}He*) is produced by the decay of ^{238}U, ^{235}U, and ^{232}Th, is matrix-

434   hosted, and its concentration increases with helium closure age, and;

435   iii) Atmospheric ^{4}He (^{4}He$_{atm}$) is present as a contaminant on the surfaces of analyzed

436   silicates and its concentration is time-independent.

437

438

A/ Inventory of helium species and production pathways in a phenocryst

B/ Range of ^{3}He and ^{4}He concentrations

C/ Stopping distance of cosmogenic ^{3}He and ^{3}H in basalt
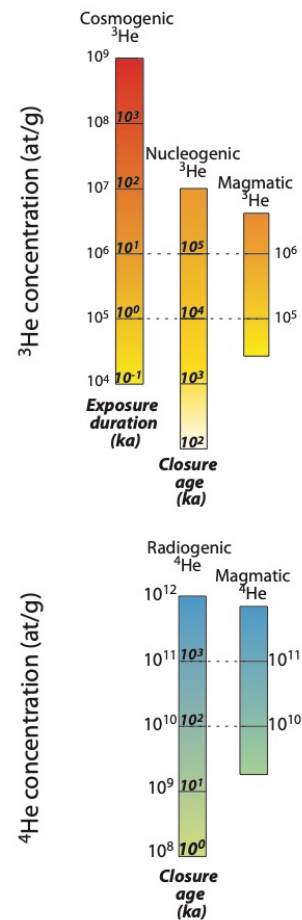
Figure 4. (A) Inventory of ^{3}He and ^{4}He species (^{3}He$_c$, cosmogenic ^{3}He; ^{3}He$_{mag}$, magmatic ^{3}He; ^{3}He$_{nuc}$, nucleogenic ^{3}He; ^{4}He$_{mag}$, magmatic ^{4}He; ^{4}He*, radiogenic ^{4}He) and production pathways in an olivine phenocryst. **(B)** Ranges of ^{3}He and ^{4}He concentrations in phenocrysts, assuming cosmogenic ^{3}He production at sea level, a nucleogenic ^{3}He production rate of 0.01 at g^{-1} yr^{-1} and a radiogenic ^{4}He production rate of 10^5 at g^{-1} yr^{-1} (typical values for olivine phenocrysts in basalt) **(C)** Stopping distances of cosmogenic ^{3}He and ^{3}H in basalt (Larsen et al., 2019; Ziegler et al., 2010).

In practice, diverse laboratory procedures are used to selectively release these different helium components, depending on their location in the studied mineral (Table 1; Fig. 4). The two main categories of extraction methods are: *i) in vacuo mineral crushing*, which preferentially releases the magmatic helium components hosted in fluid and melt inclusions; and *ii) in vacuo heating or melting (using a furnace or a laser)*, which extracts all matrix and inclusion-hosted helium components from the mineral. The heating step is mandatory to extract the totality of the cosmogenic ^{3}He from a sample, but inconveniently releases all other varieties (magmatic ^{3}He and ^{4}He, radiogenic ^{4}He, nucleogenic ^{3}He, and atmospheric ^{3}He and ^{4}He), which may complicate the detection of cosmogenic ^{3}He. Thus, this section presents the most suited

17

strategies to correct for these non-cosmogenic ^{3}He components, and section 4 details extraction procedures and helium measurement techniques.

Table 1 – Characteristics of ^{3}He and ^{4}He varieties

Component	Cosmogenic	Magmatic	Nucleogenic	Radiogenic	Atmospheric
^{3}He	Matrix-hosted. Concentration increases with exposure age.	Hosted in fluid/melt inclusions and matrix. Time-independent concentration. Determination by vacuum crushing or isochrons. Less abundant in fractions finer than 500 μm.	Produced by thermal neutron capture in ^{6}Li. Matrix-hosted. Concentration increases with closure age.	Absent.	Contaminant adsorbed at the grain surface. Time-independent concentration. Less abundant in fractions coarser than 100 μm.
^{4}He	Negligible compared to other ^{4}He varieties.	Same as ^{3}He.	Absent.	Produced by decay of ^{238}U, ^{235}U, and ^{232}Th. Matrix-hosted. Concentration increases with closure age.	Same as ^{3}He.

When a mineral sample is fused in vacuo, all ^{3}He and ^{4}He species are released, whatever their location in the mineral. Hence, the total ^{3}He amount measured with a noble gas mass spectrometer is defined by the budget (modified from Farley et al., 2006; Blard and Farley, 2008):

468

$$^3\text{He}_{\text{tot}} = {}^3\text{He}_{\text{c}} + {}^3\text{He}_{\text{mag}} + {}^3\text{He}_{\text{nuc}} + {}^3\text{He}_{\text{atm}} . \tag{2}$$

470

471 Equation (2) is similar to:

472

$$^3\text{He}_{\text{tot}} = \int_0^{t_e} P_3 \, dt + {}^3\text{He}_{\text{mag}} + \int_0^{t_c} P_{\text{nuc}} \, dt + {}^3\text{He}_{\text{atm}} , \tag{3}$$

474

475 where P_3 and P_{nuc} (at g^{-1} yr^{-1}) are the time-dependent local cosmogenic and nucleogenic ^{3}He

476 production rates, respectively, and t_e and t_c (yr) are the exposure and closure ages of the sample,

477 respectively.

478 Additionally, the ^{4}He budget can be written as:

479
$$^4\text{He}_{\text{tot}} = {}^4\text{He}_{\text{mag}} + {}^4\text{He}^* + {}^4\text{He}_{\text{atm}} , \tag{4}$$

480

481 or:

482

$$^4\text{He}_{\text{tot}} = {}^4\text{He}_{\text{mag}} + \int_0^{t_c} P_4 \, dt + {}^4\text{He}_{\text{atm}} , \tag{5}$$

484

485 where P_4 (at g^{-1} yr^{-1}) is the time-dependent ^{4}He* production rate and t_c (yr) is the closure age

486 of the sample.

487

488 **3.2. Magmatic ^{3}He and ^{4}He**

489 **3.2.1. Impact of the ^{3}He$_{\text{mag}}$ correction on the final cosmogenic ^{3}He uncertainty**

490 Just as it is more difficult to find a golf ball in tall grass than on a well-maintained

491 fairway, the relative uncertainty on the cosmogenic ^{3}He concentration increases with increasing

492 contribution from magmatic ^{3}He (Figs. 4, 5). This is a signal-to-noise ratio issue: the higher the

493 ratio, the lower the uncertainty arising from the magmatic ^{3}He correction. This relationship can

494 be modeled by defining the uncertainty on the total cosmogenic ^{3}He concentration based on the

495 uncertainties on the other variables, notably the ^{4}He concentrations and the magmatic ^{3}He/^{4}He

496 ratio: equation (6) is derived from equation (1) by applying the Taylor series approximation

497 and assuming that all involved uncertainties are independent:

498

$$\sigma^2_{{}^3\text{He}_c} = \sigma^2_{{}^3He_{tot}} + \left[\sigma\,{}^4\text{He}_{\text{mag}} \cdot \left(\frac{{}^3\text{He}}{{}^4\text{He}} \right)_{\text{mag}} \right]^2 + \left({}^4\text{He}_{\text{mag}} \cdot \sigma_{3/4} \right)^2 , \tag{6}$$

500

501 where $\sigma_{^3He_c}$, $\sigma_{^3He_{tot}}$, $\sigma_{^4He_{mag}}$, and $\sigma_{3/4}$ are the uncertainties on the cosmogenic ^{3}He

502 concentration, the total ^{3}He amount extracted by fusion, the magmatic ^{4}He concentration, and

503 the magmatic ^{3}He/^{4}He ratio, respectively.

504   Figure 5 shows the impact of the magmatic helium correction on the final uncertainty

505 of the measured ^{3}He$_c$ concentration under different exposure scenarios using Equation (6). This

506 calculation illustrates the importance of the ^{3}He$_c$/^{3}He$_{mag}$ ratio on the final uncertainty on ^{3}He$_c$:

507 the larger the magmatic correction, the lower the uncertainty. The impact of the magmatic

508 correction on the ^{3}He$_c$ uncertainty is hence larger at lower elevations, where the cosmogenic

509 production rate is smaller. For the median magmatic ^{4}He concentrations reported in olivine and

510 pyroxene phenocrysts (Fig. 5C), the total relative uncertainty on cosmogenic ^{3}He is below 5%

511 and 20% for 100 ka and 10 ka surfaces, respectively (Fig. 5A,B). However, the uncertainty may

512 reach 50-100% in the case of 1 ka surfaces.
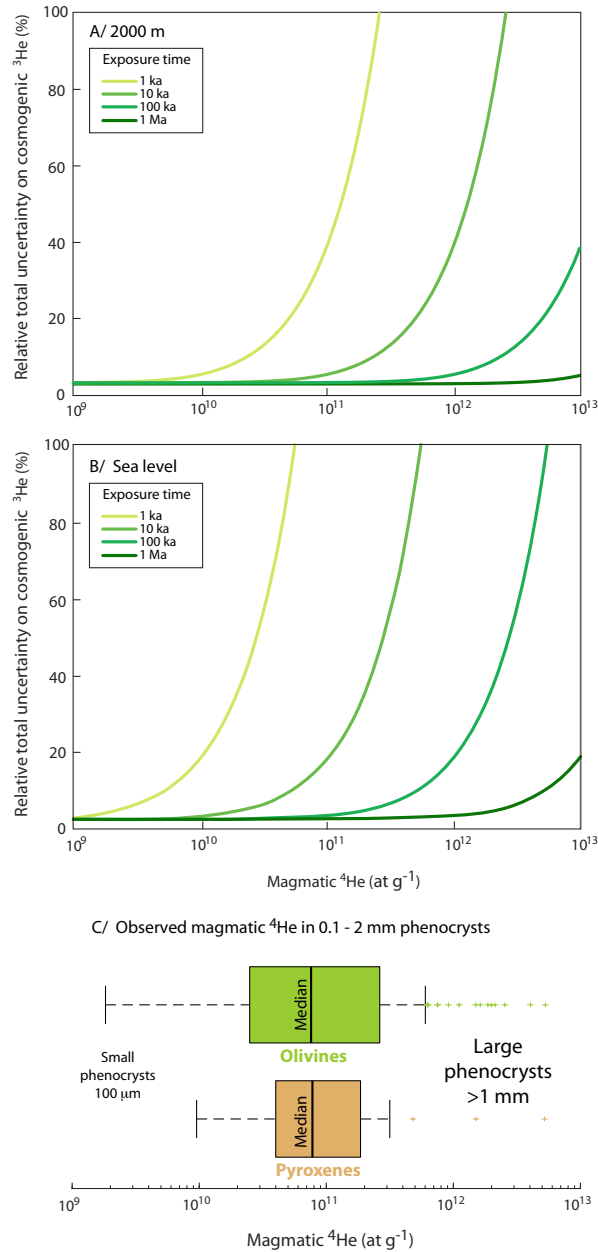
Figure 5. (A, B) Modeling the total relative uncertainty (1σ) of the measured cosmogenic ³He concentration for variable magmatic ⁴He concentrations and exposure durations. Because the ³He$_c$ production rate changes with elevation, this simulation considers a mineral at (A) 2,000 m elevation and (B) sea level. This calculation applies Equation (6) assuming a magmatic ³He/⁴He ratio of 8 Ra with an uncertainty of 20%, an uncertainty of 3% on the total amount of ³He extracted by fusion, an uncertainty of 1% on the total amount of ⁴He extracted by fusion, and a negligible contribution from radiogenic ⁴He. (C) The distribution of the total magmatic ⁴He concentrations observed in olivine and pyroxene phenocrysts (Ackert et al., 2003; Blard et al., 2006; Cerling and Craig, 1994; Dunai and Wijbrans 2000; Eaves et al., 2015; Fenton and Niedermann, 2014; Foeken et al., 2012; Goehring et al., 2010; Licciardi et al., 2006; Licciardi et al., 1999). This dataset includes only lavas that are young enough (<200 ka) to ensure that the radiogenic ⁴He correction does not represent a significant systematic uncertainty.

527   A recent compilation of magmatic helium concentrations measured in olivine and
528   pyroxene phenocrysts in basalts (Puchol et al., 2017 and references therein) indicates that the
529   total magmatic helium concentrations in these phenocrysts are largely variable, both at the scale
530   of a single lava flow and among minerals in a single sample (Fig. 5C, Table S1,
531   https://doi.org/10.24396/ORDAR-89). On average, magmatic ^{4}He concentrations measured in
532   132 olivine and 32 pyroxene phenocrysts (ranging in size from 0.2 to 2 mm and from basalts in
533   different geological settings) display mean ^{4}He concentrations of 3×10^{11} at g^{-1} (median of $8 \times$
534   10^{10} at g^{-1}) for both olivine and pyroxene. Note, however, that some samples may be very rich
535   in ^{4}He, reaching concentrations above 10^{12} at g^{-1}, implying a significant intersample variability
536   (standard deviation $> 6 \times 10^{10}$ at g^{-1}; Fig. 5C, Table S1). Such variability may also be observed
537   for aliquots of hundreds of grains, even if all grains originate from the same sample. This
538   significant intersample variability can be described as a "nugget effect" that is probably
539   controlled by the abundance and repartitioning of fluid and melt inclusions, which are generally
540   rich in magmatic gas and vary in their abundance in phenocrysts from one geological context
541   to another (e.g. Puchol et al., 2017). However, this dataset is not large enough to establish a
542   systematic or to understand why some volcanic fields present phenocrysts with higher
543   magmatic helium contents than others (Table S1). In any case, an efficient means of minimizing
544   the uncertainty from the magmatic He correction is to select phenocrysts with low magmatic
545   helium concentrations, or to find methods for reducing this initial concentration (see section
546   3.2.2).
547

548   **3.2.2. Using grains sized 100–500 μm reduces the magmatic helium contribution**
549   Observations show that phenocryst size is a first-order control on helium concentrations,
550   all other things being equal (Puchol et al., 2017). Furthermore, progressive phenocryst crushing
551   experiments have demonstrated that laboratory (Williams et al., 2005) or natural crushing (e.g.,
552   by erosion; Puchol et al., 2007) may reduce the magmatic He content by releasing the magmatic
553   component that is preferentially hosted in melt and fluid inclusions. Hence, crushing
554   phenocrysts (in vacuo or in air) before fusing the finest fraction may appear to be a good
555   strategy, because it purges magmatic helium and thus reduces the uncertainty on the computed
556   cosmogenic ^{3}He concentration. Although it is sometimes misleading to propose a universal
557   grain size cutoff, experiments have shown that analyzing phenocrysts smaller than 500 μm is
558   generally efficient in significantly reducing the magmatic helium component and intergrain
559   variability (Puchol et al., 2017; Williams et al., 2005).

560   Reducing the granulometry of the analyzed phenocrysts should however be performed
561 with caution: several studies have reported the suspected loss of matrix-hosted ^{3}He during in-
562 vacuo crushing for longer than 1 min (Blard et al., 2006; Hilton et al., 1993; Yokochi et al.,
563 2005) and, more worrisome, Protin et al., (2016) recently demonstrated that significant amounts
564 of atmospheric helium may be adsorbed onto the newly created surfaces when crushing silicates
565 in atmospheric conditions. This effect must be considered seriously because experimental data
566 indicate that the high adsorption energy of atmospheric helium requires heating above 1000 °C
567 to release the contamination, which affects cosmogenic ^{3}He (Protin et al., 2016). Because
568 atmospheric helium is adsorbed on surfaces, the magnitude of the contamination is inversely
569 proportional to grain size. Experimental data from olivines show that contamination remains
570 insignificant (compared to matrix-hosted helium varieties) for grains larger than 100 μm (Protin
571 et al., 2016). As both the loss of matrix-hosted cosmogenic ^{3}He and unexpected atmospheric
572 contamination result in underestimated cosmogenic ^{3}He concentrations, grains smaller than 100
573 μm should be avoided in cosmogenic ^{3}He analyses. Consequently, combining the need to
574 reduce the magmatic helium component while avoiding any atmospheric helium contamination
575 defines the ideal granulometric window for cosmogenic ^{3}He analyses: the fusion of minerals
576 ranging in size ***from 100 to 500 μm*** should be favored, regardless of whether they were
577 previously crushed (Fig. 5).

578   Another promising and innovative technique recently tested by Hofmann et al. (2021)
579 is to use X-ray micro-computed tomography (μCT) to identify grains that are free of melt/fluid
580 inclusions and thus have much lower magmatic ^{3}He concentrations. Finally, an alternative to
581 crushing is to melt several aliquots from the same sample and build ^{3}He *vs* ^{4}He isochrons
582 (section 3.5.3). Using this method, one can distinguish the cosmogenic and magmatic ^{3}He
583 components without vacuum crushing, avoiding all the above-mentioned potential issues.

584

585 **3.3. Radiogenic ^{4}He**

586   Radiogenic ^{4}He is produced by the decay of radioactive isotopes (such as uranium and
587 thorium) present in the mineral of interest (e.g. olivine, pyroxene). It is important to properly
588 estimate the ^{4}He* concentration to accurately estimate the magmatic ^{4}He and ^{3}He contributions
589 (Blard and Farley, 2008). In many settings, radiogenic ^{4}He concentrations are indeed non-
590 negligible and may be of the same order of magnitude as the magmatic ^{4}He component. In
591 extreme cases, the radiogenic ^{4}He concentration may even be several orders of magnitude

greater than the magmatic ^{4}He concentration, requiring specific approaches to estimate the magmatic ^{3}He component (e.g. Martin et al., 2018; Balter-Kennedy et al., 2020).

The radiogenic ^{4}He concentration, which is constrained by the mineral's closure age t_c and the chemical composition of the rock, can hence be used to determine the most suitable method and analytical strategies for performing non-cosmogenic ^{3}He corrections (see section 3.5).

3.3.1. The production of radiogenic ^{4}He: general principles and equations

Radiogenic ^{4}He is produced by the α-decay of ^{235}U, ^{238}U, and ^{232}Th when these elements are present in a studied mineral and its host lithology. ^{147}Sm and ^{148}Sm also release alpha particles through radioactive decay, but this contribution is generally negligible in silicates (Zeitler, 2014). ^{4}He* production through time is described as:

$$^4\text{He}^* = \int_0^{t_c} P_4 dt \,, \qquad (7)$$

where t_c is the helium closure age (i.e., the eruption age in the case of volcanic rocks) and P_4 is the production rate of ^{4}He*. If t_c is long enough to have reached secular equilibrium, Equation (7) simplifies to:

$$^4\text{He}^* = P_4 \times t_c \,. \qquad (8)$$

Note that, in the case of rocks with young crystallization ages (<500 ka), the assumption of secular equilibrium may not be valid, and disequilibrium must be considered when calculating P_4 (Aciego et al., 2007; Farley et al., 2002). That said, even for lavas younger than 500 ka and when using the maximum ^{230}Th/^{238}U fractionation reported for pyroxenes and olivines (Aciego et al., 2007; Wood et al., 1999), the obtained value of P_4 differs from that obtained under the secular equilibrium assumption by <5% (Farley et al., 2002)

To avoid circular reasoning and the difficulty of estimating the magmatic ^{4}He contribution, t_c should be estimated using a different radiochronometer than (U-Th)/^{4}He*, such as K-Ar or ^{40}Ar/^{39}Ar; this is often feasible for lavas because the crystallization age equals the helium closure age. However, in the case of plutonic or metamorphic rocks, in which minerals generally have helium closure ages younger than the crystallization age, (U-Th)/^{4}He* dating is a necessary alternative. In those cases, this should be done using minerals with large (U-

624   Th)/^{4}He$_{mag}$ ratios to avoid bias and uncertainties in estimating ^{4}He* that result from the

625   magmatic ^{4}He component.

626   Since the ejection distance of alpha particles is ~20 μm in rocks (Ziegler 1977), some

627   radiogenic ^{4}He produced in the surrounding matrix is also implanted in minerals (Lal 1989).

628   Conversely, a fraction of the in-situ ^{4}He* may also be ejected from minerals. Thus, one must

629   consider both ejection and implantation when computing P_4. Based on a series development

630   formula, P_4 can be calculated as (Farley et al., 2006):

631

632 $$P_4 = I_4 \left[1 - 1.5(S/D) + 0.5(S/D)^3\right] + M_4 \left[1.5(S/D) - 0.5(S/D)^3\right] , \quad (9)$$

633

634   where I_4 and M_4 are the ^{4}He* production rates in the mineral of interest and in the surrounding

635   rock, respectively, S (μm) is the stopping distance of alpha particles (~20 μm). D (μm) is the

636   crystal diameter, and Equation (9) is thus only valid for minerals having a spherical geometry;

637   for non-spherical phenocrysts, it is necessary to compute an equivalent sphere diameter (Farley

638   and Stockli 2002).

639   If secular equilibrium is reached, I_4 and M_4 follow (e.g., Wolf et al., 1998):

640

641 $$I_4 \text{ (or } M_4) = 8\lambda_{238}[^{238}U] + 7\lambda_{235}[^{235}U] + 6\lambda_{232}[^{232}Th] , \quad (10)$$

642

643   where $[^{238}U]$, $[^{235}U]$, and $[^{232}Th]$ are the isotopic concentrations measured in the mineral (for

644   I_4) or the whole rock (for M_4) and λ_{238}, λ_{235}, and λ_{232} are their respective decay constants.

645

646   **3.3.2. Removing the implanted ^{4}He* component**

647   The proportion of in-situ ^{4}He* relative to the implanted component is controlled by

648   phenocryst size and by the relative U and Th concentrations in the phenocrysts and their host

649   rock, i.e., the effective mineral/melt partition coefficients for these elements. Measurements of

650   U and Th in mineral separates and in whole rocks show that these partition coefficients vary

651   greatly across lithologies and geological settings (e.g. Blard and Farley, 2008) and are strongly

652   dependent on the abundance of U-Th-rich melt inclusions. They should thus be called "apparent

653   partition coefficients". The presence of U-Th-rich melt inclusions may also induce significant

654   spatial heterogeneities in the mineral of interest, implying that spot analyses by secondary ion

655   mass spectrometry could be misleading. Bulk U-Th analyses after mineral dissolution are thus

656   preferable because they represent the mean U-Th concentration.

657   Correcting for implantation and ejection of ^{4}He* may also be complicated by several

658   issues, and thus be a source of significant uncertainties. This is particularly true for detrital

659   minerals in river sediments: because these minerals may have been fragmented, their initial

660   sizes are generally unknown, as well as the exact U and Th concentrations of their source rocks.

661   Moreover, in the case of non-spherical grains, shape estimates and the conversion to equivalent

662   sphere diameter may also induce significant uncertainties.

663   Removing the external portion (at least 20 µm) of phenocrysts should therefore be a

664   systematic sample preparation step because it obviates the need to correct for implanted and

665   ejected components (Aciego et al., 2007; Blackburn et al., 2007; Bromley et al., 2014; Gayer

666   et al., 2008; Min et al., 2006). Using this method, geometric corrections are unnecessary and

667   the radiogenic ^{4}He production rate equals the in-situ ^{4}He* production rate, simplifying Equation

668   (9) to $P_4 = I_4$; this has the potential to reduce the uncertainties associated with calculating the

669   ^{4}He* component. For olivine and pyroxene, Bromley et al., (2014) proposed a chemical

670   treatment in which minerals are leached for 2 hours in a 3% HF:10% HCl acid solution in an

671   ultrasonic bath at 40 °C. Physical techniques, such as over-pressurized air abrasion in closed

672   chambers, also efficiently remove the external ^{4}He*-enriched rim (Aleinikoff et al., 1990).

673   If it is not possible to remove the external rim affected by alpha particle mobility, it is

674   of primary importance to measure the U and Th concentrations in both the phenocrysts and

675   their host rock, especially in samples with large closure/exposure age ratios.

676

677

678

679

680   **3.3.3. Uncertainty arising from the radiogenic ^{4}He correction**

681   To show the importance of accurately and precisely estimating the radiogenic ^{4}He

682   concentration, I modelled the total relative uncertainty on the cosmogenic ^{3}He concentration

683   for different exposure ages, closure age scenarios (10 ka to 1 Ga), and different elevations in

684   Figure 6. In this model, the uncertainty on cosmogenic ^{3}He is computed from a Taylor series

685   expansion as:

686
$$\sigma^2_{^3He_c} = \sigma^2_{^3He_f} + \left[\sigma_{^4He_{mag}} \cdot \left(\frac{^3He}{^4He} \right)_{mag} \right]^2 + \left[\sigma_{^4He^*} \cdot \left(\frac{^3He}{^4He} \right)_{mag} \right]^2 +$$

687
$$\left[\left(^4He_{tot} - ^4He^* \right) \cdot \sigma_{3/4} \right]^2 . \tag{11}$$

688

689   The model results demonstrate that the radiogenic ^{4}He correction may induce a

690 significant uncertainty on the final estimated cosmogenic ^{3}He concentration, with the error

691 increasing with increasing closure/exposure age ratio and magmatic ^{4}He concentration. For

692 helium closure ages older than 10 Ma and exposure ages younger than 100 ka, the total relative

693 uncertainty on ^{3}He$_c$ is larger than 5% and may even reach 100% for exposure ages younger than

694 10 ka (Fig. 6). In these extreme scenarios with 100% uncertainty, ^{3}He$_c$ is below the detection

695 limit. The precision and detection limit of ^{3}He$_c$ determination can hence be improved by

696 selecting samples with the youngest (U-Th)/^{4}He closure age, when possible, and by reducing

697 the magmatic He component by preferentially melting grains in the 100–500 μm size range or

698 by identifying inclusion free minerals by μCT (Hofmann et al., 2021).
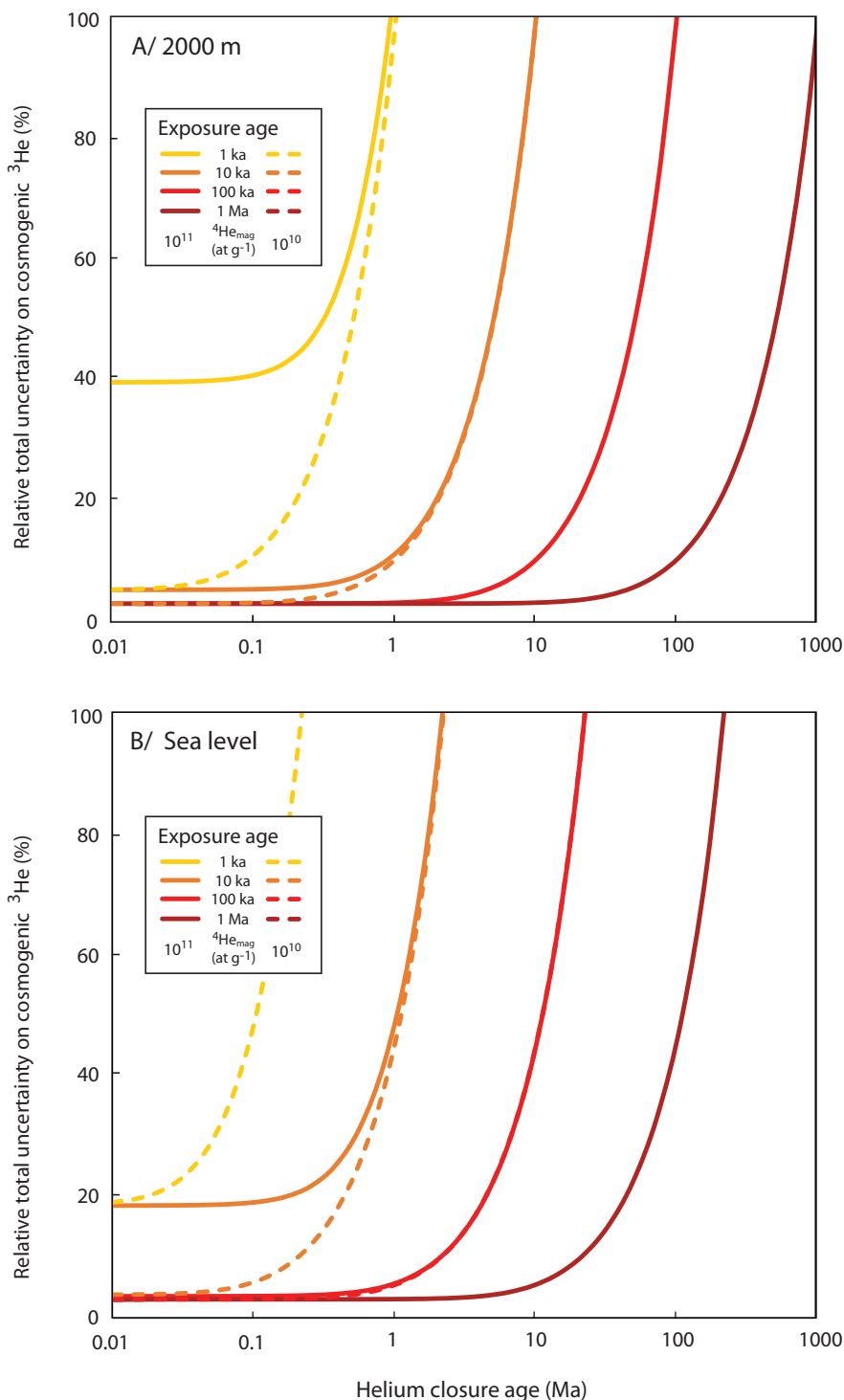
699

Figure 6. Modeling the impact of the radiogenic ^{4}He correction - described by the (U-Th)/^{4}He* cooling age - on the total relative uncertainty (1σ) on the measured cosmogenic ^{3}He concentration for variable exposure durations. Two magmatic ^{4}He concentrations are considered: 10^{10} and 10^{11} at g^{-1} (dashed and solid curves, respectively). Because the ^{3}He$_c$ production rate changes with elevation, this simulation considers samples exposed at (A) 2,000 m elevation and (B) sea level. This calculation applies Equation (11) assuming a magmatic ^{3}He/^{4}He ratio of 8 Ra with 20% uncertainty, an uncertainty of 3% on the total amount of ^{3}He extracted by fusion, an uncertainty of 1% on the magmatic ^{4}He concentration, and an uncertainty of 10% on the estimated radiogenic ^{4}He concentration.
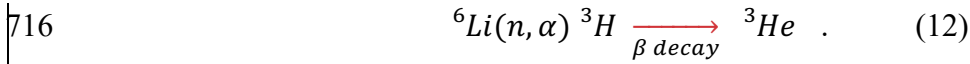
3.4. Nucleogenic ^{3}He

3.4.1. The production of nucleogenic ^{3}He: general principles and equations

In minerals, nucleogenic ^{3}He is produced by the capture of low-energy neutrons by ^{6}Li through the reaction (Andrews 1985; Andrews and Kay 1982; Dunai et al., 2007):

$$^6Li(n,\alpha)\ ^3H \xrightarrow[\beta\ decay]{} \ ^3He \ .\qquad (12)$$

Neutrons involved in this reaction are "thermal", "epithermal", and "slow" neutrons with energies ranging between 0.025 and 300 eV, far below those of the cosmogenic "fast" neutrons (>1 MeV) involved in the main cosmogenic ^{3}He production pathway (Dunai, 2010; Gosse and Phillips, 2001). Some of this low-energy neutron flux into rocks originates from nuclear reactions between cosmic rays and the terrestrial environment (Lal, 1987). However, ^{3}He production through the capture of cosmogenic thermal neutrons is significantly lower than that by cosmogenic spallation, at least in the case of minerals with typical Li concentrations of 2–50 ppm (Dunai et al., 2007).

Low-energy neutrons involved in the production of ^{3}He through capture by ^{6}Li are also produced by (α,n) reactions (Andrews, 1985; Andrews and Kay, 1982) involving elements within rocks and alpha particles emitted by the natural decay of U and T. The total production rate P_{nuc} of nucleogenic ^{3}He thus depends on the Li concentration in the mineral of interest and the bulk U and Th concentrations and chemical composition of the whole rock within ~1 m of the mineral. In a given mineral, P_{nuc} can be calculated as (modified from Andrews, 1985):

$$P_{nuc} = f_n \frac{[\sigma_{Li}C_{Li}]_{mineral}}{\left[\sum_i^k \sigma_i C_i\right]_{rock}} \ .\qquad (13)$$

where f_n is the average thermal neutron flux originating from the bulk rock, σ_i is the neutron capture cross section specific to element i, and C_i is the concentration of element i (in mol g^{-1} or atomic percent). To accurately compute P_{nuc}, it is thus important to measure the Li concentration in the mineral of interest. According to Andrews and Kay (1982), the whole-rock concentrations of 17 elements ($k = 17$) are also needed to calculate the denominator of Equation (13), $\left[\sum_i^k \sigma_i C_i\right]_{rock}$: nine major elements (Si, Al, Fe, Mn, Mg, Ca, Na, K, Ti) and eight trace elements with cross sections larger than 1 barn (Li, B, Co, Cr, Ni, Gd, Sm, Cl).

741   The whole-rock concentrations of the two main α-emitters, U and Th, also need to be
742   determined. The (α,n) reactions occurring in rock indeed determine f_n, which is computed as
743   (Andrews and Kay, 1982):
744
745    $$f_n = \frac{U}{100} \cdot (13.8 \cdot Na + 5.4 \ \cdot Mg + 5.0 \cdot Al + 1.31 \cdot Si + 0.6 \cdot Ca) + \frac{Th}{100} \cdot (6 \cdot Na +$$
746    $$2.45 \ \cdot Mg + 2.55 \cdot Al + 0.56 \cdot Si + 0.25 \cdot Ca) + 0.4764 \cdot U \ , \qquad (14)$$
747
748   where U and Th concentrations are in ppm (10^{-6} g g^{-1}) and the whole-rock major elements
749   concentrations are in atomic percent (%). Importantly, all these elemental concentrations must
750   be measured in a rock sample that is representative of the bulk rock. Indeed, the absorption
751   paths of low-energy neutrons produced through (α,n) reactions in rocks typically range between
752   50 and 80 cm, implying that the radiogenic thermal neutron flux is spatially averaged and rather
753   homogenous within a monolithologic unit (Dunai et al., 2007; Lal, 1987).
754   An Excel spreadsheet is available in the Supplementary Information (Table S2,
755   https://doi.org/10.24396/ORDAR-90) to compute P_{nuc} and the total $^3He_{nuc}$ concentration when
756   the closure age is known. As inputs, this spreadsheet requires the 19 whole-rock major and trace
757   element concentrations involved in Equation (13), as well as the Li concentration measured in
758   the mineral of interest.
759

3.4.2. Uncertainty arising from the nucleogenic ^{3}He correction

761   The concentration of nucleogenic ^{3}He in a mineral is thus mainly controlled by the
762   chemical composition of the rock and the helium closure age. Figure 7A shows modeled
763   nucleogenic ^{3}He concentrations *vs* helium closure age for various Li contents and lithologies
764   (granite, andesite, basalt). Compared to basalt phenocrysts, the build-up of $^3He_{nuc}$ may be
765   several order of magnitudes higher in Li-rich minerals (e.g. amphiboles) hosted in U-rich
766   granite (Fig. 7A).
767   To assess the impact of correcting for $^3He_{nuc}$ on the precision of the measured
768   cosmogenic ^{3}He concentration, I modeled the relative uncertainty arising from the nucleogenic
769   ^{3}He correction as a function of helium closure age for variable exposure durations (1 ka, 10 ka,
770   100 ka, 1 Ma), at 2,000 m elevation or sea level, in the case of a mineral containing 10 ppm Li
771   and hosted in an andesite (Fig. 7B, C). This model shows that for helium closure ages younger
772   than 1 Ma, the uncertainty arising from the nucleogenic ^{3}He correction remains below 20%,
773   even for exposure ages as young as ~1 ka (Fig. 7B, C). However, for longer helium closure

ages, the detection limit and the final uncertainty increase and may become significant. For example, in the case of 10 Ma closure ages, the total uncertainty is larger than 20% for exposure ages younger than 10 ka at sea level (Fig. 7C).

Whenever possible, it is thus important to select rock samples with the largest possible exposure/closure age ratio to improve the precision on the measured cosmogenic ^{3}He concentration.
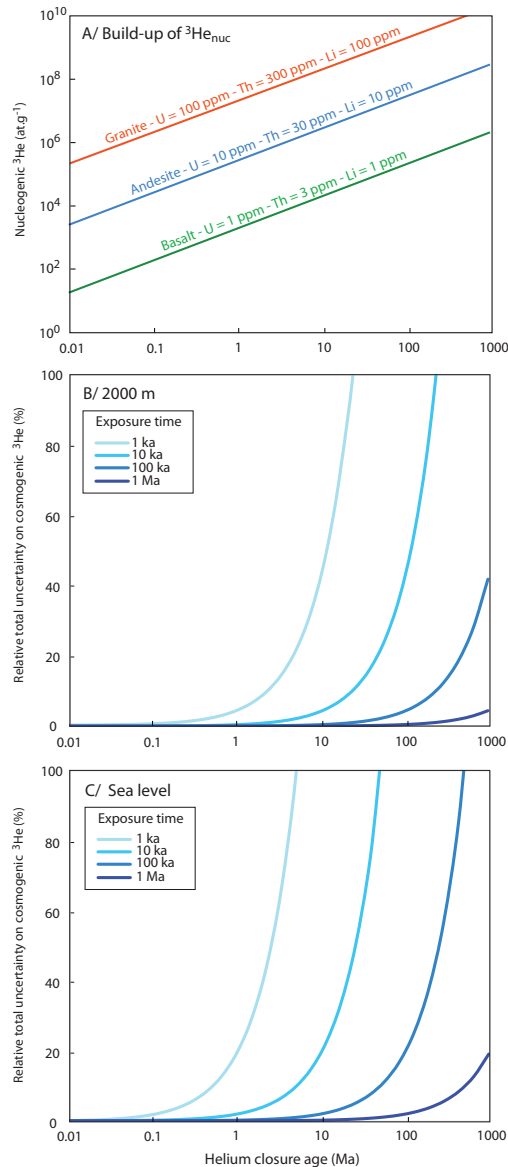
Figure 7. (A) Nucleogenic ^{3}He concentrations *vs* helium closure age for various mineral Li contents and lithologies (granite, andesite, basalt). (B, C) Uncertainty on the cosmogenic ^{3}He concentration due to the nucleogenic ^{3}He correction for variable closure ages, at 2,000 m elevation, and sea level, respectively. This modeling assumes a mineral containing 10 ppm Li in a rock of average andesitic composition with bulk U and Th contents of 10 ppm and 30 ppm, respectively, corresponding to $P_{nuc} = 0.25$ at g^{-1} yr^{-1} (shown in blue in (A)). This model assumes that the nucleogenic production rate is known with a relative uncertainty of 10%.

3.5. Strategies to estimate the non-cosmogenic ^{3}He components

789

790   Correcting for non-cosmogenic ^{3}He components is key to achieving low detection limits
791   and final uncertainties on cosmogenic ^{3}He concentrations. Several characteristics of a rock's
792   geological history must be carefully evaluated for each sample, notably the helium closure age,
793   the amount of magmatic helium in the minerals, and the concentrations of U, Th, and Li in the
794   minerals and their host rocks. Depending on the thermal history and chemical composition of a
795   rock sample, the minimum measurable surface exposure age may vary by several orders of
796   magnitude, from 10^2 to >10^6 years (Figs. 5–7). Hence, when background geological information
797   is available (e.g. from geological maps), field sampling should first target rocks with the
798   youngest cooling history, and select minerals/rocks with the lowest U, T,h and Li
799   concentrations, such as olivine and pyroxenes in basalts or andesites.

800   Different analytical strategies and procedures can be used to correct for the non-
801   cosmogenic ^{3}He components, and the choice of the best strategy mainly depends on the specific
802   characteristics of a given sample. Figure 8 is an easy-to-use flowchart that summarizes the
803   analytical protocol, from bulk sample crushing to final cosmogenic ^{3}He calculation, for various
804   sample cases.

805

Flowchart for cosmogenic ^{3}He measurements

$^3\text{He}_{tot} = {}^3\text{He}_c + {}^3\text{He}_{mag} + {}^3\text{He}_{nuc}$

$^3\text{He}_{tot} = {}^3\text{He}_c + {}^4\text{He}_{mag} \times \left(\frac{^3\text{He}}{^4\text{He}}\right)_{mag} + f(U_{rock}, Th_{rock}, Li_{min}, t_c)$

$^4\text{He}_{tot} = {}^4\text{He}_{mag} + {}^4\text{He}^* = {}^4\text{He}_{mag} + f(U_{min}, Th_{min}, t_c)$
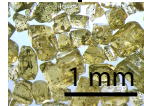
Thin section: petrographic characteristics (optional)

1 – Isolation of minerals (olivines, pyroxenes)

Save a 3 cm x 3 cm piece
Crush bulk rock
Sieve: 100-500 µm and 500-1000 µm
Density and magnetic separation
Quality check: handpicking under a microscope to remove grains with adhering lava, oxides, clays

~1 g bulk rock aliquot

Major and trace elements in rock Li, U-Th-Sm

Thermal neutron flux in the rock

1 mm

2 – Removal of 20 µm external rim
to remove the implanted ^{4}He*

Chemical: HF 3% - HCl 5% for 2 hours (20 mL/g) at 40 °C
HCl 40% rinsing ×3 - H$_2$O rinsing ×3 - Drying

or

Physical: abrasion with compressed air

Microscope quality check: remove newly formed fluorides

~1 g mineral aliquot

Major and trace elements in the mineral U-Th-Sm, Li

× closure age t_c $^\&$

^{4}He*

^{3}He$_{nuc}$

P_4

P_{nuc}

100-500 µm minerals

1a – 10 min in vacuo crushing of ~0.5 g: ^{3}He$_{mag}$
and/or
1b – Fuse ~0.1 g of shielded sample: ^{3}He$_{mag}$ + ^{3}He$_{nuc}$

2 - Fusion of ~0.05 g to 1 g: ^{3}He$_{tot}$ ^{4}He$_{tot}$

^{3}He$_c$ = ^{3}He$_{tot}$ – ^{3}He$_{mag}$ – ^{3}He$_{nuc}$

YES

Case 3

^{4}He* >> ^{4}He$_{mag}$?

Hypothesis: ^{3}He$_{mag}$ homogeneous

NO

Uneroded Lava?

YES
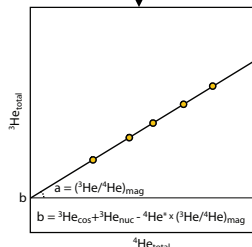
NO

Case 1

or

Standard method

1 - Crushing in vacuuo ~ 0.5 g aliquot of 0.5-1 mm minerals
(^{3}He/^{4}He)$_{mag}$

2 – Fusion$^\#$ of ~0.05 g to 1 g aliquot of 100-500 µm minerals
^{3}He$_{tot}$ ^{4}He$_{total}$

$^3\text{He}_c = {}^3\text{He}_{tot} - ({}^4\text{He}_{tot} - {}^4\text{He}^*) \times \left(\frac{^3\text{He}}{^4\text{He}}\right)_{mag}$
$- {}^3\text{He}_{nuc}$

$^\#$ *Before any He extraction in a furnace, weigh the samples and wrap in metal foil.*

Isochrons

Fusion$^\#$ of several aliquots of ~ 0.5 g of 0.1 to 1 mm minerals
^{3}He$_{total}$ ^{4}He$_{total}$

$a = (^3\text{He}/^4\text{He})_{mag}$

$b = {}^3\text{He}_{cos} + {}^3\text{He}_{nuc} - {}^4\text{He}^* \times (^3\text{He}/^4\text{He})_{mag}$

^{3}He$_{total}$

^{4}He$_{total}$

$^3\text{He}_c = b + {}^4\text{He}^* \times a - {}^3\text{He}_{nuc}$

Case 2

$^\&$ Particular case of uneroded lava flow:
t_c is unnecessary

Standard method

$^3\text{He}_c = \frac{1}{R}\left[{}^3\text{He}_{tot} - {}^4\text{He}_{tot} \times \left(\frac{^3\text{He}}{^4\text{He}}\right)_{mag}\right]$

Isochrons

$^3\text{He}_c = \frac{b}{R}$

with:

$R = 1 - \frac{P_4}{P_3} \times \left(\frac{^3\text{He}}{^4\text{He}}\right)_{mag}$

806

807

808

809 **Figure 8. Flowchart presenting up-to-date protocols for measuring cosmogenic ^{3}He, including**
810 **the estimation of radiogenic ^{4}He and nucleogenic ^{3}He, which requires independent knowledge of**
811 **the helium closure age of a rock, t_c, except in the special case of uneroded lava flows. See text for**
812 **detailed equations, notably those for calculating the radiogenic ^{4}He production rate, P_4**
813 **(Equations 9-10) and the nucleogenic ^{3}He production rate, P_{nuc} (Equations 13-14). See section**
814 **3.5.2 for more details about the R-factor and section 3.5.3 for details about the isochron method.**
815

816 **3.5.1. Case 1, the general situation: He closure age > exposure age, but ^{4}He* is not**

817 **significantly larger than ^{4}He$_{mag}$**

818 For typical U and Th concentrations in olivine and pyroxene (1-100 ppb), the common

819 case in which ^{4}He* and magmatic ^{4}He concentrations are of comparable orders of magnitudes

820 (i.e., $0 < {}^4\text{He*}/{}^4\text{He}_{tot} < 1$) is encountered in minerals with helium closure ages younger than a

821 few tens of millions of years (Blard and Farley, 2008). In such cases, an efficient strategy is to

822 compute ^{4}He* using Equations (7)–(10); the magmatic He correction can then be performed

823 accurately using a modified version of Equation (1) (Blard and Farley, 2008):

824

825 $$^3\text{He}_c = {}^3\text{He}_{tot} - ({}^4\text{He}_{tot} - {}^4\text{He*}) \times ({}^3\text{He}/{}^4\text{He})_{mag} - {}^3\text{He}_{nuc} \,. \qquad (15)$$

826

827 In this case, the total uncertainty on cosmogenic ^{3}He can be computed applying Equation (11).

828

829 **3.5.2. Case 2: Samples with similar closure and exposure ages – the R-factor**

830 Although rare, the condition that $t_c = t_e$ applies to the case of uneroded lava flows. In

831 such cases, the accumulation of radiogenic ^{4}He and cosmogenic ^{3}He in the minerals of interest

832 (olivine, pyroxenes) starts synchronously when a lava flow cools at the Earth's surface (Blard

833 and Farley, 2008). Because $t_c = t_e$:

834

835 $$^4\text{He*} = \frac{P_4}{P_3} \times {}^3\text{He}_c \,. \qquad (16)$$

836

837 Then, using Equation (16) to substitute ^{4}He* into Equation (15), and making the reasonable

838 assumption that ^{3}He$_{nuc}$ is negligible in this case, isolating ^{3}He$_c$ on the left-hand side gives:

839 $$^3\text{He}_c = \frac{{}^3\text{He}_{tot} - {}^4\text{He}_{tot} \times \left(\frac{{}^3\text{He}}{{}^4\text{He}}\right)_{mag}}{R} \,, \qquad (17)$$

840

841 where

842

843
$$R = 1 - \frac{P_4}{P_3} \times \left(\frac{{}^{3}\text{He}}{{}^{4}\text{He}}\right)_{\text{mag}}. \qquad (18)$$

844

845   Equation (18) defines the so-called R-factor ("R" for radiogenic; Blard and Farley, 2008;
846   Blard and Pik, 2008). This approach has the advantage of including the full impact of the
847   radiogenic ${}^{4}\text{He}$ correction on the calculation of the cosmogenic ${}^{3}\text{He}$ concentration without
848   requiring any independent estimate on the helium closure age of the rock.

849   Calculating R requires only the local time-integrated production rate P_3, the ${}^{4}\text{He}^{*}$
850   production rate P_4, and the magmatic ${}^{3}\text{He}/{}^{4}\text{He}$ ratio. The lower the value of R, the greater the
851   correction arising from radiogenic ${}^{4}\text{He}$. When $R \approx 1$, the radiogenic correction is negligible
852   compared to the production of cosmogenic ${}^{3}\text{He}$, i.e., $\frac{P_4}{P_3} \cdot \left(\frac{{}^{3}\text{He}}{{}^{4}\text{He}}\right)_{\text{mag}} \ll 1$, and the magmatic
853   correction simplifies to Equation (1). However, this situation is rare in nature; modelling R for
854   different exposure altitudes and U and Th concentrations shows that R is generally < 1 (Fig. 9).
855   Importantly, in the case of lava flows used to calibrate the cosmogenic ${}^{3}\text{He}$ production rate,
856   most actual R-factors are between 0.80 and 0.95 (Blard and Farley, 2008), meaning that
857   neglecting the radiogenic ${}^{4}\text{He}$ correction would translate to underestimating ${}^{3}\text{He}_c$ by 5–20%.
858   Because some earlier studies did not perform this radiogenic ${}^{4}\text{He}$ correction, we have
859   recomputed all reported R-factors in the updated online production rate database ICE-D
860   (http://calibration.ice-d.org/), which is used as a reference by the CREp calculator
861   (https://crep.otelo.univ-lorraine.fr/#/) to compute cosmogenic ${}^{3}\text{He}$ exposure ages (Martin et al.,
862   2017).
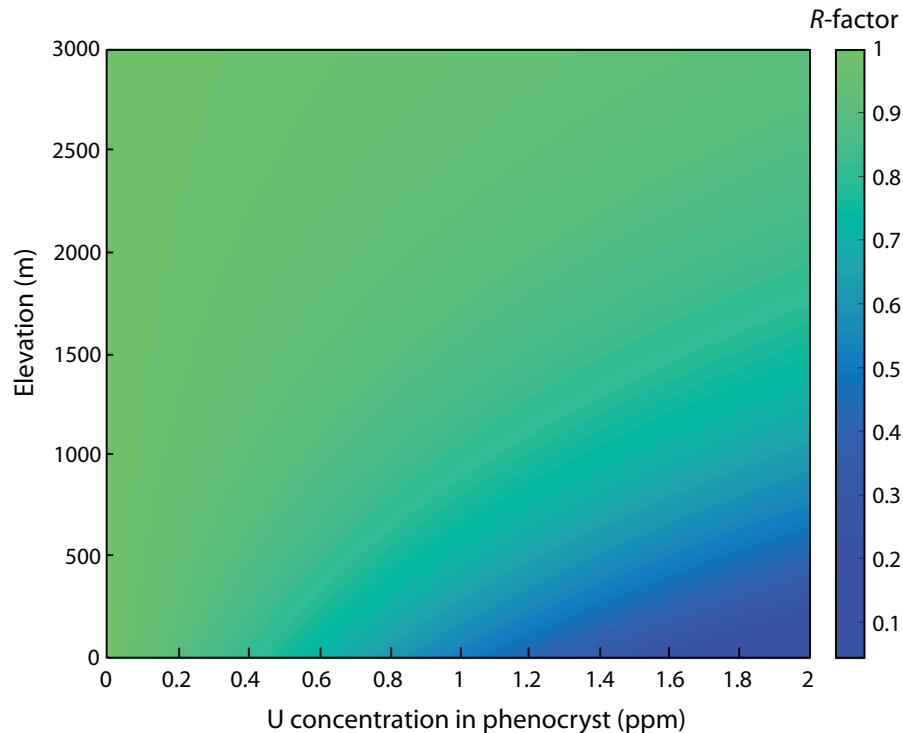
Figure 9. Modeled values of *R*-factor for uneroded lava flows as a function of U concentration in the phenocrysts and exposure elevation. Here, *R* is computed for a Th/U ratio of 3 and a magmatic ^{3}He/^{4}He ratio of 8 Ra. Implantation of ^{4}He* from surrounding lava is neglected. The equations of Stone (2000) were used to scale the sea-level ^{3}He$_c$ production rate of 124 at g^{-1} yr^{-1} (Martin et al., 2017). This simulation shows that *R* is strongly dependent on the altitude at which a lava flow is emplaced.

3.5.3. Isochrons (adequate for Cases 1 and 2)

An alternative method of estimating non-cosmogenic ^{3}He components is to fuse several aliquots of the same mineral sample and build helium isochrons. The main advantage of this isochron method is to avoid the initial in vacuo crushing step. Measured ^{3}He and ^{4}He concentrations obtained by melting different aliquots (of ~0.5 g) with variable magmatic helium concentrations define straight lines in ^{3}He$_{melt}$ *vs* ^{4}He$_{melt}$ space (this study) or (^{3}He/^{4}He)$_{melt}$ *vs* 1/^{4}He$_{melt}$ space (Blard and Pik, 2008; Cerling and Craig, 1994) (Fig. 10); these 'melt' concentrations represent total concentrations. The crushing step is thus unnecessary because the magmatic ^{3}He/^{4}He ratio is directly defined by the linear regression of an isochron. Even though the isochron method is powerful for estimating the magmatic ^{3}He contribution, note that this technique still requires the determination of potential contributions from radiogenic ^{4}He (by measuring mineral and rock U and Th concentrations and the helium closure age; see section 3.3) and nucleogenic ^{3}He components (by measuring bulk-rock major and trace elements and mineral Li concentrations; see section 3.4).

885   Below, I detail the basic equations and outcomes that can be derived from the isochron approach.

886

887   **3.5.3.1. ^{3}He *vs* ^{4}He isochrons (this study).** The general equation of the "^{3}He *vs* ^{4}He

888   isochron" is:

889

890    $$^3\text{He}_{\text{tot}} = \ ^4\text{He}_{\text{tot}} \times \left(\frac{^3\text{He}}{^4\text{He}}\right)_{\text{mag}} + \left[^3\text{He}_{\text{c}} + \ ^3\text{He}_{\text{nuc}} - \ ^4\text{He}^* \times \left(\frac{^3\text{He}}{^4\text{He}}\right)_{\text{mag}}\right]. \quad (19)$$

891

892   This corresponds to the equation of a line, $y = ax + b$, in which the slope a is $(^3\text{He}/^4\text{He})_{\text{mag}}$

893   and the y-intercept b is the sum of all components that are independent of the magmatic

894   component, including cosmogenic ^{3}He (Fig. 10A). $^3\text{He}_{\text{c}}$ can then be estimated after correcting

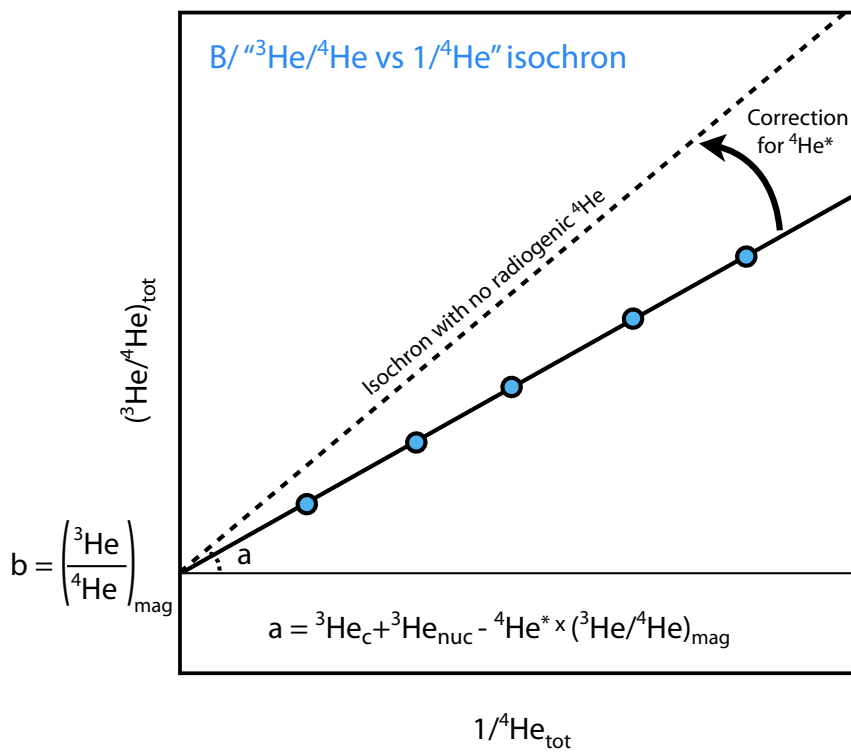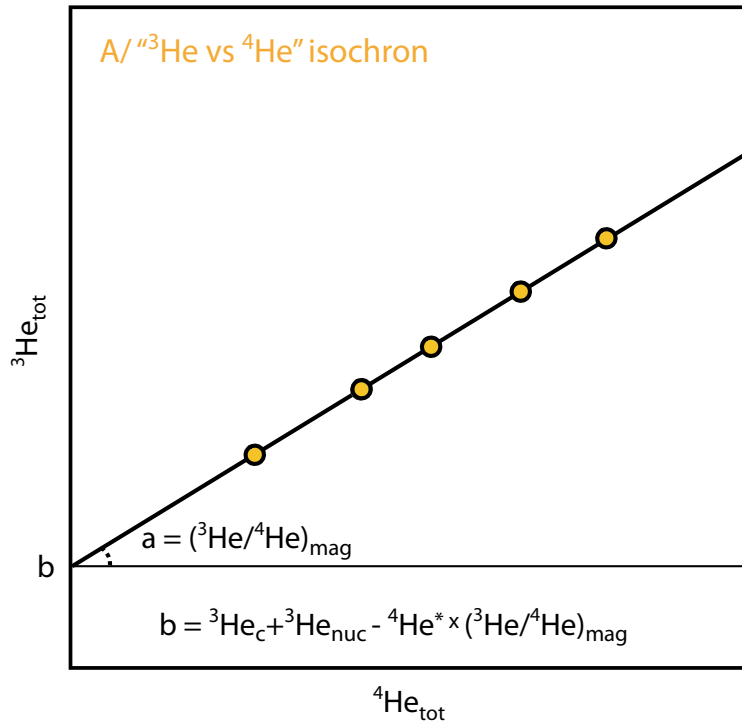895   for the nucleogenic ^{3}He and radiogenic ^{4}He components as:

896

897    $$^3\text{He}_{\text{c}} = b + \ ^4\text{He}^* \times a - \ ^3\text{He}_{\text{nuc}} . \quad (20)$$

898

899   In the specific case of uneroded lava flows, the radiogenic ^{4}He correction may be simplified

900   using the R-factor (Eq. 18) to:

901

902    $$^3\text{He}_{\text{c}} = \frac{b}{R} . \quad (21)$$

A/ "^{3}He vs ^{4}He" isochron

^{3}He$_{tot}$

$a = (^3He/^4He)_{mag}$

b

$b = ^3He_c + ^3He_{nuc} - ^4He^* \times (^3He/^4He)_{mag}$

^{4}He$_{tot}$

B/ "^{3}He/^{4}He vs 1/^{4}He" isochron

Correction for ^{4}He*

Isochron with no radiogenic ^{4}He

$(^3He/^4He)_{tot}$

$b = \left(\dfrac{^3He}{^4He}\right)_{mag}$

a

$a = ^3He_c + ^3He_{nuc} - ^4He^* \times (^3He/^4He)_{mag}$

1/^{4}He$_{tot}$

Figure 10. Cosmogenic ^{3}He isochrons: (A) "^{3}He *vs* ^{4}He isochron" (this study) and (B) "^{3}He/^{4}He *vs* 1/^{4}He isochron" (Blard and Pik, 2008; Cerling and Craig, 1994).

38

909   **3.5.3.2. ^{3}He/^{4}He *vs* 1/^{4}He isochrons (Blard and Pik, 2008; Cerling and Craig, 1994).**

910   The general equation of the "^{3}He/^{4}He *vs* 1/^{4}He isochron" is:

911

912
$$\left(\frac{^3\text{He}}{^4\text{He}}\right)_{\text{tot}} = \left[^3\text{He}_c + {}^3\text{He}_{\text{nuc}} - {}^4\text{He}^* \times \left(\frac{^3\text{He}}{^4\text{He}}\right)_{\text{mag}}\right] \times \frac{1}{^4\text{He}_{\text{tot}}} + \left(\frac{^3\text{He}}{^4\text{He}}\right)_{\text{mag}} . \qquad (22)$$

913

914   Again, this corresponds to the equation of a line, but in this case the *y*-intercept is $(^3\text{He}/^4\text{He})_{\text{mag}}$

915   and the slope is the sum of "magmatic-independent" components, including cosmogenic ^{3}He

916   (Fig. 10B). ^{3}He$_c$ can then be estimated after correcting for the nucleogenic ^{3}He and radiogenic

917   ^{4}He components as:

918

919
$$^3\text{He}_c = a + {}^4\text{He}^* \times b - {}^3\text{He}_{\text{nuc}} . \qquad (23)$$

920

921   Using the R-factor in the specific case of uneroded lava flows, the radiogenic ^{4}He correction

922   may be simplified to:

923

924
$$^3\text{He}_c = \frac{a}{R} . \qquad (24)$$

925

926   Note that the mathematical regression of the "^{3}He/^{4}He *vs* 1/^{4}He isochron" requires computing

927   the correlation factor ρ_{err} between the $(^3\text{He}/^4\text{He})_{\text{tot}}$ and $1/^4\text{He}_{\text{tot}}$ uncertainties:

928

929
$$\rho_{\text{err}} = \frac{\sigma_4/{}^4He}{\sqrt{(\sigma_3/{}^3He)^2 + (\sigma_4/{}^4He)^2}} . \qquad (25)$$

930

931   To achieve the best isochron regression, statistical parameters (MSWD, York, 1966)

932   should be calculated using modern numerical tools, such as the online version of IsoplotR

933   (http://isoplotr.es.ucl.ac.uk/; Vermeesch, 2018). Although, in its current version, IsoplotR does

934   not include a specific tool for computing cosmogenic ^{3}He, this is easily done using the generic

935   functions of "other *x vs y* regressions" in this online software. Even if both isochron types yield

936   equivalent results, the "^{3}He/^{4}He *vs* 1/^{4}He isochron" is more suited to defining the magmatic

937   (^{3}He/^{4}He) ratio, but also requires calculating the correlation factor ρ_{err}.

938

939

3.5.4. Case 3: Samples with large amounts of radiogenic $^4He^*$ ($^4He^* \gg {}^4He_{mag}$)

In this case, the amount of ^4He extracted by fusion is similar to, and indistinguishable from, the radiogenic $^4He^*$ concentration within analytical uncertainties. In other words, the magmatic ^4He component is below the detection limit. This occurs for long closure ages (typically $\gg 10^6$ yr) or in minerals with particularly high U-Th concentrations ($\gg 10$ ppm), such as zircons. In such a situation, using the total amount of ^4He extracted by fusion to estimate the concentrations of magmatic ^4He and ^3He is misleading, even when applying Equation (15). This may induce major uncertainties, and indeed potential inaccuracies, on the final cosmogenic ^3He concentrations (Fig. 6). However, it is not always straightforward to diagnose this extreme case, notably because, in practice, there exists a continuum between situations where $^4He^* \approx {}^4He_{mag}$ and those where $^4He^* \gg {}^4He_{mag}$. If the closure age and the U-Th concentrations of the mineral of interest are well known, one can determine if $^4He^* \gg {}^4He_{mag}$ by calculating the amount of $^4He^*$ and comparing it with the total amount of ^4He extracted by fusion. Another way to pose this diagnostic is the impossibility of building isochrons: fused aliquots will present significant scatter in $^3He_{tot}$ vs $^4He_{tot}$ space and will not align on a straight line, displaying errorchrons. Since this case occurs for closure ages $\gg 1$ Ma, the nucleogenic ^3He contribution may be significant. This correction must therefore be considered carefully, using an accurate and precise estimate of the helium cooling age.

If it is established that $^4He^* \gg {}^4He_{mag}$, an alternative strategy must be employed to estimate the magmatic ^3He correction. The most efficient alternatives are:

1) Find and fuse a sample of the same lithology that has been shielded from cosmic rays to estimate the magmatic and nucleogenic ^3He components (e.g., Amidon et al., 2009). This assumes that the magmatic ^3He component is homogeneous.

2) Prolonged in vacuo crushing (10 min, 100 strokes) of an aliquot of the same sample that has been dated by cosmogenic ^3He. This allows the extraction of the majority of the magmatic ^3He, which can be used to perform the magmatic ^3He correction (Blard et al., 2009; Martin et al., 2018).

Note that these strategies may be sources of undetected inaccuracies, for example due to unrecognized magmatic or nucleogenic ^3He components. Thus, when it is determined that $^4He^* \gg {}^4He_{mag}$, it is key to minimize the contribution of magmatic helium by selecting samples in the 100–500 µm size fraction (Puchol et al., 2017; Williams et al., 2005) or use prescreening methods to select inclusion free minerals (Hofmann et al., 2021).

4. Analytical methods for measuring ^{3}He and ^{4}He in minerals

4.1. Extraction procedure

As mentioned in sections 2.1 and 3.1, different extraction techniques must be used to selectively release the different helium components: measuring magmatic helium requires crushing in vacuo, whereas the complete extraction of cosmogenic ^{3}He requires that minerals be heated at high temperatures and melted, using a high-vacuum, high-temperature furnace or a laser.

4.1.1. In-vacuo crushing

This method is suited to selectively releasing the magmatic component from minerals of interest (e.g. olivine, pyroxene) (Kurz, 1986a, 1986b). The several types and sizes of available crushers can accommodate different sample sizes with variable crushing efficiency (Blard et al., 2008; Scarsi, 2000). Typical crushers comprise ~50–100-g stainless steel cylinders that are moved in vacuo by external solenoids (Kurz, 1986a; Yokochi et al., 2005). The associated ^{3}He and ^{4}He blanks of ~5 × 10^3 and 5 × 10^8 atoms per minute of crushing, respectively (Blard et al., 2008). Typical sample sizes are 0.5–1 g of solid materials; larger samples require a larger crusher to ensure crushing efficiency. If samples are too poor in magmatic helium to yield high signal/blank ratios, the isochron approach may be a useful alternative because it obviates the magmatic crushing step (e.g., Marchetti et al., 2020).

4.1.2. Heating furnace systems

High-temperature heating (1300-1500 °C for pyroxene, 1500-1800°C for olivine) is necessary to extract the entire cosmogenic ^{3}He component present in samples, either by achieving total diffusion or melting. Double-vacuum resistance furnaces are ideal because they can be used to heat sample sizes ranging from 100 mg to 2 g (e.g., Amidon et al., 2009; Kurz, 1986b; Margerison et al., 2005). These apparatuses have typical ^{4}He blanks in the range of 10^8– 10^{10} atoms when heating at 1500 °C for 15 minutes (see review by Zimmermann et al., 2018). For most analyzed concentrations, such amounts of phenocrysts (0.1–2 g) are necessary to ensure sufficiently high signal/blank ratios. It is important to note that all mineral samples must be weighed and wrapped in metal foils (e.g. Sn, Al, Cu) before being loaded into the furnaces. Recently, Zimmermann et al., (2018) developed and patented a new all-metal single-vacuum furnace whose crucible is heated by induction (Fig. 11). As the mass of heated metal is small compared to classical double-vacuum resistance furnaces, this design ensures better blanks (^{4}He

1008 $= (5 \pm 2) \times 10^8$ atoms for 15 min at 1500 °C), faster heating and cooling rates (400 °C min⁻¹),

1009 improved robustness, lower functional costs, and, for models equipped with a thermocouple or

1010 thermal camera, improved temperature control.

1011
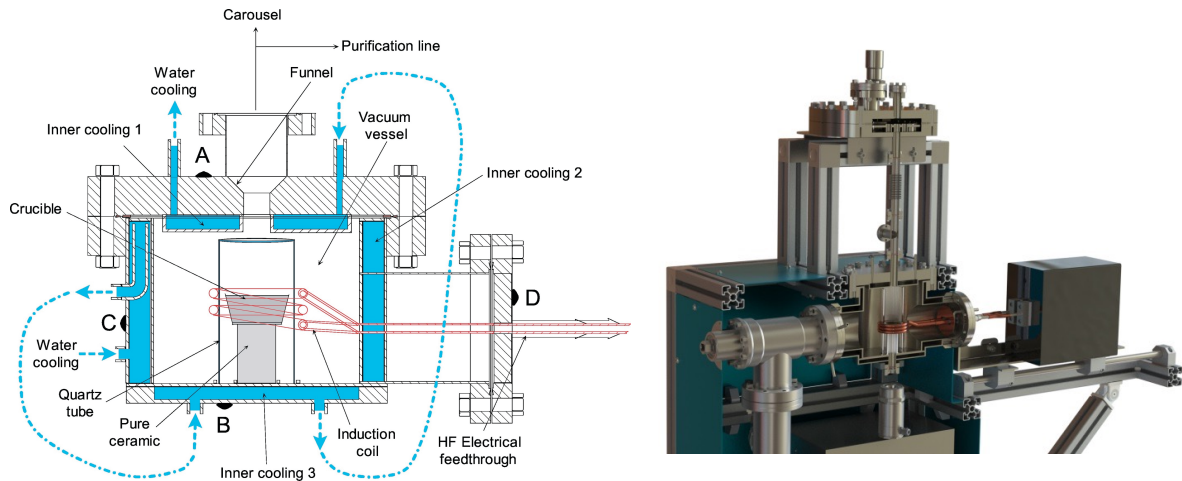
1012

1013

1014 **Figure 11. Newly patented all-metal single-vacuum induction furnace (Zimmermann et al., 2018)**
1015 **allowing 1-g samples to be heated to 2000 °C in less than 5 minutes. Photo credit:**
1016 **©Cryoscan/CNRS/Satt-Sayens**

1017

1018 ### 4.1.3. Lasers

1019 Depending on their wavelength, lasers may either be used for ablation or heating. Although

1020 this extraction system is best suited for ^{3}He-rich extraterrestrial materials (e.g., Megrue, 1971),

1021 the utility of lasers is limited for terrestrial cosmogenic ^{3}He. When they are used to directly heat

1022 minerals, laser beams can only heat a maximum of 10 mg of material (less in the case of

1023 ablation), with ^{4}He blanks on the order of 10^8–10^9 atoms, implying lower signal/blank ratios

1024 compared to furnaces (Zimmermann et al., 2018). Note that BGC recently developed a laser

1025 "microfurnace" system, in which a sample of up to ~200 mg can be analyzed in a crimped

1026 tantalum tube heated with a diode laser (Balter-Kennedy et al., 2020).

1027

1028 When the uncertainty attached to the blank correction is propagated to the measured ^{3}He

1029 and ^{4}He concentrations, what matters is the absolute standard deviation on the blank level.

1030 Hence, to get an accurate estimate of the blank variance, it is important to run several blanks of

1031 an extraction apparatus. This must be done under strictly similar duration and temperature

1032 conditions to ensure that the blank variability is as low as possible.

4.2. Purification lines

After gas extraction by crushing or heating, it is necessary to remove the undesirable gas before analyzing the ^{3}He and ^{4}He concentrations. Pressures may indeed reach 10^{-3} mbar in hot furnaces, whereas most analyzers must be operated at pressures lower than 10^{-6} mbar to preserve their integrity and ensure accurate analysis. In most modern labs, this gas purification consists of sequentially releasing the sample in successive volumes of a stainless steel ultra-vacuum line, in which physical (e.g. charcoal cooled by liquid nitrogen at -196 °C) and chemical traps (e.g. SAES getters, titanium sponges) remove most hydrocarbons, CO_2, H_2O, H_2, and heavy noble gases (Xe, Kr, Ar) (e.g. Blard et al., 2015). Then, a cryogenic sorber (or "cryopump") is often used in the final part of the line to trap He and Ne at temperatures <10 K, before being heated above 35 K to selectively release helium into the analyzer. This last purification step both removes neon and maximizes the helium signal.

4.3. Mass spectrometry

Mass spectrometers operated in static mode remain the most precise, accurate, and sensitive instruments for measuring helium isotopes in solid minerals. Since the invention of Nier-type sources (Fig. 12; De Laeter and Kurz, 2006), the main improvements have been in the design, materials, and detector sensitivity. State-of-the-art analytical instruments for measuring ^{3}He and ^{4}He abundances are stainless steel mass spectrometers with Nier-type sources, such as the Noblesse AN37 or the ThermoFisher SFT ("Split Flight Tube"; Fig. 12). The geometry of the SFT flight tube is designed to minimize the analytical volume (1400 cc) while simultaneously collecting ^{4}He on a Faraday cup (with 10^{10}–10^{12} Ω amplifiers) and ^{3}He on an electron multiplier. Whereas mono-collection mass spectrometers require peak jumping, this bi-collection of helium isotopes improves analytical stability and speed. The resolution on the electron multiplier is 700, ensuring the complete separation of ^{3}He$^+$ from the isobars HD$^+$ and HHH$^+$. Sensitivities of the Thermo SFT and the Noblesse AN37 are comparable, in the range of 0.1-0.2 A/bar.
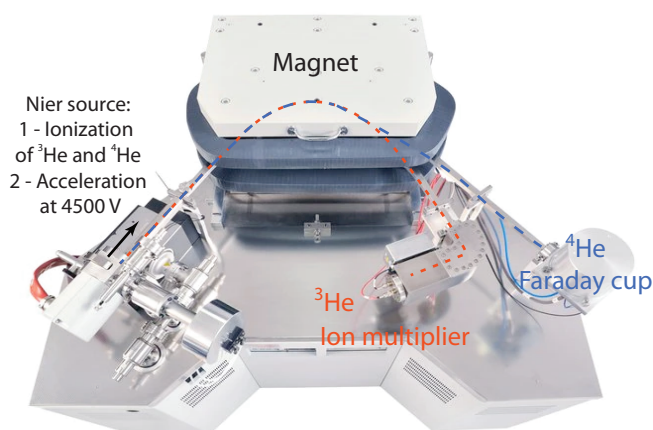
Figure 12. (Left) A photograph taken in 1940 of Alfred O. C. Nier (1911–1994) showing the glass mass spectrometer that he developed and which was used to measure ^{4}He (De Laeter and Kurz, 2006). (Right) A modern all-metal ©ThermoFisher SFT spectrometer.

The most promising recent development in noble gas mass spectrometry is the creation of the compressed ion source, which can increase instrumental sensitivity for helium by one to two orders of magnitude (Baur, 1999; Matsumoto et al., 2010). For now, however, this advancement remains theoretical because, in practice, measurements are limited by the blank levels of the extraction system and, more importantly, by the presence of non-cosmogenic helium in samples. To fully exploit this progress in the sensitivity of noble gas mass spectrometers, parallel analytical developments must focus on reducing blanks and selecting minerals with the lowest possible non-cosmogenic ^{3}He concentrations.

4.4. Interlaboratory comparisons

To identify potential sources of systematic and random uncertainties in ^{3}He and ^{4}He measurements, interlaboratory comparisons performed by analyzing splits of the same standard mineral material provide useful insights (Blard et al., 2015; Vermeesch et al., 2015). Recently, six international laboratories (GFZ, Potsdam; Caltech, Pasadena; CRPG, Nancy; SUERC, Glasgow; BGC, Berkeley; Lamont Doherty Earth Observatory, New York) participated in an intercomparison experiment (Blard et al., 2015), analyzing 5–22 aliquots of the CRONUS-P pyroxene standard, which has been shown to be homogeneous (Schaefer et al., 2016). Adding the 17 analyses recently performed at BGC (with the new "Ohio" system, Balter-Kennedy et al., 2020), this interlaboratory dataset (totaling 83 determinations from the six laboratories; Fig. 13) is characterized by a global weighted mean of $(5.02 \pm 0.05) \times 10^9$ at ^{3}He g^{-1} (1σ) with an overdispersion of 2.6% (1σ). ^{4}He is characterized by a larger variability than ^{3}He, with a global

weighted mean of $(3.60 \pm 0.09) \times 10^{13}$ at ^{4}He g^{-1} (1σ) with an overdispersion of 5.2% (1σ) (Blard et al., 2015). This interlaboratory overdispersion probably reflects systematic differences between the six laboratories, since the overdispersion is, by definition, larger than the analytical uncertainties. To further evaluate this and homogenize datasets, thereby improving the accuracy of cosmogenic ^{3}He dating, all future studies should measure the CRONUS-P standard as part of their analyses. Potential sources of systematic uncertainties that may explain these previously overlooked interlaboratory offsets are discussed in the next subsection.
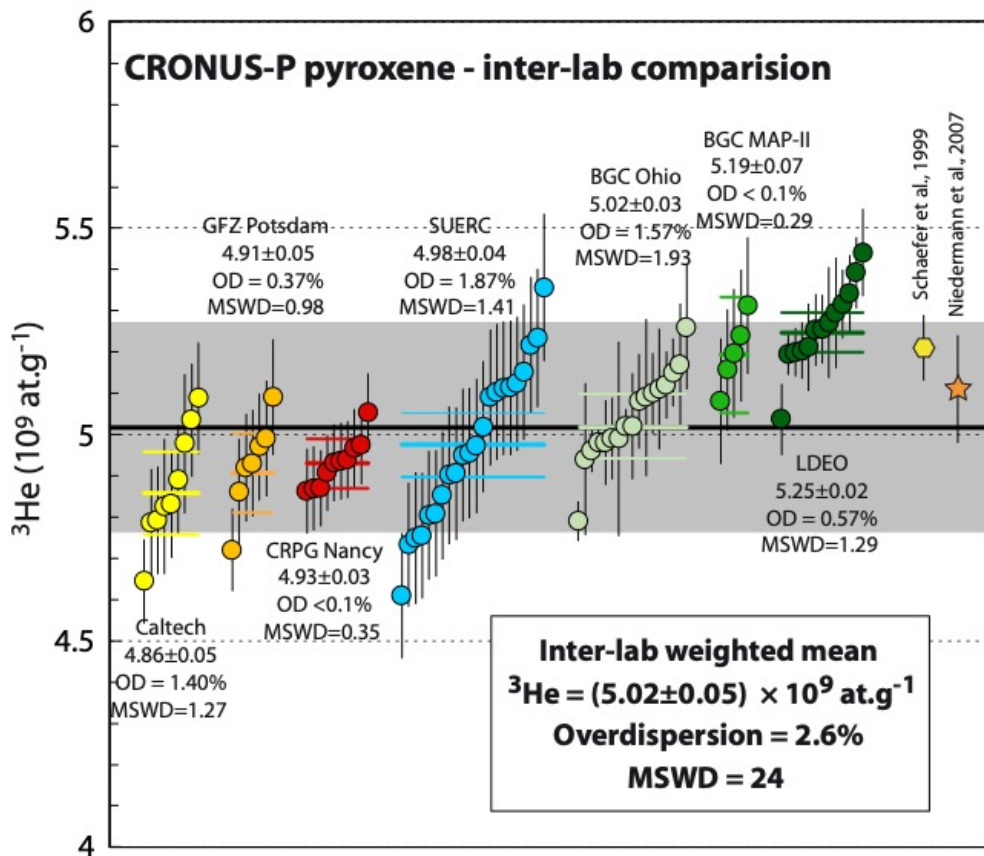
Figure 13. Interlaboratory comparison of ^{3}He concentrations measured in the CRONUS-P pyroxene standard (n = 83). Note that I updated here the initial dataset of (Blard et al., 2015) to incorporate the data recently obtained by the "Ohio" analytical system of BGC (Balter-Kennedy et al., 2020). Plotted individual analytical uncertainties are at 1σ. For each lab are given the weighted means with their standards errors at 1σ (color horizontal bars show the 2σ range), the intra-lab overdispersion (OD, 1σ) and the MSWD. This statistical analysis was performed with the online tool IsoplotR (www.ucl.ac.uk), computing the weighted mean using a random effects model with two sources of uncertainty: the analytical uncertainty and an overdispersion term (Vermeesch 2018). Overdispersion describes the interlaboratory variance that is not included in the analytical uncertainties. Hence, computed overdispersion also depends on the analytical uncertainties reported by each lab. The standard error of the global weighted mean and the inter-lab overdispersion are given at 1σ (grey area show the 2σ range). Early measurements by (Niedermann et al., 2007; Schäfer et al., 1999) are also shown.

4.5. Potential sources of systematic uncertainties in ^{3}He and ^{4}He measurements

Various analytical issues may lead to potentially overlooked biases and contribute to the systematic differences in the ^{3}He and ^{4}He concentrations measured in different laboratories. Nonetheless, as some such biases have been recognized in some laboratories, discussing them openly and suggesting possible control benchmarks is a first step toward improving analytical precision and accuracy in all laboratories.

i) ***Estimate of the initial pressure in gas standard tanks.*** Nearly all laboratories use a gas standard as a primary reference to calibrate the sensitivities of their mass spectrometers. For this, it is vital to properly estimate the initial helium pressure (i.e., the number of ^{3}He and ^{4}He atoms) in the gas tank. This determination must be as accurate as possible, but depends on the non-linear behavior of capacitance manometers or the use of poorly calibrated volumes during dilution of the calibration gas in the reservoir. When a new gas standard is prepared, a useful experiment is to cross-check the measured initial pressure against a measurement of a mineral standard material, such as CRONUS-P.

ii) ***Tank depletion after several standard iterations***. For daily calibration procedures, laboratories generally extract a small aliquot (<1 cc) from a large bottle of the gas standard (typically 2 L). Although the aliquot volume is small compared to the standard reservoir volume (ratio $\sim 10^{-4}$), it is essential to know the volumes of both the aliquot and the standard bottle to correctly calculate the amount of standard gas remaining in the bottle over time. See Fleck and Calvert (2014) for a complete discussion of the most accurate depletion equation. Modern automated extraction systems can use $>10^3$ standard aliquots per year; hence, a small initial bias on the aliquot/bottle volume ratio may be significantly amplified over several years of standard use. Thus, even if the gas standard remains the most convenient for daily calibrations, regularly cross-checking against a mineral standard material is again a useful and important control routine.

iii) ***Volumetric calibration of the extraction and purification line.*** Since pressure may reach high values ($>10^{-5}$ mbar) in furnaces operating at >1000 °C, it is often necessary to split the extracted gas to remove the gas fraction in the "dirty" part

of the purification line. Depending on the line design, this may imply that dilution routines differ between mineral samples and gas standards. Correcting for this dilution requires precise and accurate knowledge of the volumes involved. Extraction line volumes are generally determined with capacitance manometers at pressures between a few millibars and 1 bar. This measurement may be biased by adsorption onto the internal surfaces and thus overestimate the true volume. It is therefore particularly complicated to estimate volumes in which chemical and physical traps are present. Hence, when possible, splitting and dilution should be avoided or limited to a small fraction of the gas to reduce potential inaccuracies. Ideally, cryofocusing is useful for avoiding this issue and applying the same dilution to samples and standards.
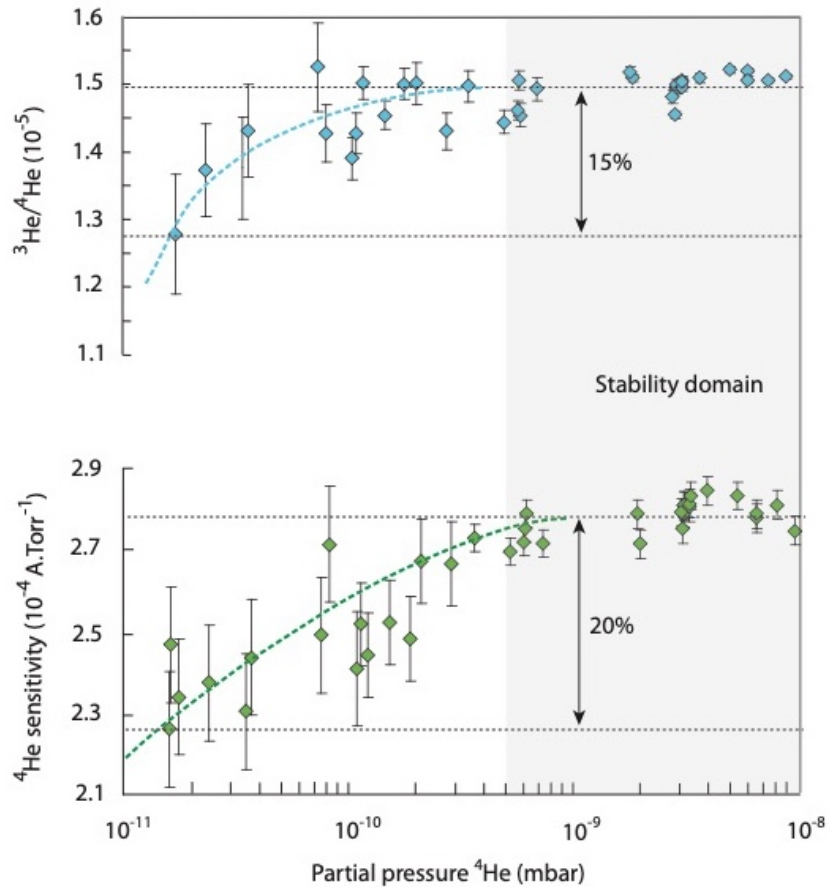
iv) ***Overly efficient and unknown He cryotrapping in the presence of heavier noble (Ne) or other gases.*** In most laboratories, helium is trapped by a sorber head that is cooled to <10 K before being released into the last part of the extraction line at 35 K, the empirically established vacuum-release temperature for helium in most cryopump systems. This cryotrapping step is useful because it optimizes helium purification and separation from other noble gases. Because the cryopump is generally placed in the last part of the purification line, cryofocusing also maximizes the pressure of the gas being input into the mass spectrometer, improving the sensitivity of the entire analytical system. At CRPG, we tested the impact of the release temperature by measuring the helium signal obtained at various temperatures between 35 and 100 K (unpublished data): when analyzing pure helium gas, 35 K is sufficient to release 100% of the helium that was previously trapped on the cryopump sorber head. However, when analyzing helium extracted from silicates, 5% of the total helium remained trapped at 35 K, and heating to 70 K was necessary to release the totality of the sample's helium. Hence, it is possible that the release temperature of helium from the cryopump sorbing step depends on the He/Ne ratio, or on the presence of other gases that were not removed in the upstream part of the purification line. These observations are not sufficient to define a clear relationship between the helium trapping and release temperatures and the ratio of He to other gases, and more attention should be given to this issue. New experimental data with

1175	variable He/(other gas) ratios would be useful for improving the accuracy of He
1176	isotopic measurements.
1177	
1178	**v)** ***Pressure effects on the linearity of mass spectrometer sensitivity.*** Empirical
1179	observations have shown that the amount of helium present in the mass
1180	spectrometer may modify instrumental sensitivity when measuring ^{3}He and ^{4}He
1181	(Fig. 14; Burnard and Farley, 2000; Mabry et al., 2013; Sano et al., 2008). This
1182	effect is more pronounced at low helium pressures ($<10^{-9}$ mbar) and may reach
1183	20% in the worst situations (Sano et al., 2008; Zimmermann and Bekaert, 2020).
1184	The mechanisms producing this pressure dependence are not well constrained,
1185	but such instrumental fractionation could occur in a Nier-type source due to a
1186	space-charge effect on the ionization efficiency (Burnard and Farley 2000).
1187	Other possible mechanisms might involve the flight tube or the detectors (Sano
1188	et al., 2008). Importantly, this pressure effect varies significantly from one mass
1189	spectrometer to another (Sano et al., 2008) and is sensitive to the source settings,
1190	notably the trap current (Burnard and Farley, 2000; Mabry et al., 2013).

To minimize the potential bias arising from this pressure effect, source settings should be optimized to define the largest possible zone of stability (Fig. 14). Lower trap currents (50–200 μA) minimize this non-linearity. If it is not possible to suppress this instrumental fractionation, it is important to analyze similar amounts of gas standard and sample. Since this procedure often requires splitting gas standards, the volume of the preparation line must be accurately calibrated. Alternatively, this issue could be overcome by using He-poor gas standards: if a single pipette delivers a low-pressure helium signal in the range 10^{-11}–10^{-10} mbar, the dilution step will be unnecessary. Because the presence of other gases may also affect this instrumental bias (see above), it may be useful to ensure that samples and standards are of similar helium purity, notably He/Ne ratios. This can be achieved either by cryo-separation of neon and helium or by performing a quick scan of the amount of ^{20}Ne in the sample using a quadrupole installed on the purification line. A neon spike may then be used to adjust the He/Ne ratio of the helium standard to be similar to that of the sample.

1206

1207

1214

1215

      vi)   *Variations of the absolute ^{3}He/^{4}He atmospheric ratio.* Many gas standards are prepared using atmospheric helium that is artificially enriched in ^{3}He (e.g. Matsuda et al., 2002). Other standards are natural magmatic gases with ^{3}He/^{4}He ratios greater than that of the atmosphere (e.g. Blard et al., 2015). In either case, gas standards must be cross-calibrated against a gas of known composition to determine their absolute He contents and ^{3}He/^{4}He ratios. This is often performed against atmospheric helium, because the ^{3}He/^{4}He ratio in this reservoir is spatially homogeneous with a variability lower than 2‰ (95% confidence interval; Boucher et al., 2018). However, for absolute determinations of ^{3}He, it is vital to know with accuracy the absolute value of the atmospheric ^{3}He/^{4}He

49

1226	ratio. The few studies that have attempted to measure the absolute $^3He/^4He$ ratio
1227	in air (Clarke et al., 1976; Hoffman and Nier 1993; Lupton and Graham 1991;
1228	Mamyrin et al., 1970) yield a weighted average of $(1.386 \pm 0.005) \times 10^{-6}$ (1σ;
1229	Boucher et al., 2018). However, a few studies have reported values beyond this
1230	range; notably, Sano et al., (2008) analyzed air collected in the center of Tokyo
1231	(Japan) and obtained a ratio of 1.34×10^{-6}, ~3.5% lower than the world average,
1232	suggestive of a potential ^4He enrichment by a local anthropogenic source.
1233	Moreover, temporal variations of the atmospheric $^3He/^4He$ ratio are possible
1234	(Sano et al., 2010), but this effect is probably smaller than 1% in the Northern
1235	Hemisphere over the past 40 years (Mabry et al., 2015).
1236	

1237   In summary, all these sources of systematic uncertainties may accumulate, leading in

1238 the worst cases to under-/over-estimates and interlaboratory discrepancies larger than 5%. To

1239 reduce these potential inaccuracies and improve interlaboratory comparisons, it is highly

1240 recommended that future studies analyze solid standard materials alongside each sample batch,

1241 such as the CRONUS-P pyroxene mineral standard (Schaefer et al., 2016; Blard et al., 2015).

5. Discussion: cosmogenic ³He production rates, the accuracy of spatial scaling, cross-calibration with other cosmogenic nuclides, online calculators and new frontiers

5.1. Production rates

Knowing cosmogenic ³He production rates accurately and precisely is important because this parameter is involved in all applications of cosmogenic ³He, notably in calculating surface exposure ages. Production rates are spatially variable (Gosse and Phillips 2001; Lal, 1991; Lal and Peters 1967) because the Earth's magnetic field controls the flux and repartition of incoming primary charged cosmic particles (Dunai 2001; Lal, 1991; Lal and Peters 1967), and because atmospheric shielding results in elevation-dependent production rates (Hess 1912; Lal, 1991; Lal and Peters 1967; Pacini et al., 1911; Stone 2000). Hence, scaling models are necessary to calculate the production rate at a given sampling location by accounting for spatial characteristics (altitude, latitude, longitude) and exposure duration. Such scaling models were initially established from empirical relationships linking production rate to latitude, longitude, and altitude based on physical observations of the reactions triggered by cosmic particles (Balco et al., 2008). Recent scaling models based on ab-initio physical modeling efficiently describe the spatial variability of production rates (Argento et al., 2013; Lifton et al., 2014). However, geological calibration sites for cosmogenic nuclide production rates are necessary to ground truth and refine these models (Borchers et al., 2016; Martin et al., 2017). A production rate calibration site is a continuously exposed geomorphological surface that has gone uneroded and uncovered since its emplacement at the surface, and whose exposure age can be determined independently with accuracy and precision (e.g., by ¹⁴C, K-Ar, or luminescence dating). If a scaling model is accurate, all calibration sites should yield the same normalized production rate, within uncertainties, after the dataset is scaled to sea level and high latitude (>60°; SLHL).

5.2. The global ³He_c production rate calibration database

Figure 15A shows the locations of the 24 production rate calibration sites available in the literature (Ackert et al., 2003; Amidon and Farley 2011; Blard et al., 2013; Blard et al., 2006; Borchers et al., 2016; Cerling and Craig, 1994; Delunel et al., 2016; Dunai and Wijbrans 2000; Eaves et al., 2016; Fenton et al., 2009; 2013; Foeken et al., 2012; Goehring et al., 2010; Licciardi et al., 2006; Licciardi et al., 1999). The SLHL ³He production rates presented in Figure 15B–E were computed from this empirical dataset using the CREp calculator (https://crep.otelo.univ-lorraine.fr/#/).Whereas the compilation of Borchers et al., (2016) only considers a limited subset of the data, this up-to-date synthesis integrates all published raw
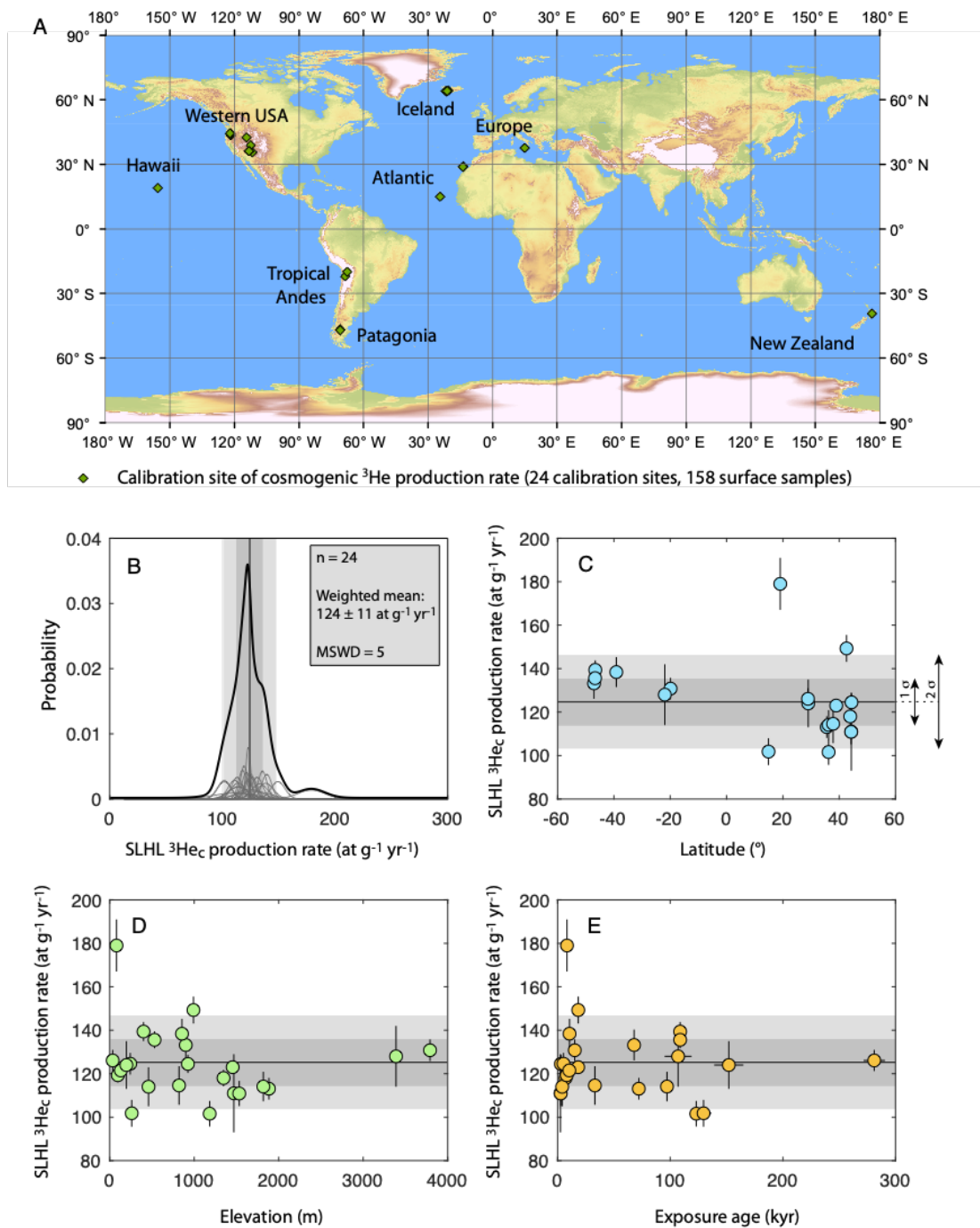
1276   calibration data from the 24 calibration sites, which are available in the ICE-D online database

1277   (http://calibration.ice-d.org/). Contrary to the compilation of (Goehring et al., 2018), this

1278   updated synthesis also ensures that all ^3He_c concentrations are corrected for radiogenic ^4He,

1279   which amounts to a 1–5% correction at a few sites (Blard and Farley, 2008). The SLHL and

1280   time corrections presented in Figure 15 were performed with the Lifton-Sato-Dunai (LSD)

1281   scaling scheme (Lifton et al., 2014), the ERA-40 atmospheric model, and the Virtual Dipole

1282   Moment (VDM) dataset, derived from atmospheric ^{10}Be (Muscheler et al., 2005). This analysis

1283   shows that there is no clear correlation between SLHL P_3 and the latitudes, altitudes, or

1284   exposure durations of these calibration surfaces, suggesting that this time-dependent scaling

1285   model is accurate for the majority of the calibrated production rates (Balco et al., 2008). This

1286   dataset defines a worldwide average weighted mean of 124 ± 11 at g^{-1} yr^{-1} with MSWD = 5

1287   (Fig. 15B). For comparison, the Lal-Stone time-dependent scheme (Balco et al., 2008) yields a

1288   larger dispersion (MSWD = 7), suggesting that the LSD model performs slightly better, at least

1289   for ^3He (Borchers et al., 2016; Martin et al., 2017). When plotted against exposure duration,

1290   SLHL P_3 values scaled with the Lal-Stone model present a slight negative correlation (i.e.,

1291   lower P_3 values for longer exposure times >100 ka); this is not the case with the LSD scaling.

1292   Tests of the different atmospheric models have shown that the spatially distributed

1293   ERA-40 atmospheric grid (Uppala et al., 2005) performs better than the standard atmosphere

1294   model (Stone 2000) in reducing the scatter on SLHL P_3 (Martin et al., 2017). Similarly, the

1295   VDM database (Muscheler et al., 2005) yields the lowest dispersion (Martin et al., 2017).

1296   However, local inaccuracies persist and require further investigation and additional data and

1297   calibration sites: 4 of the 24 calibration sites yield SLHL P_3 values stand beyond 2 weighted

1298   standard deviations. For example, in Western Africa, a calibration site on Fogo Island (Cabo

1299   Verde) yielded a SLHL P_3 value that is particularly low, 2σ below the weighted average

1300   (Foeken et al., 2012). Future calibration studies in these regions will indicate whether this

1301   outlier is due to an improper independent K-Ar date or unrecognized erosion, or whether it

1302   results from an as yet unrecognized local anomaly such as high atmospheric pressure or a

1303   specific magnetic field anomaly (Lifton et al., 2014). In contrast, the Hawaiian calibration site

1304   yields a SLHL P_3 more than 2σ above the global average, suggesting either inaccuracy in the

1305   independent dating or in the atmospheric or temporal correction.

1306   To reduce potential inaccuracies in the spatial scaling, local calibration sites should

1307   generally be favored over the use of a global average, particularly in low-latitude, high-altitude

1308   sites. A local calibration site should ideally be as close as possible to the site to be dated. When

1309   the horizontal/vertical distance between the object to be dated and the calibration site is less

1310   than 1,000 km/1,000 m, discrepancies between scaling models remain within analytical
1311   uncertainties (Martin et al., 2018). However, in practice, many regions do not have any ^{3}He
1312   calibration sites (Fig. 15A), hindering the use of a local calibration to compute exposure ages.
1313   The case of the High Tropics is particularly important, since the altitude and magnetic field
1314   corrections are extreme in these regions, inducing large differences between the different
1315   scaling schemes. The use of a global-averaged production rate there may hence yield large
1316   discrepancies between ages computed with different scaling schemes. The sole calibration sites
1317   of the High Tropics are located in the Tropical Andes (e.g. Blard et al., 2013; Delunel et al.,
1318   2016), whereas none have been established in Africa, Eurasia, or Oceania. Future calibration
1319   studies could also focus on all elevation zones of Eurasia, Oceania, Africa, Central America,
1320   Greenland, and Antarctica, where calibration sites are scarce or absent (Fig. 15A). High-
1321   elevation, high-latitude calibration sites are also poorly represented.
1322

Figure 15. (A) Calibration sites for cosmogenic [3]He production rates available in the ICE-D calibration database (24 calibration sites, 158 surface samples). (B) The distribution of production rates and (C–E) production rate variations with latitude, elevation, and exposure age, respectively, were computed and plotted using the online CREp calculator (https://crep.otelo.univ-lorraine.fr/). SLHL and time corrections were performed here with the LSD scaling scheme (Lifton et al., 2014) using the ERA-40 atmospheric model and the VDM dataset derived from atmospheric [10]Be (Muscheler et al., 2005). Source articles of the [3]He calibration site dataset: (Ackert et al., 2003; Amidon and Farley 2011; Blard et al., 2013; Blard et al., 2006; Borchers et al., 2016; Cerling and Craig, 1994; Delunel et al., 2016; Dunai and Wijbrans 2000; Eaves et al., 2016; Fenton et al., 2009; 2013; Foeken et al., 2012; Goehring et al., 2010; Licciardi et al., 2006; Licciardi et al., 1999).

5.3. Online calculators

Three main calculators are available online to compute the spatial scaling factor and convert ^{3}He data into ^{3}He exposure ages: (i) the BGC calculator, formerly the initial CRONUS calculator (https://hess.ess.washington.edu/; Balco et al., 2008), (ii) the CRONUS calculator (http://cronus.cosmogenicnuclides.rocks/2.1/; Marrero et al., 2016), and (iii) the CREp calculator (https://crep.otelo.univ-lorraine.fr/#/; Martin et al., 2017).

Each calculator requires particular characteristics (spatial position, thickness, topographic shielding) as inputs to compute production rates specific to the collected samples. This scaling is performed using the most accurate available models, i.e., the Lal-Stone time-dependent model (Balco et al., 2008) and/or the LSD model (Lifton et al., 2014). Note that, in each calculator, the input cosmogenic ^{3}He concentration data must already be corrected for other ^{3}He sources.

The CRONUS calculator uses a unique and non-modifiable ^{3}He$_c$ production rate and VDM correction. In contrast, the CREp and BGC calculators allow users to choose from among several production rates: world average, regional mean, and local production rates. In CREp, these production rates can easily be selected from a clickable map. Moreover, CREp connects to the ICE-D calibration database daily, which is regularly updated to incorporate the newest literature data. The CREp and BGC calculators also offer the possibility of using different atmospheric models and geomagnetic databases.

5.4. Production of cosmogenic ^{3}He by muons

Numerical modeling based on experimental cross sections suggests that both fast muons and negative-muon capture reactions may produce cosmogenic ^{3}He (Lal 1987; Nesterenok and Yakubovich 2016). However, geological evidence supporting such reactions has been scarce, which has precluded the precise calibration of the muogenic production of ^{3}He (Kurz 1986a; Shuster et al., 2012). Larsen et al., (2021) recently presented a vertical profile of ^{3}He concentrations measured in pyroxenes and ilmenites along a 300-m-long drill core in the Columbia River basalts, which were emplaced by successive massive eruptions 16 Ma (Kasbohm and Schoene 2018). After correcting for non-cosmogenic ^{3}He components, this dataset displays a clear attenuation profile that precisely defines the muogenic production of ^{3}He: assuming a single exponential attenuation model (Braucher et al., 2011), the surficial SLHL muogenic ^{3}He production rate is 0.3 ± 0.1 at g^{-1} yr^{-1} and the attenuation length is 8,780 g cm^{-2} (Fig. 16; Larsen et al., 2021). Hence, in a massif having an average density of 2.7 g cm^{-3}, the muogenic production rate decreases by an exponential factor each 30 m.

1369   At Earth's surface, the contribution of this muogenic component represents only 3‰ of

1370   the spallogenic ^{3}He production (Martin et al., 2017), implying that muons can be safely

1371   neglected when determining cosmogenic ^{3}He exposure ages. However, with these production

1372   parameters, muogenic ^{3}He becomes dominant at depths >5 m and may represent 10^5–10^6 at g^{-1}

1373   in the case of exposures longer than 1 Myr. Shielded samples are useful for determining the

1374   non-cosmogenic ^{3}He correction for surficial samples (e.g., Amidon and Farley, 2011), for

1375   analyzing the pristine ^{3}He/^{4}He magmatic component (Dodson et al., 1997), for ensuring the

1376   preservation of paleo-exposure signals, and for computing accurate burial ages (Blard et al.,

1377   2006). Given the muogenic ^{3}He production parameters obtained by Larsen et al. (2021), several

1378   tens of meters of shielding are required to ensure the absence of cosmogenic ^{3}He for these

1379   applications.

1380
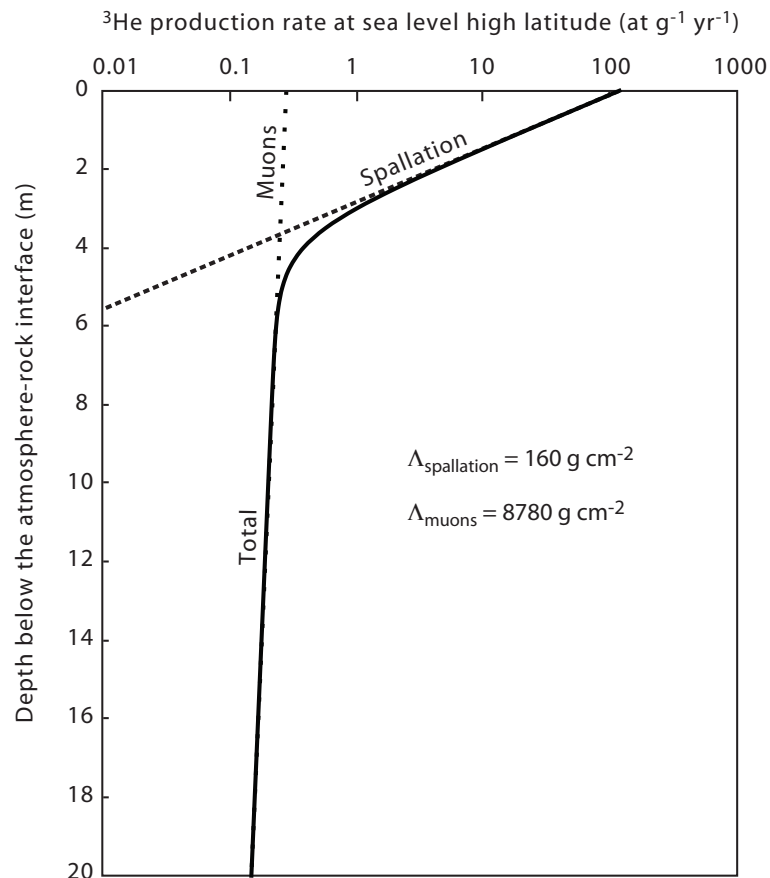
1381

1382

1383   **Figure 16. Vertical attenuation of spallogenic and muogenic ^{3}He production rates below the**
1384   **atmosphere-rock interface at SLHL. This model assumes surficial spallogenic and muogenic ^{3}He**
1385   **production rates of 124 at g^{-1} yr^{-1} (Martin et al., 2017) and 0.3 at g^{-1} yr^{-1} (Larsen et al., 2021),**
1386   **respectively, with respective attenuation lengths of 160 g cm^{-2} (Gosse and Phillips 2001) and**
1387   **8,780 g cm^{-2} (Larsen et al., 2021). In this calculation, rock density is assumed to be 2.7 g cm^{-3}.**

1388

1389   These muogenic production parameters affect the calculation of denudation rates from

1390   cosmogenic ^{3}He measurements in basin-wide eroded sediments (e.g., Ferrier et al., 2013;

1391   Puchol et al., 2017). Because ^{3}He is not radioactive, all muogenic ^{3}He nuclides produced at

1392   depth will be preserved until they reach the rock surface. Therefore, muon parameters must be

1393   included in the equation used to compute the denudation rate (ε) from cosmogenic ^{3}He

1394   concentrations:

1395

1396 $$\varepsilon \quad = \frac{\Lambda_n \bar{P}_n + \Lambda_\mu \bar{P}_\mu}{\rho \; ^{3}He_c}, \qquad\qquad (26)$$

1397

1398   where $\bar{P}_n$ and $\bar{P}_\mu$ are the basin-averaged spallogenic and muogenic production rates (at g^{-1} yr^{-1}),

1399   respectively, Λ_n and Λ_μ are their respective attenuation lengths (g cm^{-2}; Charreau et al., 2019),

1400   and ρ is density of the rock (g cm^{-3}).

1401   Previous articles by Ferrier et al. (2013), Litty et al. (2021), and Puchol et al. (2017)

1402   calculated denudation rates considering only the spallation parameters. Ideally, these published

1403   denudation rates should thus be recomputed with Equation (26), employing the new, well-

1404   defined muogenic parameters of Larsen et al. (2021). This revision would increase denudation

1405   rates by 5% for basins at an average elevation of 2,000 m, whereas denudation rates at sea level,

1406   where the contribution of muogenic production is the largest, would increase by 13%. In the

1407   case of ^{10}Be in quartz, incorporating muogenic production may increase calculated denudation

1408   rates by 20% at sea level (Lupker et al., 2012).

1409   Even if equation (26) is a reasonable approximation for computing denudation rates, the

1410   model of Heisinger et al. (2002a, b) most accurately describes muogenic production at a given

1411   depth (Balco, 2017). However, more work is needed to implement the muogenic ^{3}He calibration

1412   data of Larsen et al. (2021) into the model of Heisinger et al. (2002a, b).
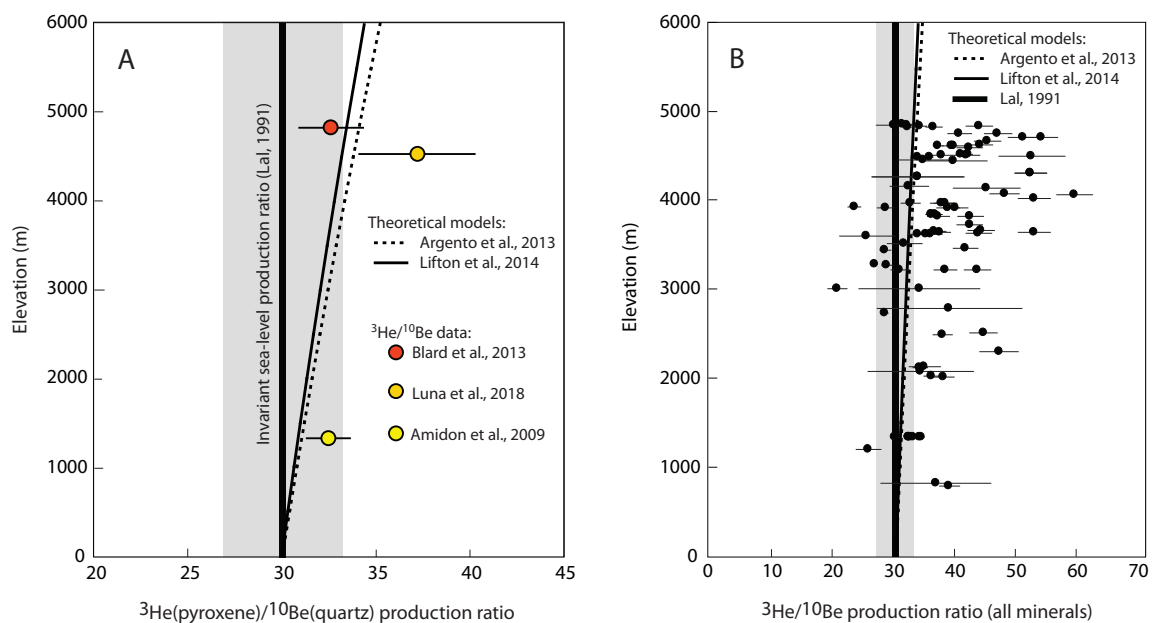
1413

1414   **5.5. Cross-calibration of ^{3}He against ^{10}Be and other cosmogenic nuclides**

1415   The most commonly used empirical scaling models that were published in the 1990's

1416   and 2000's (Dunai and Wijbrans 2000; Lal, 1991; Stone 2000) consider the impact of elevation

1417   to be similar for all cosmogenic nuclides, including ^{3}He and ^{10}Be. However, ab-initio physical

1418   models have recently revisited the use of different spatial scaling factors for each nuclide

1419   (Argento et al., 2013; Lifton et al., 2014), after D. Lal initially proposed the idea in his PhD

1420   thesis (Lal, 1958). These models predict that the ^{3}He/^{10}Be production ratio increases with

1421 increasing elevation, with the computed production of ^{3}He exceeding that of ^{10}Be by 4% at
1422 3,000 m elevation and up to 7% at 5,000 m (Fig. 17). Empirical benchmarks are necessary to
1423 test the validity of these theoretical models and better constrain the spatial variations of each
1424 nuclide's production rate. This can be done by measuring the ^{3}He/^{10}Be production ratios in
1425 minerals that have recently been exposed at the surface: if the possibility of an inherited
1426 cosmogenic ^{3}He component produced during an earlier exposure episode can be discarded, such
1427 cross-calibrations are key because they integrate the same exposure history for both nuclides.
1428 Only a handful of studies have produced such cross-calibration data: three articles reported
1429 cosmogenic ^{3}He concentrations in pyroxenes and ^{10}Be concentrations in coexisting quartz
1430 (Amidon et al., 2009; Blard et al., 2013; Luna et al., 2018), three others documented ^{3}He in
1431 accessory minerals (apatites, zircons, kyanites, garnets, iron oxides) and ^{10}Be in
1432 coexisting quartz (Amidon et al., 2008; Gayer et al., 2004; Kober et al., 2007), and another few
1433 articles reported cosmogenic ^{3}He concentrations in olivines/pyroxenes and ^{10}Be in coexisting
1434 feldspars (Blard et al., 2013; Zerathe et al., 2017) or olivines/pyroxenes (Blard et al., 2008;
1435 Nishiizumi et al., 1990). For this review, I updated and homogenized these ^{3}He/^{10}Be cross-
1436 calibration datasets by recalculating the ^{3}He/^{10}Be production ratios ($R_{3/10}$) using Equation (3) in
1437 Blard et al., (2013), to account for the radioactive decay of ^{10}Be. All ^{3}He concentrations in this
1438 dataset were only corrected for magmatic and nucleogenic ^{3}He. They thus include all
1439 cosmogenic production pathways: spallation, thermal neutron capture, and muogenic
1440 production. Note that these $R_{3/10}$ values are raw ^{3}He/^{10}Be production ratios that were not scaled
1441 for elevation. These updated data are available in Table S3 (https://doi.org/10.24396/ORDAR-
1442 91) and plotted in Figures 17–19. In the following, I use this updated dataset to test correlations
1443 and review potential causes of the spatial and rock-specific variabilities of the ^{3}He/^{10}Be
1444 production ratio.
1445   The cross-calibration studies based on cosmogenic ^{3}He in pyroxenes and ^{10}Be in
1446 coexisting quartz (Amidon et al., 2009; Blard et al., 2013; Luna et al., 2018) provide important
1447 observations (Fig. 17A). These two nuclide-mineral pairs are among the most commonly used,
1448 and their absolute production rates are the best documented (http://calibration.ice-d.org). Using
1449 this dataset, the CREp calculator (Martin et al., 2017), and the Lal-Stone time-dependent scaling
1450 (Balco et al., 2008) provides a theoretical SLHL $R_{3/10}$ value of 30.1 ± 3.1 (1σ) (Fig. 17). Then,
1451 comparing ^{3}He in pyroxene-^{10}Be in quartz cross-calibrations measured at 1,333, 4,530, and
1452 4,827 m elevation indicates a slight impact of elevation on the measured $R_{3/10}$ value (Fig. 17A).
1453 These data are in agreement, within 1σ uncertainties, with the theoretical models of Argento et
1454 al. (2013) and Lifton et al. (2014) that predict a 7–8% increase of $R_{3/10}$ at 5,000 m compared to

58

the sea-level value. Although this observation supports the use of nuclide-specific scaling, further new cross-calibration and absolute calibration datasets at variable elevations and latitudes will be useful for confirming and refining this relationship. I stress that the use of classical, non-nuclide-specific scaling factors, such as the Lal-Stone (Balco et al., 2008) or LSD scaling (Lifton et al., 2014), do not yield inaccuracies if using locally calibrated production rates, i.e., from calibration sites at similar elevations as the dated objects (Blard et al., 2013; Kelly et al., 2015; Martin et al., 2015).

Figure 17. Comparison of modeled (Argento et al., 2013; Lifton et al., 2014; Lal, 1991) and observed ³He/¹⁰Be production ratios *vs* elevation. Cross-calibrations are from (A) ³He in pyroxenes and ¹⁰Be in quartz (Amidon et al., 2009; Blard et al., 2013; Luna et al., 2018) and (B) ³He/¹⁰Be in any mineral pair (Amidon et al., 2008, 2009; Blard et al., 2008, 2013; Gayer et al., 2004; Kober et al., 2007; Luna et al., 2018; Nishiizumi et al., 1990; Zerathe et al., 2017). The vertical line shows the ³He/¹⁰Be production ratio at SLHL calculated using ³He in pyroxene-¹⁰Be in quartz data (http://calibration.ice-d.org), the CREp calculator (https://crep.otelo.univ-lorraine.fr/#/; Martin et al., 2017), and the Lal-Stone time-dependent scaling (Balco et al., 2008); the gray shaded bar indicates 1σ uncertainty.

However, considering the global ³He/¹⁰Be cross-calibration dataset, reported $R_{3/10}$ values deviate markedly from SLHL production ratio, and even from the theoretical production models of Argento et al. (2013) and Lifton et al. (2014). These high $R_{3/10}$ values reach ~50 above 4,000 m, and are from cross-calibration data based on ³He concentrations measured in accessory minerals (garnet, apatite, zircon; Amidon et al., 2008; Gayer et al., 2004). By determining the ³He in garnet/¹⁰Be in quartz production ratio from Himalayan glacial rocks at 3,000–4,500 m

1481   elevation, Gayer et al. (2004) identified an overproduction of cosmogenic ^{3}He compared to the

1482   standard scaling model that assumes an elevation-independent ^{3}He/^{10}Be production ratio (Fig.

1483   17; Lal, 1991). Dunai et al. (2007) attributed this high-elevation ^{3}He production excess to the

1484   unrecognized impact of cosmogenic thermal neutrons through the ^{6}Li(n,α)^{3}H reaction.

1485   According to Dunai et al. (2007), this reaction could account for a 50% increase of cosmogenic

1486 ^{3}He production in the Li-rich garnets (20–100 ppm Li) analyzed by Gayer et al. (2004).

1487   However, Amidon et al. (2008) later reported ^{3}He and ^{10}Be cross-calibration data on Li-poor

1488   (<10 ppm) minerals (zircons, kyanites) from the high Himalayas, which yielded ^{3}He/^{10}Be

1489   production ratios in the same range as those determined in garnet by Gayer et al. (2004) (Fig.

1490   17). This empirical evidence indicates that Li is not the main driver of this "anomalously" high

1491   cosmogenic ^{3}He production rate. Furthermore, when ^{3}He/^{10}Be cross-calibration data across all

1492   mineral pairs ($n = 88$) are plotted against Li concentration (Fig. 18), no correlation is observed

1493   ($R^2 = 0.19$, $n = 78$). Hence, other mechanisms are required to explain the high $R_{3/10}$ values above

1494   3,000 m. Interestingly, the highest anomalous ^{3}He production rates are reported for

1495   metamorphic or plutonic lithologies (Gayer et al., 2004; Amidon et al., 2008), whereas

1496   materials from recent (<10 Ma) volcanic terrains yield much lower ^{3}He/^{10}Be production ratios

1497   (Amidon et al., 2009; Blard et al., 2013; Luna et al., 2018).

1498
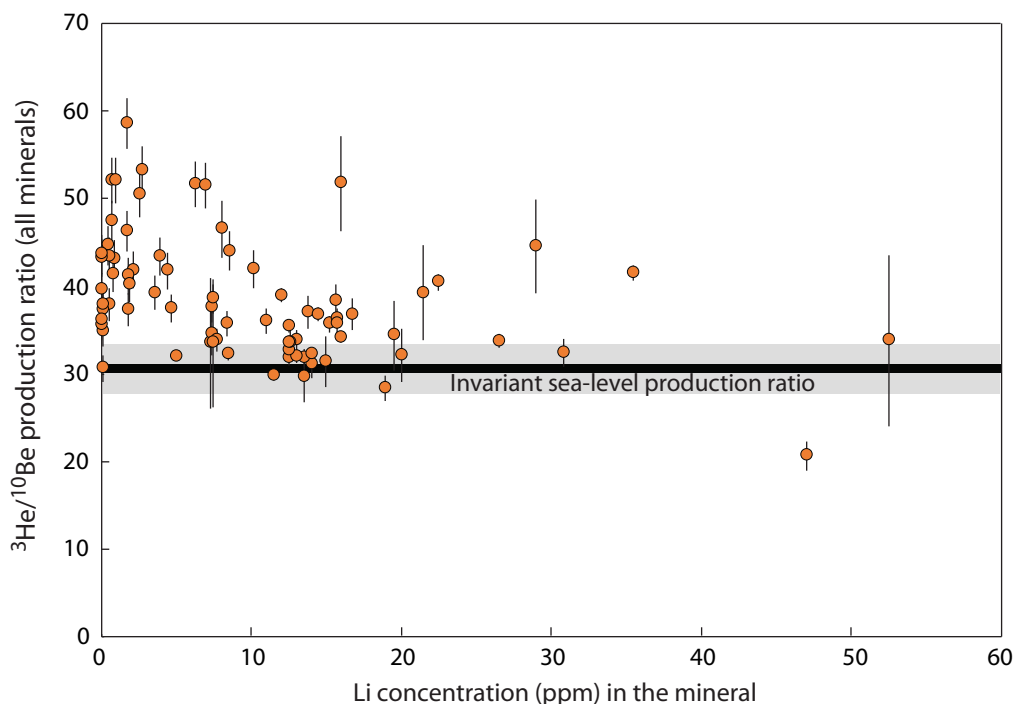
1499

1500   **Figure 18. ^{3}He/^{10}Be production ratio plotted against Li concentration (ppm) in the cosmogenic**
1501   **^{3}He-hosting mineral (data sources: Amidon et al., 2008, 2009; Blard et al., 2008, 2013; Gayer et**
1502   **al., 2004; Kober et al., 2007; Luna et al., 2018; Nishiizumi et al., 1990; Zerathe et al., 2017).**

1503

1504   Although further evidence is required to reach definitive conclusions, several

1505 mechanisms might explain these observations:

1506

1507   i)   **Inheritance of previous exposure.** Because ^{3}He is a stable nuclide, it is more

1508   prone than radioactive nuclides to be affected by inheritance from previous

1509   exposure episodes that might have occurred several million years ago. Hence,

1510   after the radioactive decay of ^{10}Be during subsequent burial episodes, such

1511   inherited ^{3}He concentrations will appear to be in excess compared to the actual

1512 $R_{3/10}$ value. This mechanism was proposed by Zerathe et al. (2017) to identify

1513   two outliers among a dataset of eight samples from a ^{3}He/^{10}Be cross-calibration

1514   based on andesitic boulders. Another observation supporting this explanation is

1515   the relationship between observed $R_{3/10}$ values and ^{10}Be-derived exposure ages

1516   for the whole dataset (Fig. 19). I used ^{10}Be to compute these exposure ages

1517   because this radioactive nuclide is less susceptible than ^{3}He to be biased by

1518   inheritance and because its production rate is better constrained. Interestingly,

1519   the scatter among observed $R_{3/10}$ values is much greater for younger exposure

1520   ages (<50 ka), and the maximum values of $R_{3/10}$ (>50) are only observed in that

1521   population. Moreover, exposure ages older than 100 ka (n = 10 of 88)

1522   systematically yield $R_{3/10}$ < 40. If true, the interpretation of ^{3}He inheritance

1523   implies that the anomalously large ^{3}He/^{10}Be production ratios are not real, but a

1524   geomorphological artifact. However, the Himalayan samples (Gayer et al., 2004;

1525   Amidon et al., 2008) are from a region characterized by rapid exhumation (1–10

1526   km/Myr; Amidon et al., 2008), a context that, in theory, favors the rapid turnover

1527   and rejuvenation of the subsurface, which should preclude significant

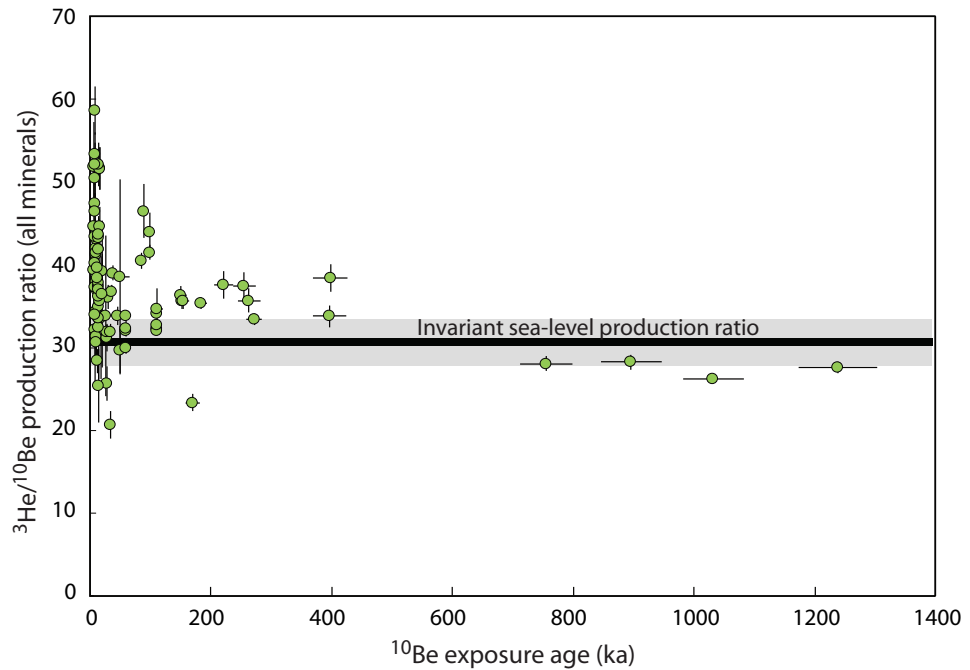1528   inheritance.

1529

1530

Figure 19. ^{3}He/^{10}Be production ratios plotted against ^{10}Be exposure ages (data sources: Amidon et al., 2008, 2009; Blard et al., 2008, 2013; Gayer et al., 2004; Kober et al., 2007; Luna et al., 2018; Nishiizumi et al., 1990; Zerathe et al., 2017).

1531
1532
1533

1534

1535

1536   ii)   **Chemical compositions of rocks and minerals.** Larsen et al., (2019) recently

1537   underscored that the composition of the whole rock may play a major role in the

1538 ^{3}He production rate, and that this bulk chemistry could be more important that

1539   the mineral composition itself because of the long-distance (20–100 μm)

1540   ejection of cosmogenic ^{3}He and ^{3}H (Fig. 4; Nesterenok and Yakubovich, 2016).

1541   The impact of this ^{3}He redistribution is larger for smaller grains (Larsen et al.,

1542   2019). This explanation may be compatible with the fact that the greatest

1543   observed ^{3}He overproduction (i.e., $R_{3/10} > 40$) at high elevation has so far only

1544   been documented in silicic lithologies (Amidon et al., 2008; Gayer et al., 2004),

1545   and not in intermediate rocks such as dacite or andesite (Blard et al., 2013; Luna

1546   et al., 2018). Although potential production pathways may be implicated in this

1547   bulk compositional effect (e.g., Lal, 1987), the exact reaction(s) and element(s)

1548   that may have induced this unrecognized ^{3}He production remain elusive and

1549   should be explored with additional data.

1550   iii)   **Impact of water on thermal neutron capture.** Liquid water, ice, or snow

1551   enhance thermal neutron capture and may modify the balance between spallation

1552   and thermal neutron production in the first few meters below the air-rock

1553	interface. This may affect the ^{3}He/^{10}Be production ratio because ^{10}Be is not
1554	produced by thermal neutron capture (Delunel et al., 2014; Dunai et al., 2014).
1555	Indeed, the largest anomalous ^{3}He/^{10}Be production ratios above 3,000 m have
1556	only been documented in wet regions of the Himalayas (Amidon et al., 2008;
1557	Gayer et al., 2004), and not in the dry Andes (Blard et al., 2013; Luna et al.,
1558	2018; Zerathe et al., 2017). However, the global dataset clearly indicates that
1559	$R_{3/10}$ is not correlated with Li content, which contradicts the potential
1560	involvement of a ^{6}Li(n,α)^{3}H reaction. If future data confirm the role of water or
1561	snow cover in inducing high ^{3}He/^{10}Be production ratios, the existence of an
1562	unknown production pathway involving thermal neutrons and an element other
1563	than Li should be explored. ^{2}H(n)^{3}H and ^{10}B(n,^{8}Be)^{3}H reactions are potential
1564	candidates (Lal, 1987). They could be tested with ad hoc experimental data.
1565	

1566 New ^{3}He/^{10}Be cross-calibration data and measuring cosmogenic ^{3}He in different

1567 minerals (with variable compositions and grain sizes) from different lithologies (andesite,

1568 dacite, granite-like composition) exposed at variable elevations and in different climatic

1569 contexts with variable snow cover will be useful in addressing these issues.

1570 Cross-calibrations of ^{3}He$_c$ against cosmogenic nuclides other than ^{10}Be may also

1571 provide information about nuclide-specific altitudinal scalings, although such observations are

1572 rare: few studies have provided intercomparison data with cosmogenic ^{21}Ne, ^{26}Al, and ^{36}Cl

1573 measured in the same samples as ^{3}He (Licciardi et al., 2008; Luna et al., 2018;

1574 Schimmelpfennig et al., 2011). The ^{36}Cl production rate is extremely sensitive to mineral

1575 composition, notably the K, Ca, and Cl contents of the target minerals (Schimmelpfennig et al.,

1576 2009). The ^{3}He/^{36}Cl production ratios reported by Licciardi et al. (2008), Luna et al. (2018),

1577 and Schimmelpfennig et al. (2011) were obtained by measuring ^{36}Cl concentrations in enstatites

1578 and feldspars or whole rocks with variable chemical compositions, notably their Cl contents.

1579 As these studies are based on different localities at variable latitudes and altitudes, there are too

1580 many unknowns to draw definitive conclusions about ^{3}He/^{36}Cl production ratios from these

1581 datasets.

1582 That said, Schimmelpfennig et al. (2011) documented the ^{3}He/^{36}Cl production ratios by

1583 measuring ^{3}He, ^{36}Cl, and ^{21}Ne in low-Ca pyroxenes (15% Ca) of homogenous composition

1584 sampled along a vertical transect between 1,000 and 4,300 m elevation at Kilimanjaro volcano

1585 (3°S, Tanzania). This dataset suggests that the ^{3}He/^{21}Ne and ^{3}He/^{36}Cl production ratios in low-

1586 Ca pyroxenes (average values of 5.4 ± 0.2 and 17.2 ± 1.8, respectively) are not elevation-

dependent. Luna et al. (2018) also measured ^{3}He/^{21}Ne in low-Ca pyroxenes (En$_{88-94}$) from moraines of the Altiplano-Puna plateau (24°S, Argentina) at 4,500 m elevation; they reported a ^{3}He/^{21}Ne production ratio of 4.06 ± 0.12. By measuring the ^{3}He/^{21}Ne production ratio in olivines and pyroxenes from <200 ka lava flows in Arizona situated at 1,500–2,000 m elevation, Fenton and Niedermann (2014) evidenced that mineral composition has a significant impact on the absolute cosmogenic ^{21}Ne production rate. Hence, the contrast between the ^{3}He/^{21}Ne production ratios determined by Luna et al. (2018) and Schimmelpfennig et al. (2011) above 4,000 m probably results from distinct absolute ^{21}Ne production rates due to different pyroxene compositions.

Although many uncertainties remain on the element-specific production pathways of other nuclides, these cross-calibrations against ^{21}Ne and ^{36}Cl support the hypothesis that ^{3}He in olivines and pyroxenes is probably not characterized by an unrecognized overproduction at high elevation (>2,000 m) (Blard et al., 2013a, b), in contrast to accessory minerals such as garnet (Gayer et al., 2004), kyanite, or zircon (Amidon et al., 2008). New cross-calibrations varying mineralogy, elevation, latitude, and snow cover will be useful for confirming this conclusion.

5.6. New directions of cosmogenic ^{3}He coupled with cosmogenic radioactive nuclides (^{14}C, ^{10}Be, ^{36}Cl, and ^{53}Mn)

Beyond cross-calibration issues, measuring two (or more) cosmogenic nuclides with different half lives in the same mineral also has great potential for many geoscience applications, including i) burial dating (Lebatard et al., 2014), ii) measuring paleo-depths of exposure (Hidy et al., 2018) or the thickness of snow cover (Hippe et al., 2014), iii) determining paleo-elevations (Blard et al., 2019a, b), or iv) detecting complex exposure histories such as the dynamics of sediment transfer (Wittmann and von Blanckenburg, 2009). The most commonly used nuclide pair for these applications is ^{26}Al/^{10}Be in quartz (Granger, 2006), although ^{10}Be/^{21}Ne in quartz has the potential to probe longer timescales (5–20 Ma, compared to 0.5–6 Ma for ^{26}Al/^{10}Be) (Balco and Shuster, 2009; Sartégou et al., 2020).

Despite their intriguing potential, these nuclide pairs remain to be tested in quartz-free environments, such as andesitic or mafic terrains. Although measuring ^{3}He is often possible in such geological settings, measuring radioactive cosmogenic nuclides in the same rock sample remains challenging; only a few studies have reported joint measurements of ^{3}He and a radioactive cosmogenic nuclide in the same mineral (Blard et al., 2008; Licciardi et al., 2008; Nishiizumi et al., 1990).

1620   Because the measurement of ^{36}Cl in Ca- and K-rich minerals (feldspars, pyroxene) is

1621   quite well established (Schimmelpfennig et al., 2009), the ^{3}He-^{36}Cl pair is, for now, the most

1622   accessible nuclide pair for multi-isotopic analyses in mafic terrains (Licciardi et al., 2008).

1623   However, given the half-life of ^{36}Cl ($t_{1/2}$ = 301 kyr), this pair can only be used to probe the last

1624   few million years in the best cases. Measuring ^{10}Be in olivine and pyroxene might prove useful

1625   in extending this temporal range, although removing atmospheric ^{10}Be contamination from

1626   mafic minerals has long been considered an unsolvable problem (Ivy-Ochs et al., 1998). A new

1627   chemical procedure employing a preliminary crushing step has allowed the accurate

1628   measurement of ^{10}Be in olivine and pyroxene (Blard et al., 2008; Eaves et al., 2018). Using

1629   these data and the Lal-Stone time-dependent model, Eaves et al., (2018) determined the SLHL

1630 ^{10}Be production rate to be 3.2 ± 0.8 at g^{-1} yr^{-1} in olivine and pyroxene, extending the utility of

1631 ^{10}Be burial age or paleoaltimetry measurements in intermediate and mafic rocks to 5 Ma. Recent

1632   developments in accelerator mass spectrometry offer the possibility to measure ^{53}Mn in Fe-rich

1633   minerals, such as iron-oxides (Schiffer et al., 2020). With a half-life of 3.74 Myr, ^{53}Mn is an

1634   interesting complement to ^{3}He; this nuclide pair could extend the range of burial dating to 25

1635   Ma. The ability to measure short-lived in-situ cosmogenic ^{14}C ($t_{1/2}$ = 5,730 yr; Pigati et al.,

1636   2010) in the same mineral as ^{3}He is also an interesting development because this pair could be

1637   used to determine paleo-depths of exposure, snow cover thicknesses, landslide volumes, and

1638   burial ages from 1 to 40 ka.

1639   All such applications involving exposures below the rock-atmosphere interface, i.e.,

1640   burial episodes, should carefully integrate the impact of the muogenic contribution using the

1641   most recently determined parameters, currently those of Larsen et al. (2021) for ^{3}He$_{c}$. See

1642   reviews by Balco (2017), Braucher et al. (2011), and Lupker et al. (2015) for the muogenic

1643   production of other cosmogenic nuclides.

1644

1645

1646   **6. Concluding remarks**

1647

1648   In this review article, I have summarized and different strategies that can be applied to

1649   accurately and precisely measure cosmogenic ^{3}He concentrations. Even using the most accurate

1650   and precise mass spectrometer, non-cosmogenic ^{3}He components have a major impact on the

1651   detection limit and the precision of the method; correcting for other sources of ^{3}He in the

1652   mineral of interest thus requires particular attention. The choice of the best correction strategy

1653   is determined by the respective concentrations of radiogenic and magmatic ^{4}He:

1654

Case 1: Magmatic and radiogenic ^{4}He concentrations are of the same order of magnitude.
Measure U, Th, and Li and independently determine the He closure age to compute ^{4}He*.

       Strategy 1a – Crush and fuse minerals, use Equation (15).

       Strategy 1b – Fuse multiple aliquots and build isochrons (see section 3.5.3).

Case 2: Uneroded lavas (a particularity of Case 1). In this case, it is not necessary to calculate the He closure age. However, U, Th, and Li measurements remain necessary to correct for radiogenic He by calculating the R-factor.

       Strategy 2a – Crush and fuse minerals, use Equations (17-18).

       Strategy 2b – Fuse multiple aliquots and build isochrons (see section 3.5.3).

Case 3: ^{4}He* >> ^{4}He$_{mag}$. This is the case for samples with very long closure ages (>>1 Myr) and/or U-Th-rich minerals (>> 1 ppm). In this situation, the correction for magmatic ^{3}He is not easy and may hinder the precision on cosmogenic ^{3}He, particularly for short exposure ages (<10 ka). Prolonged crushing or the fusion of cosmogenically shielded samples from the same lithology are ways to estimate the magmatic ^{3}He component.

       Future improvements will be to: i) improve our knowledge of the spatial and temporal variability of production rates; ii) develop cosmogenic ^{3}He measurements in new minerals, such as accessory minerals in Si-rich rocks; iii) better document the impacts of the chemical compositions of minerals and their host rocks on production rates; and iv) better understand exotic ^{3}He production pathways, notably those involving muons and thermal neutrons. To achieve these objectives, important information will be acquired from new calibrations of ^{3}He$_c$ production rates measured in non-eroded and well-dated surfaces, as well as from cross-calibrations with other cosmogenic nuclides such as ^{10}Be. These future directions have the potential to improve the accuracy and precision of the ^{3}He geoscientific toolbox and open the door to new applications (burial dating, paleoaltimetry, paleo-depths, durations of volcanic eruptions) and lithologies.

66

References

Aciego, Sarah M., Donald J. DePaolo, B.M. Kennedy, Michael P. Lamb, Kenneth W.W. Sims, and William E. Dietrich. 2007. "Combining [3He] Cosmogenic Dating with U–Th/He Eruption Ages Using Olivine in Basalt." *Earth and Planetary Science Letters* 254 (3–4): 288–302. https://doi.org/10.1016/j.epsl.2006.11.039.

Ackert, Robert P., Brad S. Singer, Hervé Guillou, Mike R. Kaplan, and Mark D. Kurz. 2003. "Long-Term Cosmogenic 3He Production Rates from 40Ar/39Ar and K–Ar Dated Patagonian Lava Flows at 47°S." *Earth and Planetary Science Letters* 210 (1–2): 119–36. https://doi.org/10.1016/S0012-821X(03)00134-1.

Aldrich, LT, and AOC Nier. 1946. "The Abundance of He3 in Atmospheric and Well Helium." *Physical Review* 70 (11–12): 983.

Aleinikoff, John N., Donald L. Winegarden, and Marianne Walter. 1990. "U-Pb Ages of Zircon Rims: A New Analytical Method Using the Air-Abrasion Technique." *Chemical Geology: Isotope Geoscience Section* 80 (4): 351–63. https://doi.org/10.1016/0168-9622(90)90015-5.

Amidon, W H, and K A Farley. 2011. "Cosmogenic 3He Production Rates in Apatite, Zircon and Pyroxene Inferred from Bonneville Flood Erosional Surfaces." *Quaternary Geochronology* 6: 10–21.

Amidon, W H, K A Farley, D W Burbank, and B Pratt-Sitaula. 2008. "Anomalous Cosmogenic 3He Production and Elevation Scaling in the High Himalaya." *Earth and Planetary Science Letters* 265 (1–2): 287–301.

Amidon, W H, D H Rood, and K A Farley. 2009. "Cosmogenic 3He and 21Ne Production Rates Calibrated against 10Be in Minerals from the Coso Volcanic Field." *Earth and Planetary Science Letters* 280 (1–4): 194–204.

Amidon, William H., Daniel Hobbs, and Scott A. Hynek. 2015. "Retention of Cosmogenic 3He in Calcite." *Quaternary Geochronology* 27 (April): 172–84. https://doi.org/10.1016/j.quageo.2015.03.004.

Andrews, J. N., and R. L. F. Kay. 1982. "Natural Production of Tritium in Permeable Rocks." *Nature* 298 (5872): 361–63. https://doi.org/10.1038/298361a0.

Andrews, J.N. 1985. "The Isotopic Composition of Radiogenic Helium and Its Use to Study Groundwater Movement in Confined Aquifers." *Chemical Geology* 49 (1–3): 339–51. https://doi.org/10.1016/0009-2541(85)90166-4.

Argento, David C., Robert C. Reedy, and John O. Stone. 2013. "Modeling the Earth's Cosmic Radiation." *Nuclear Instruments and Methods in Physics Research Section B: Beam Interactions with Materials and Atoms* 294 (January): 464–69. https://doi.org/10.1016/j.nimb.2012.05.022.

Balco, Greg. 2017. "Production Rate Calculations for Cosmic-Ray-Muon-Produced 10Be and 26Al Benchmarked against Geological Calibration Data." *Quaternary Geochronology* 39 (April): 150–73. https://doi.org/10.1016/j.quageo.2017.02.001.

Balco, Greg, and David L. Shuster. 2009. "26Al-10Be-21Ne Burial Dating." *Earth and Planetary Science Letters* 286 (3–4): 570–75. https://doi.org/10.1016/j.epsl.2009.07.025.

Balco, Greg, John O. Stone, Nathaniel A. Lifton, and Tibor J. Dunai. 2008. "A Complete and Easily Accessible Means of Calculating Surface Exposure Ages or Erosion Rates from 10Be and 26Al Measurements." *Quaternary Geochronology* 3 (3): 174–95. https://doi.org/10.1016/j.quageo.2007.12.001.

Balter-Kennedy, Allie, Gordon Bromley, Greg Balco, Holly Thomas, and Margaret S. Jackson. 2020. "A 14.5-Million-Year Record of East Antarctic Ice Sheet Fluctuations from the Central Transantarctic Mountains, Constrained with Cosmogenic 3He, 10Be, 21Ne, and 26Al." *The Cryosphere* 14 (8): 2647–72. https://doi.org/10.5194/tc-14-2647-2020.

Baur, H. 1999. "A Noble Gas Mass Spectrometer Compressor Source with Two Orders of Magnitude Improvement in Sensitivity." *EOS, Trans. Am. Geophys. Union* 46: F1118.

Blackburn, Terrence J., Daniel F. Stockli, and J. Douglas Walker. 2007. "Magnetite (U–Th)/He Dating and Its Application to the Geochronology of Intermediate to Mafic Volcanic Rocks." *Earth and Planetary Science Letters* 259 (3–4): 360–71. https://doi.org/10.1016/j.epsl.2007.04.044.

Blard, P. H., J. Lavé, K. A. Farley, M. Fornari, N. Jiménez, and V. Ramirez. 2009. "Late Local Glacial Maximum in the Central Altiplano Triggered by Cold and Locally-Wet Conditions during the Paleolake Tauca Episode (17-15 Ka, Heinrich 1)." *Quaternary Science Reviews* 28 (27–28): 3414–27. https://doi.org/10.1016/j.quascirev.2009.09.025.

Blard, P.-H., G. Balco, P. G. Burnard, K. A. Farley, C. R. Fenton, R. Friedrich, A. J T Jull, et al., 2015. "An Inter-Laboratory Comparison of Cosmogenic 3He and Radiogenic 4He in the CRONUS-P Pyroxene Standard." *Quaternary Geochronology* 26: 11–19. https://doi.org/10.1016/j.quageo.2014.08.004.

Blard, P.-H., D. Bourlès, J. Lavé, and R. Pik. 2006. "Applications of Ancient Cosmic-Ray Exposures: Theory, Techniques and Limitations." *Quaternary Geochronology* 1 (1): 59–73. https://doi.org/10.1016/j.quageo.2006.06.003.

Blard, P-H, D Bourles, R Pik, and J Lave. 2008. "In Situ Cosmogenic 10Be in Olivines and Pyroxenes." *Quaternary Geochronology* 3 (3): 196–205. https://doi.org/10.1016/j.quageo.2007.11.006.

Blard, P.-H., R. Braucher, J. Lavé, and D. Bourlès. 2013. "Cosmogenic 10Be Production Rate Calibrated against 3He in the High Tropical Andes (3800-4900 m, 20-22° S)." *Earth and Planetary Science Letters* 382: 140–49. https://doi.org/10.1016/j.epsl.2013.09.010.

Blard, P-H, and K Farley. 2008. "The Influence of Radiogenic 4He on Cosmogenic 3He Determinations in Volcanic Olivine and Pyroxene." *Earth and Planetary Science Letters* 276 (1–2): 20–29. https://doi.org/10.1016/j.epsl.2008.09.003.

Blard, P.-H., J. Lave, R. Pik, X. Quidelleur, D.L. Bourles, and G. Kieffer. 2005. "Fossil Cosmogenic 3He Record from K–Ar Dated Basaltic Flows of Mount Etna Volcano (Sicily, 38°N): Evaluation of a New Paleoaltimeter." *Earth and Planetary Science Letters* 236 (3–4): 613–31. https://doi.org/10.1016/j.epsl.2005.05.028.

Blard, P.-H., J. Lavé, R. Pik, P. Wagnon, and D. Bourlès. 2007. "Persistence of Full Glacial Conditions in the Central Pacific until 15,000 Years Ago." *Nature* 449 (7162): 591–94. https://doi.org/10.1038/nature06142.

Blard, PH, J Lavé, F Sylvestre, CJ Placzek, C Claude, V Galy, T Condom, and B Tibari. 2013. "Cosmogenic 3He Production Rate in the High Tropical Andes (3800 m, 20 S): Implications for the Local Last Glacial Maximum." *Earth and Planetary Science Letters* 377: 260–75.

Blard, P.-H., M. Lupker, and M. Rousseau. 2019. "Paired-Cosmogenic Nuclide Paleoaltimetry." *Earth and Planetary Science Letters* 515 (June): 271–82. https://doi.org/10.1016/j.epsl.2019.03.005.

Blard, P.-H., Maarten Lupker, Moïse Rousseau, and Jim Tesson. 2019. "Two MATLAB Programs for Computing Paleo-Elevations and Burial Ages from Paired-Cosmogenic Nuclides." *MethodsX* 6: 1547–56. https://doi.org/10.1016/j.mex.2019.05.017.

Blard, P.-H., and R. Pik. 2008. "An Alternative Isochron Method for Measuring Cosmogenic 3He in Lava Flows." *Chemical Geology* 251 (1–4): 20–32. https://doi.org/10.1016/j.chemgeo.2008.02.004.

Blard, P.-H., R. Pik, J. Lave, D. Bourles, P.G. Burnard, R. Yokochi, B. Marty, and F. Trusdell. 2006. "Cosmogenic 3He Production Rates Revisited from Evidences of Grain Size Dependent Release of Matrix-Sited Helium." *Earth and Planetary Science Letters* 247 (3–4): 222–34. https://doi.org/10.1016/j.epsl.2006.05.012.

Blard, P.-H., N. Puchol, and K.A. Farley. 2008. "Constraints on the Loss of Matrix-Sited

1802 Helium during Vacuum Crushing of Mafic Phenocrysts." *Geochimica et Cosmochimica Acta*
1803 72 (15): 3788–3803. https://doi.org/10.1016/j.gca.2008.05.044.
1804 Borchers, Brian, Shasta Marrero, Greg Balco, Marc Caffee, Brent Goehring, Nathaniel Lifton,
1805 Kunihiko Nishiizumi, Fred Phillips, Joerg Schaefer, and John Stone. 2016. "Geological
1806 Calibration of Spallation Production Rates in the CRONUS-Earth Project." *Quaternary*
1807 *Geochronology* 31: 188–98. https://doi.org/10.1016/j.quageo.2015.01.009.
1808 Boucher, Christine, Tefang Lan, Jennifer Mabry, David V. Bekaert, Peter G. Burnard, and
1809 Bernard Marty. 2018. "Spatial Analysis of the Atmospheric Helium Isotopic Composition:
1810 Geochemical and Environmental Implications." *Geochimica et Cosmochimica Acta* 237
1811 (September): 120–30. https://doi.org/10.1016/j.gca.2018.06.010.
1812 Braucher, R., S. Merchel, J. Borgomano, and D. L. Bourlès. 2011. "Production of Cosmogenic
1813 Radionuclides at Great Depth: A Multi Element Approach." *Earth and Planetary Science*
1814 *Letters* 309 (1–2): 1–9. https://doi.org/10.1016/j.epsl.2011.06.036.
1815 Bromley, Gordon R.M., Brenda L. Hall, Joerg M. Schaefer, Gisela Winckler, Claire E. Todd,
1816 and Kurt M. Rademaker. 2011. "Glacier Fluctuations in the Southern Peruvian Andes during
1817 the Late-Glacial Period, Constrained with Cosmogenic3He." *Journal of Quaternary Science* 26
1818 (1): 37–43. https://doi.org/10.1002/jqs.1424.
1819 Bromley, Gordon R.M., Gisela Winckler, Joerg M. Schaefer, Michael R. Kaplan, Kathy J.
1820 Licht, and Brenda L. Hall. 2014. "Pyroxene Separation by HF Leaching and Its Impact on
1821 Helium Surface-Exposure Dating." *Quaternary Geochronology* 23 (October): 1–8.
1822 https://doi.org/10.1016/j.quageo.2014.04.003.
1823 Brook, Edward J., and Mark D. Kurz. 1993. "Surface-Exposure Chronology Using *in Situ*
1824 Cosmogenic [3] He in Antarctic Quartz Sandstone Boulders." *Quaternary Research* 39 (1): 1–
1825 10. https://doi.org/10.1006/qres.1993.1001.
1826 Burnard, P. G., and K. A. Farley. 2000. "Calibration of Pressure-Dependent Sensitivity and
1827 Discrimination in Nier-Type Noble Gas Ion Sources: TECHNICAL BRIEF." *Geochemistry,*
1828 *Geophysics, Geosystems* 1 (7): n/a-n/a. https://doi.org/10.1029/2000GC000038.
1829 Cerling, T. E. 1990. "Dating Geomorphologic Surfaces Using Cosmogenic 3He." *Quaternary*
1830 *Research* 33 (2): 148–56. https://doi.org/10.1016/0033-5894(90)90015-D.
1831 Cerling, T E, and H Craig. 1994. "Geomorphology and In-Situ Cosmogenic Isotopes." *Annual*
1832 *Review of Earth and Planetary Sciences* 22: 273–317.
1833 Cerling, Thure E., and Harmon Craig. 1994. "Cosmogenic 3He Production Rates from 39°N to
1834 46°N Latitude, Western USA and France." *Geochimica et Cosmochimica Acta* 58 (1): 249–55.
1835 https://doi.org/10.1016/0016-7037(94)90462-6.
1836 Charreau, Julien, Pierre-Henri Blard, Jéna Zumaque, Léo C.P. Martin, Tony Delobel, and Lucas
1837 Szafran. 2019. "Basinga: A Cell-by-cell GIS Toolbox for Computing Basin Average Scaling
1838 Factors, Cosmogenic Production Rates and Denudation Rates." *Earth Surface Processes and*
1839 *Landforms* 44 (12): 2349–65. https://doi.org/10.1002/esp.4649.
1840 Cherniak, D.J., W. Amidon, D. Hobbs, and E.B. Watson. 2015. "Diffusion of Helium in
1841 Carbonates: Effects of Mineral Structure and Composition." *Geochimica et Cosmochimica*
1842 *Acta* 165 (September): 449–65. https://doi.org/10.1016/j.gca.2015.06.033.
1843 Clarke, W.B., W.J. Jenkins, and Z. Top. 1976. "Determination of Tritium by Mass
1844 Spectrometric Measurement of 3He." *The International Journal of Applied Radiation and*
1845 *Isotopes* 27 (9): 515–22. https://doi.org/10.1016/0020-708X(76)90082-X.
1846 Craig, H., and R. J. Poreda. 1986. "Cosmogenic 3He in Terrestrial Rocks: The Summit Lavas
1847 of Maui." *Proceedings of the National Academy of Sciences* 83 (7): 1970–74.
1848 https://doi.org/10.1073/pnas.83.7.1970.
1849 De Laeter, John, and Mark D. Kurz. 2006. "Alfred Nier and the Sector Field Mass
1850 Spectrometer." *Journal of Mass Spectrometry* 41 (7): 847–54.
1851 https://doi.org/10.1002/jms.1057.

Delon, Rémi, Sylvie Demouchy, Yves Marrocchi, Mohamed Ali Bouhifd, Julien Gasc, Patrick Cordier, Sanae Koizumi, and Pete G. Burnard. 2020. "Effect of Deformation on Helium Storage and Diffusion in Polycrystalline Forsterite." *Geochimica et Cosmochimica Acta* 273 (March): 226–43. https://doi.org/10.1016/j.gca.2020.01.018.

Delunel, Romain, Pierre-Henri Blard, Léo C.P. Martin, Sébastien Nomade, and Fritz Schlunegger. 2016. "Long Term Low Latitude and High Elevation Cosmogenic 3He Production Rate Inferred from a 107ka-Old Lava Flow in Northern Chile; 22°S-3400ma.s.l." *Geochimica et Cosmochimica Acta* 184: 71–87. https://doi.org/10.1016/j.gca.2016.04.023.

Delunel, Romain, Didier L. Bourlès, Peter A. van der Beek, Fritz Schlunegger, Ingo Leya, Jozef Masarik, and Emmanuel Paquet. 2014. "Snow Shielding Factors for Cosmogenic Nuclide Dating Inferred from Long-Term Neutron Detector Monitoring." *Quaternary Geochronology* 24 (December): 16–26. https://doi.org/10.1016/j.quageo.2014.07.003.

Dodson, Allen, B. Mack Kennedy, and Donald J. DePaolo. 1997. "Helium and Neon Isotopes in the Imnaha Basalt, Columbia River Basalt Group: Evidence for a Yellowstone Plume Source." *Earth and Planetary Science Letters* 150 (3–4): 443–51. https://doi.org/10.1016/S0012-821X(97)00090-3.

Dunai, Tibor J. 2010. *Cosmogenic Nuclides: Principles, Concepts and Applications in the Earth Surface Sciences*. Cambridge: Cambridge University Press. https://doi.org/10.1017/CBO9780511804519.

Dunai, Tibor J., Finlay M. Stuart, Raphaël Pik, Pete Burnard, and Eric Gayer. 2007. "Production of 3He in Crustal Rocks by Cosmogenic Thermal Neutrons." *Earth and Planetary Science Letters* 258 (1–2): 228–36. https://doi.org/10.1016/j.epsl.2007.03.031.

Dunai, Tibor J., and Jan R. Wijbrans. 2000. "Long-Term Cosmogenic 3He Production Rates (152 Ka–1.35 Ma) from 40Ar/39Ar Dated Basalt Flows at 29°N Latitude." *Earth and Planetary Science Letters* 176 (1): 147–56. https://doi.org/10.1016/S0012-821X(99)00308-8.

Dunai, T.J. 2001. "Influence of Secular Variation of the Geomagnetic Field on Production Rates of in Situ Produced Cosmogenic Nuclides." *Earth and Planetary Science Letters* 193 (1–2): 197–212. https://doi.org/10.1016/S0012-821X(01)00503-9.

Dunai, T.J., S.A. Binnie, A.S. Hein, and S.M. Paling. 2014. "The Effects of a Hydrogen-Rich Ground Cover on Cosmogenic Thermal Neutrons: Implications for Exposure Dating." *Quaternary Geochronology* 22 (August): 183–91. https://doi.org/10.1016/j.quageo.2013.01.001.

Dunne, Jeff, David Elmore, and Paul Muzikar. 1999. "Scaling Factors for the Rates of Production of Cosmogenic Nuclides for Geometric Shielding and Attenuation at Depth on Sloped Surfaces." *Geomorphology* 27 (1–2): 3–11. https://doi.org/10.1016/S0169-555X(98)00086-5.

Eaves, Shaun R., Julia A. Collins, R. Selwyn Jones, Kevin P. Norton, Stephen G. Tims, and Andrew N. Mackintosh. 2018. "Further Constraint of the in Situ Cosmogenic 10Be Production Rate in Pyroxene and a Viability Test for Late Quaternary Exposure Dating." *Quaternary Geochronology* 48 (October): 121–32. https://doi.org/10.1016/j.quageo.2018.09.006.

Eaves, Shaun R., Andrew N. Mackintosh, Gisela Winckler, Joerg M. Schaefer, Brent V. Alloway, and Dougal B. Townsend. 2016. "A Cosmogenic He-3 Chronology of Late Quaternary Glacier Fluctuations in North Island, New Zealand (39 Degrees S)." *Quaternary Science Reviews* 132 (January): 40–56. https://doi.org/10.1016/j.quascirev.2015.11.004.

Eaves, Shaun R, Gisela Winckler, Joerg M Schaefer, Marcus J Vandergoes, Brent V Alloway, Andrew N Mackintosh, Dougal B Townsend, Matthew T Ryan, and Xun Li. 2015. "A Test of the Cosmogenic 3He Production Rate in the Southwest Pacific (39S)." *Journal of Quaternary Science* 30: 9.

Farley, K A, B P Kohn, and B Pillans. 2002. "The Effects of Secular Disequilibrium on (U-Th)/He Systematics and Dating of Quaternary Volcanic Zircon and Apatite." *Earth and*

Planetary Science Letters 201: 117–25.

Farley, K. a., and D. F. Stockli. 2002. "(U-Th)/He Dating of Phosphates: Apatite, Monazite, and Xenotime." *Reviews in Mineralogy and Geochemistry* 48 (1): 559–77. https://doi.org/10.2138/rmg.2002.48.15.

Farley, K.A. 2018. "Helium Diffusion Parameters of Hematite from a Single-Diffusion-Domain Crystal." *Geochimica et Cosmochimica Acta* 231 (June): 117–29. https://doi.org/10.1016/j.gca.2018.04.005.

Farley, K.a., J. Libarkin, S. Mukhopadhyay, and W. Amidon. 2006. "Cosmogenic and Nucleogenic 3He in Apatite, Titanite, and Zircon." *Earth and Planetary Science Letters* 248 (1–2): 451–61. https://doi.org/10.1016/j.epsl.2006.06.008.

Fenton, Cassandra R., Darren F. Mark, Dan N. Barfod, Samuel Niedermann, Mirjam M. Goethals, and Finlay M. Stuart. 2013. "40Ar/39Ar Dating of the SP and Bar Ten Lava Flows AZ, USA: Laying the Foundation for the SPICE Cosmogenic Nuclide Production-Rate Calibration Project." *Quaternary Geochronology* 18: 158–72. https://doi.org/10.1016/j.quageo.2013.01.007.

Fenton, Cassandra R., and Samuel Niedermann. 2014. "Surface Exposure Dating of Young Basalts (1-200ka) in the San Francisco Volcanic Field (Arizona, USA) Using Cosmogenic 3He and 21Ne." *Quaternary Geochronology* 19: 87–105. https://doi.org/10.1016/j.quageo.2012.10.003.

Fenton, Cassandra R., Samuel Niedermann, Mirjam M. Goethals, Björn Schneider, and Jan Wijbrans. 2009. "Evaluation of Cosmogenic 3He and 21Ne Production Rates in Olivine and Pyroxene from Two Pleistocene Basalt Flows, Western Grand Canyon, AZ, USA." *Quaternary Geochronology* 4 (6): 475–92. https://doi.org/10.1016/j.quageo.2009.08.002.

Fenton, Cassandra R, Robert H Webb, Philip A Pearthree, Thure E Cerling, and Robert J Poreda. 2001. "Displacement Rates on the Toroweap and Hurricane Faults: Implications for Quaternary Downcutting in the Grand Canyon, Arizona." *Geology* 29 (11): 1035–38.

Ferrier, K. L., J. T. Perron, S. Mukhopadhyay, M. Rosener, J. D. Stock, K. L. Huppert, and M. Slosberg. 2013. "Covariation of Climate and Long-Term Erosion Rates across a Steep Rainfall Gradient on the Hawaiian Island of Kaua'i." *Geological Society of America Bulletin* 125 (7–8): 1146–63. https://doi.org/10.1130/B30726.1.

Fisher, D. 1972. "Cosmogenic Rare Gas Production Rates in Chondritic Meteorites." *Earth and Planetary Science Letters* 16 (3): 391–95. https://doi.org/10.1016/0012-821X(72)90157-4.

Fleck, Robert J., and Andrew T. Calvert. 2014. "Modified Expression for Bulb-Tracer Depletion-Effect on Argon Dating Standards." *Geochemistry, Geophysics, Geosystems* 15 (4): 1657–62. https://doi.org/10.1002/2013GC005205.

Foeken, Jurgen P.T., Finlay M. Stuart, and Darren F. Mark. 2012. "Long-Term Low Latitude Cosmogenic 3He Production Rate Determined from a 126ka Basalt from Fogo, Cape Verdes." *Earth and Planetary Science Letters* 359–360: 14–25. https://doi.org/10.1016/j.epsl.2012.10.005.

Gayer, E., R. Pik, J. Lavé, C. France-Lanord, D. Bourlès, and B. Marty. 2004. "Cosmogenic 3He in Himalayan Garnets Indicating an Altitude Dependence of the 3He/10Be Production Ratio." *Earth and Planetary Science Letters* 229 (1–2): 91–104. https://doi.org/10.1016/j.epsl.2004.10.009.

Gayer, Eric, Sujoy Mukhopadhyay, and Brendan J. Meade. 2008. "Spatial Variability of Erosion Rates Inferred from the Frequency Distribution of Cosmogenic 3He in Olivines from Hawaiian River Sediments." *Earth and Planetary Science Letters* 266 (3–4): 303–15. https://doi.org/10.1016/j.epsl.2007.11.019.

Goehring, Brent M., Mark D. Kurz, Greg Balco, Joerg M. Schaefer, Joseph Licciardi, and Nathaniel Lifton. 2010. "A Reevaluation of in Situ Cosmogenic 3He Production Rates." *Quaternary Geochronology* 5 (4): 410–18. https://doi.org/10.1016/j.quageo.2010.03.001.

Goehring, Brent M., Paul Muzikar, and Nathaniel A. Lifton. 2018. "Establishing a Bayesian Approach to Determining Cosmogenic Nuclide Reference Production Rates Using He-3." *Earth and Planetary Science Letters* 481: 91–100. https://doi.org/10.1016/j.epsl.2017.10.025.

Gosse, John C., and Fred M. Phillips. 2001. "Terrestrial in Situ Cosmogenic Nuclides: Theory and Application." *Quaternary Science Reviews* 20 (14): 1475–1560. https://doi.org/10.1016/S0277-3791(00)00171-2.

Granger, D.E. 2006. "A Review of Burial Dating Methods with 26Al and 10Be." In *In Situ–Produced Cosmogenic Nuclides and Quantifi Cation of Geological Processes*, edited by L. Siame, D.L. Bourlès, and E.T. Brown, 1–16. Geological Society of America Special Paper 415.

Heineke, Caroline, Samuel Niedermann, Ralf Hetzel, and Cüneyt Akal. 2016. "Surface Exposure Dating of Holocene Basalt Flows and Cinder Cones in the Kula Volcanic Field (Western Turkey) Using Cosmogenic 3He and 10Be." *Quaternary Geochronology* 34 (August): 81–91. https://doi.org/10.1016/j.quageo.2016.04.004.

Heisinger, B., D. Lal, A.J.T. Jull, P. Kubik, S. Ivy-Ochs, K. Knie, and E. Nolte. 2002. "Production of Selected Cosmogenic Radionuclides by Muons: 2. Capture of Negative Muons." *Earth and Planetary Science Letters* 200: 357–69.

Heisinger, B., D. Lal, A.J.T. Jull, P. Kubik, S. Ivy-Ochs, S. Neumaier, K. Knie, V. Lazarev, and E. Nolte. 2002. "Production of Selected Cosmogenic Radionuclides by Muons; 1. Fast Muons." *Earth and Planetary Science Letters* 200: 345–55.

Hess, V.F. 1912. "Observations of Penetrating Radiation during Seven Free Balloon Flights." *Phys. Zeit.* 13: 1084–91.

Hidy, Alan J., John C. Gosse, Paul Sanborn, and Duane G. Froese. 2018. "Age-Erosion Constraints on an Early Pleistocene Paleosol in Yukon, Canada, with Profiles of 10Be and 26Al: Evidence for a Significant Loess Cover Effect on Cosmogenic Nuclide Production Rates." *CATENA* 165 (June): 260–71. https://doi.org/10.1016/j.catena.2018.02.009.

Hilton, D.R., K. Hammerschmidt, S. Teufel, and H. Friedrichsen. 1993. "Helium Isotope Characteristics of Andean Geothermal Fluids and Lavas." *Earth and Planetary Science Letters* 120 (3–4): 265–82. https://doi.org/10.1016/0012-821X(93)90244-4.

Hippe, K., S. Ivy-Ochs, F. Kober, J. Zasadni, R. Wieler, L. Wacker, P. W. Kubik, and C. Schlüchter. 2014. "Chronology of Lateglacial Ice Flow Reorganization and Deglaciation in the Gotthard Pass Area, Central Swiss Alps, Based on Cosmogenic10Be and in Situ14C." *Quaternary Geochronology* 19: 14–26. https://doi.org/10.1016/j.quageo.2013.03.003.

Hoffman, John H., and Alfred O. Nier. 1993. "Atmospheric Helium Isotopic Ratio." *Geophysical Research Letters* 20 (2): 121–23. https://doi.org/10.1029/93GL00112.

Hofmann, Florian, Emily H. G. Cooperdock, A. Joshua West, Dominic Hildebrandt, Kathrin Strößner, and Kenneth A. Farley. 2021. "Exposure Dating of Detrital Magnetite Using 3He Enabled by MicroCT and Calibration of the Cosmogenic 3He Production Rate in Magnetite." Preprint. Cosmogenic nuclide dating. https://doi.org/10.5194/gchron-2021-10.

Ivy-Ochs, S, P. W. Kubik, J. Masarik, R. Wieler, L. Bruno, and C. Schluechter. 1998. "Preliminary Results on the Use of Pyroxene for 10Be Surface Exposure Dating." *Schweizerische Mineralogische Und Petrographische Mitteilungen* 78: 375–82.

Kasbohm, Jennifer, and Blair Schoene. 2018. "Rapid Eruption of the Columbia River Flood Basalt and Correlation with the Mid-Miocene Climate Optimum." *Science Advances* 4 (9): eaat8223. https://doi.org/10.1126/sciadv.aat8223.

Kelly, Meredith A., Thomas V. Lowell, Patrick J. Applegate, Fred M. Phillips, Joerg M. Schaefer, Colby A. Smith, Hanul Kim, Katherine C. Leonard, and Adam M. Hudson. 2015. "A Locally Calibrated, Late Glacial \textlesssup\textgreater10\textless/Sup\textgreaterBe Production Rate from a Low-Latitude, High-Altitude Site in the Peruvian Andes." *Quaternary Geochronology* 26 (1): 70–85. https://doi.org/10.1016/j.quageo.2013.10.007.

Klein, J., R. Middleton, and Hongqing Tang. 1982. "Modifications of an FN Tandem for

Quantitative 10Be Measurement." *Nuclear Instruments and Methods in Physics Research* 193 (3): 601–16. https://doi.org/10.1016/0029-554X(82)90258-0.

Kober, F., S. Ivy-Ochs, I. Leya, H. Baur, T. Magna, R. Wieler, and P. W. Kubik. 2005. "In Situ Cosmogenic 10Be and 21Ne in Sanidine and in Situ Cosmogenic 3He in Fe-Ti-Oxide Minerals." *Earth and Planetary Science Letters* 236 (1–2): 404–18. https://doi.org/10.1016/j.epsl.2005.05.020.

Kober, F., S. Ivy-Ochs, F. Schlunegger, H. Baur, P. W. Kubik, and R. Wieler. 2007. "Denudation Rates and a Topography-Driven Rainfall Threshold in Northern Chile: Multiple Cosmogenic Nuclide Data and Sediment Yield Budgets." *Geomorphology* 83 (1–2): 97–120. https://doi.org/10.1016/j.geomorph.2006.06.029.

Kurz, M., D. Colodner, T.W. Trull, R.B. Moore, and K. O'Brien. 1990. "Cosmic Ray Exposure Dating with in Situ Produced Cosmogenic 3He: Results from Young Hawaiian Lava Flows." *Earth and Planetary Science Letters* 97: 177–89.

Kurz, Mark D. 1986a. "In-Situ Production of Cosmogenic Terrestrial Helium and Some Applications to Geochronology." *Geochimica et Cosmochimica Acta* 50 (12): 2855–62.

———. 1986b. "Cosmogenic Helium in a Terrestrial Igneous Rock." *Nature* 320 (6061): 435–39. https://doi.org/10.1038/320435a0.

Lal, D. 1958. "Investigations of Nuclear Interactions Produced by Cosmic Rays." PhD Thesis, Bombay University.

Lal, D. 1987. "Production of 3He in Terrestrial Rocks." *Chemical Geology: Isotope Geoscience Section* 66: 89–98.

Lal, D. 1989. "An Important Source Of4He (And3He) in Diamonds." *Earth and Planetary Science Letters* 96 (1–2): 1–7. https://doi.org/10.1016/0012-821X(89)90118-0.

———. 1991. "Cosmic Ray Labeling of Erosion Surfaces: In Situ Nuclide Production Rates and Erosion Models." *Earth and Planetary Science Letters* 104 (2–4): 424–39. https://doi.org/10.1016/0012-821X(91)90220-C.

Lal, D., and B. Peters. 1967. "Cosmic Ray Produced Radioactivity on the Earth." In *Handbuch Der Physik*, Sitte, K., 551-612. Berlin: Springer.

Larsen, I.J., K.A. Farley, M.P. Lamb, and C.J. Pritchard. 2021. "Empirical Evidence for Cosmogenic 3He Production by Muons." *Earth and Planetary Science Letters*, February, 116825. https://doi.org/10.1016/j.epsl.2021.116825.

Larsen, Isaac J., Kenneth A. Farley, and Michael P. Lamb. 2019. "Cosmogenic 3He Production Rate in Ilmenite and the Redistribution of Spallation 3He in Fine-Grained Minerals." *Geochimica et Cosmochimica Acta* 265 (November): 19–31. https://doi.org/10.1016/j.gca.2019.08.025.

Lebatard, Anne Elisabeth, M. Cihat Alçiçek, Pierre Rochette, Samir Khatib, Amélie Vialet, Nicolas Boulbes, Didier L. Bourlès, et al., 2014. "Dating the Homo Erectus Bearing Travertine from Kocabaş (Denizli, Turkey) at at Least 1.1 Ma." *Earth and Planetary Science Letters* 390: 8–18. https://doi.org/10.1016/j.epsl.2013.12.031.

Licciardi, J, M Kurz, and J Curtice. 2006. "Cosmogenic 3He Production Rates from Holocene Lava Flows in Iceland." *Earth and Planetary Science Letters* 246 (3–4): 251–64. https://doi.org/10.1016/j.epsl.2006.03.016.

Licciardi, J.M., C.L. Denoncourt, and R.C. Finkel. 2008. "Cosmogenic 36Cl Production Rates from Ca Spallation in Iceland." *Earth and Planetary Science Letters* 267 (1–2): 365–77. https://doi.org/10.1016/j.epsl.2007.11.036.

Licciardi, J.M, M.D Kurz, P.U Clark, and E.J Brook. 1999. "Calibration of Cosmogenic 3He Production Rates from Holocene Lava Flows in Oregon, USA, and Effects of the Earth's Magnetic Field." *Earth and Planetary Science Letters* 172 (3–4): 261–71. https://doi.org/10.1016/S0012-821X(99)00204-6.

Lifton, Nathaniel, Tatsuhiko Sato, and Tibor J. Dunai. 2014. "Scaling in Situ Cosmogenic

Nuclide Production Rates Using Analytical Approximations to Atmospheric Cosmic-Ray Fluxes." *Earth and Planetary Science Letters* 386 (January): 149–60. https://doi.org/10.1016/j.epsl.2013.10.052.

Litherland, A E. 1980. "Ultrasensitive Mass Spectrometry with Accelerators." *Annual Review of Nuclear and Particle Science* 30 (1): 437–73. https://doi.org/10.1146/annurev.ns.30.120180.002253.

Litty, Camille, Julien Charreau, Pierre-Henri Blard, Raphael Pik, and Sébastien Nomade. 2021. "Spatial Variability of Quaternary Denudation Rates across a Volcanic Ocean Island (Santo Antão, Cape Verde) from Cosmogenic 3He." *Geomorphology* 375 (February): 107557. https://doi.org/10.1016/j.geomorph.2020.107557.

Luna, Lisa V., Bodo Bookhagen, Samuel Niedermann, Georg Rugel, Andreas Scharf, and Silke Merchel. 2018. "Glacial Chronology and Production Rate Cross-Calibration of Five Cosmogenic Nuclide and Mineral Systems from the Southern Central Andean Plateau." *Earth and Planetary Science Letters* 500 (October): 242–53. https://doi.org/10.1016/j.epsl.2018.07.034.

Lupker, M., K. Hippe, L. Wacker, F. Kober, C. Maden, R. Braucher, D. Bourlès, J.R. Vidal Romani, and R. Wieler. 2015. "Depth-Dependence of the Production Rate of in Situ 14C in Quartz from the Leymon High Core, Spain." *Quaternary Geochronology* 28 (June): 80–87. https://doi.org/10.1016/j.quageo.2015.04.004.

Lupker, Maarten, Pierre Henri Blard, Jérôme Lavé, Christian France-Lanord, Laetitia Leanni, Nicolas Puchol, Julien Charreau, and Didier Bourlès. 2012. "10Be-Derived Himalayan Denudation Rates and Sediment Budgets in the Ganga Basin." *Earth and Planetary Science Letters* 333–334: 146–56. https://doi.org/10.1016/j.epsl.2012.04.020.

Lupton, John, and David Graham. 1991. "Comment on 'A Ten-Year Decrease in the Atmospheric Helium Isotope Ratio Possibly Caused by Human Activity', by Y. Sano et Al." *Geophysical Research Letters* 18 (3): 482–85. https://doi.org/10.1029/91GL00493.

Mabry, Jennifer C., Tefang Lan, Christine Boucher, Peter G. Burnard, Matthias S. Brennwald, Ray Langenfelds, and Bernard Marty. 2015. "No Evidence for Change of the Atmospheric Helium Isotope Composition since 1978 from Re-Analysis of the Cape Grim Air Archive." *Earth and Planetary Science Letters* 428 (October): 134–38. https://doi.org/10.1016/j.epsl.2015.07.035.

Mabry, Jennifer, Tefang Lan, Pete Burnard, and Bernard Marty. 2013. "High-Precision Helium Isotope Measurements in Air." *J. Anal. At. Spectrom.* 28 (12): 1903–10. https://doi.org/10.1039/C3JA50155H.

Mamyrin, B. A., G. S. Anufriev, I. N. Kamenskii, and I. N. Tolstikhin. 1970. "Determination of the Isotopic Composition of Atmospheric Helium." *Geochemical International* 7: 498–505.

Marchetti, David W., Allen L. Stork, D. Kip Solomon, Thure E. Cerling, and Wil Mace. 2020. "Cosmogenic 3He Exposure Ages of Basaltic Flows from Miller Knoll, Panguitch Lake, Utah: Using the Alternative Isochron Approach to Overcome Low-Gas Crushes." *Quaternary Geochronology* 55 (February): 101035. https://doi.org/10.1016/j.quageo.2019.101035.

Margerison, H.R., W.M. Phillips, F.M. Stuart, and D.E. Sugden. 2005. "Cosmogenic 3He Concentrations in Ancient Flood Deposits from the Coombs Hills, Northern Dry Valleys, East Antarctica: Interpreting Exposure Ages and Erosion Rates." *Earth and Planetary Science Letters* 230 (1–2): 163–75. https://doi.org/10.1016/j.epsl.2004.11.007.

Marrero, Shasta M., Fred M. Phillips, Brian Borchers, Nathaniel Lifton, Robert Aumer, and Greg Balco. 2016. "Cosmogenic Nuclide Systematics and the CRONUScalc Program." *Quaternary Geochronology* 31: 160–87. https://doi.org/10.1016/j.quageo.2015.09.005.

Martin, L. C.P., P.-H. Blard, G. Balco, J. Lavé, R. Delunel, N. Lifton, and V. Laurent. 2017. "The CREp Program and the ICE-D Production Rate Calibration Database: A Fully Parameterizable and Updated Online Tool to Compute Cosmic-Ray Exposure Ages."

Quaternary Geochronology 38: 25–49. https://doi.org/10.1016/j.quageo.2016.11.006.

Martin, L.C.P., P.-H. Blard, J. Lavé, R. Braucher, M. Lupker, T. Condom, J. Charreau, V. Mariotti, and E. Davy. 2015. "In Situ Cosmogenic 10Be Production Rate in the High Tropical Andes." *Quaternary Geochronology* 30 (March 2016): 54–68. https://doi.org/10.1016/j.quageo.2015.06.012.

Martin, L.C.P., P.-H. Blard, J. Lavé, V. Jomelli, J. Charreau, T. Condom, M. Lupker, et al., 2020. "Antarctic-like Temperature Variations in the Tropical Andes Recorded by Glaciers and Lakes during the Last Deglaciation." *Quaternary Science Reviews* 247 (November): 106542. https://doi.org/10.1016/j.quascirev.2020.106542.

Martin, Léo C. P., Pierre-Henri Blard, Jérôme Lavé, Thomas Condom, Mélody Prémaillon, Vincent Jomelli, Daniel Brunstein, et al., 2018. "Lake Tauca Highstand (Heinrich Stadial 1a) Driven by a Southward Shift of the Bolivian High." *Science Advances* 4 (8): eaar2514. https://doi.org/10.1126/sciadv.aar2514.

Marty, B., and A. Jambon. 1987. "C3He in Volatile Fluxes from the Solid Earth: Implications for Carbon Geodynamics." *Earth and Planetary Science Letters* 83 (1–4): 16–26. https://doi.org/10.1016/0012-821X(87)90047-1.

Matsuda, J., T. Matsumoto, H. Sumino, K. Nagao, J. Yamamoto, Y. Miura, I. Kaneoka, N. Takahata, and Y. Sano. 2002. "The 3He/4He Ratio of New Internal He Standard of Japan (HESJ)." *Geochemical Journal* 36 (2): 191–95. https://doi.org/10.2343/geochemj.36.191.

Matsumoto, Takuya, Jun-Ichi Matsuda, Igor Yatsevich, and Minoru Ozima. 2010. "Noble Gas Mass Spectrometry with a Compressor Driven Recycling System for Improved Sensitivity." *GEOCHEMICAL JOURNAL* 44 (3): 167–72. https://doi.org/10.2343/geochemj.1.0055.

Medynski, S., R. Pik, P. Burnard, S. Dumont, R. Grandin, A. Williams, P.-H. Blard, et al., 2016. "Magmatic Cycles Pace Tectonic and Morphological Expression of Rifting (Afar Depression, Ethiopia)." *Earth and Planetary Science Letters* 446: 77–88. https://doi.org/10.1016/j.epsl.2016.04.014.

Megrue, G. H. 1967. "Isotopic Analysis of Rare Gases with a Laser Microprobe." *Science* 157 (3796): 1555–56. https://doi.org/10.1126/science.157.3796.1555.

———. 1971. "Distribution and Origin of Helium, Neon, and Argon Isotopes in Apollo 12 Samples Measured by in Situ Analysis with a Laser-Probe Mass Spectrometer." *Journal of Geophysical Research* 76 (20): 4956–68. https://doi.org/10.1029/JB076i020p04956.

Min, Kyoungwon, Peter W. Reiners, John a. Wolff, Roland Mundil, and R. Lee Winters. 2006. "(U–Th)/He Dating of Volcanic Phenocrysts with High-U–Th Inclusions, Jemez Volcanic Field, New Mexico." *Chemical Geology* 227 (3–4): 223–35. https://doi.org/10.1016/j.chemgeo.2005.10.006.

Muscheler, Raimund, Jürg Beer, Peter W. Kubik, and H.-A. Synal. 2005. "Geomagnetic Field Intensity during the Last 60,000 Years Based on 10Be and 36Cl from the Summit Ice Cores and 14C." *Quaternary Science Reviews* 24 (16–17): 1849–60. https://doi.org/10.1016/j.quascirev.2005.01.012.

Nesterenok, A. V., and O. V. Yakubovich. 2016. "Production of 3He in Rocks by Reactions Induced by Particles of the Nuclear-Active and Muon Components of Cosmic Rays: Geological and Petrological Implications." *Petrology* 24 (1): 21–34. https://doi.org/10.1134/S0869591116010057.

Niedermann, S. 2002. "Cosmic-Ray-Produced Noble Gases in Terrestrial Rocks: Dating Tools for Surface Processes." *Reviews in Mineralogy and Geochemistry* 47 (1): 731–84. https://doi.org/10.2138/rmg.2002.47.16.

Niedermann, S, J Schaefer, R Wieler, and R Naumann. 2007. "The Production Rate of Cosmogenic 38Ar from Calcium in Terrestrial Pyroxene." *Earth and Planetary Science Letters* 257 (3–4): 596–608. https://doi.org/10.1016/j.epsl.2007.03.020.

Nishiizumi, K., J. Klein, R. Middleton, and H. Craig. 1990. "Cosmogenic 10Be, 26Al and 3He

in Olivine from Maui Lavas." *Earth and Planetary Science Letters* 98 (3–4): 263–66. https://doi.org/10.1016/0012-821X(90)90028-V.

Pacini, Domenico, translated, commented by Michela De Maria, and Alessandro De Angelis. 1911. "Penetrating Radiation on the Sea." *ArXiv:1101.3015 [Astro-Ph, Physics:Physics]*. http://arxiv.org/abs/1101.3015.

Parman, S. W. 2007. "Helium Isotopic Evidence for Episodic Mantle Melting and Crustal Growth." *Nature* 446 (7138): 900–903. https://doi.org/10.1038/nature05691.

Pigati, Jeffrey S, Nathaniel A Lifton, A J Timothy Jull, and Jay Quade. 2010. "A Simplified in Situ Cosmogenic ^{14}C Extraction System." *Radiocarbon* 52 (3): 1236–43. https://doi.org/10.1017/S0033822200046324.

Protin, Marie, Pierre Henri Blard, Yves Marrocchi, and François Mathon. 2016. "Irreversible Adsorption of Atmospheric Helium on Olivine: A Lobster Pot Analogy." *Geochimica et Cosmochimica Acta* 179: 76–88. https://doi.org/10.1016/j.gca.2016.01.032.

Puchol, Nicolas, Pierre Henri Blard, Raphaël Pik, Bouchaïb Tibari, and Jérôme Lavé. 2017. "Variability of Magmatic and Cosmogenic3He in Ethiopian River Sands of Detrital Pyroxenes: Impact on Denudation Rate Determinations." *Chemical Geology* 448: 13–25. https://doi.org/10.1016/j.chemgeo.2016.10.033.

Raisbeck, G.M., F. Yiou, D. Bourlès, J. Lestringuez, and D. Deboffle. 1987. "Measurements of 10Be and 26Al with a Tandetron AMS Facility." *Nuclear Instruments and Methods in Physics Research Section B: Beam Interactions with Materials and Atoms* 29 (1–2): 22–26. https://doi.org/10.1016/0168-583X(87)90196-0.

Ramalho, Ricardo S., Gisela Winckler, José Madeira, George R. Helffrich, Ana Hipólito, Rui Quartau, Katherine Adena, and Joerg M. Schaefer. 2015. "Hazard Potential of Volcanic Flank Collapses Raised by New Megatsunami Evidence." *Science Advances* 1 (9): e1500456. https://doi.org/10.1126/sciadv.1500456.

Ritz, J. F., A. Avagyan, M. Mkrtchyan, H. Nazari, P. H. Blard, A. Karakhanian, H. Philip, et al., 2016. "Active Tectonics within the NW and SE Extensions of the Pambak-Sevan-Syunik Fault: Implications for the Present Geodynamics of Armenia." *Quaternary International* 395: 61–78. https://doi.org/10.1016/j.quaint.2015.05.021.

Sano, Yuji, Yukiko Furukawa, and Naoto Takahata. 2010. "Atmospheric Helium Isotope Ratio: Possible Temporal and Spatial Variations." *Geochimica et Cosmochimica Acta* 74 (17): 4893–4901. https://doi.org/10.1016/j.gca.2010.06.003.

Sano, Yuji, Taichi Tokutake, and Naoto Takahata. 2008. "Accurate Measurement of Atmospheric Helium Isotopes." *Analytical Sciences : The International Journal of the Japan Society for Analytical Chemistry* 24 (4): 521–25. https://doi.org/10.2116/analsci.24.521.

Sartégou, Amandine, Pierre-Henri Blard, Régis Braucher, Didier L. Bourlès, Patrick Sorriaux, Laurent Zimmermann, Alexis Laffitte, et al., 2020. "Late Cenozoic Evolution of the Ariège River Valley (Pyrenees) Constrained by Cosmogenic 26Al/10Be and 10Be/21Ne Dating of Cave Sediments." *Geomorphology* 371 (December): 107441. https://doi.org/10.1016/j.geomorph.2020.107441.

Scarsi, Paolo. 2000. "Fractional Extraction of Helium by Crushing of Olivine and Clinopyroxene Phenocrysts: Effects on the 3He/4He Measured Ratio." *Geochimica et Cosmochimica Acta* 64 (21): 3751–62. https://doi.org/10.1016/S0016-7037(00)00419-1.

Schaefer, Joerg M., Gisela Winckler, Pierre-Henri Blard, Greg Balco, David L. Shuster, Ronny Friedrich, A.J.T. Jull, Rainer Wieler, and Christian Schluechter. 2016. "Performance of CRONUS-P – A Pyroxene Reference Material for Helium Isotope Analysis." *Quaternary Geochronology* 31 (February): 237–39. https://doi.org/10.1016/j.quageo.2014.07.006.

Schäfer, Jörg M., Susan Ivy-Ochs, Rainer Wieler, Ingo Leya, Heinrich Baur, George H. Denton, and Christian Schlüchter. 1999. "Cosmogenic Noble Gas Studies in the Oldest Landscape on Earth: Surface Exposure Ages of the Dry Valleys, Antarctica." *Earth and Planetary Science*

Letters 167 (3–4): 215–26. https://doi.org/10.1016/S0012-821X(99)00029-1.

Schiffer, Markus, Alexander Stolz, Damián Alejandro López, Richard Spanier, Susan Herb, Claus Müller-Gatermann, Stefan Heinze, et al., 2020. "Method Developments for Accelerator Mass Spectrometry at CologneAMS, 53Mn/3He Burial Dating and Ultra-Small 14CO2 Samples." *Global and Planetary Change* 184 (January): 103053. https://doi.org/10.1016/j.gloplacha.2019.103053.

Schimmelpfennig, Irene, Lucilla Benedetti, Robert Finkel, Raphaël Pik, Pierre Henri Blard, Didier Bourlès, Pete Burnard, and Alice Williams. 2009. "Sources of In-Situ 36Cl in Basaltic Rocks. Implications for Calibration of Production Rates." *Quaternary Geochronology* 4 (6): 441–61. https://doi.org/10.1016/j.quageo.2009.06.003.

Schimmelpfennig, Irene, Alice Williams, Raphaël Pik, Pete Burnard, Samuel Niedermann, Robert Finkel, Björn Schneider, and Lucilla Benedetti. 2011. "Inter-Comparison of Cosmogenic in-Situ 3He, 21Ne and 36Cl at Low Latitude along an Altitude Transect on the SE Slope of Kilimanjaro Volcano (3°S, Tanzania)." *Quaternary Geochronology* 6 (5): 425–36. https://doi.org/10.1016/j.quageo.2011.05.002.

Shuster, David L, Kenneth a Farley, Janet M Sisterson, and Donald S Burnett. 2004. "Quantifying the Diffusion Kinetics and Spatial Distributions of Radiogenic 4He in Minerals Containing Proton-Induced 3He." *Earth and Planetary Science Letters* 217 (1–2): 19–32. https://doi.org/10.1016/S0012-821X(03)00594-6.

Shuster, David L., Kenneth A. Farley, Paulo M. Vasconcelos, Greg Balco, Hevelyn S. Monteiro, Kathryn Waltenberg, and John O. Stone. 2012. "Cosmogenic 3He in Hematite and Goethite from Brazilian 'Canga' Duricrust Demonstrates the Extreme Stability of These Surfaces." *Earth and Planetary Science Letters* 329–330 (May): 41–50. https://doi.org/10.1016/j.epsl.2012.02.017.

Stone, J. O. 2000. "Air Pressure and Cosmogenic Isotope Production." *Journal of Geophysical Research-Solid Earth* 105 (B10): 23753–59. https://doi.org/10.1029/2000JB900181.

Tremblay, Marissa M., David L. Shuster, and Greg Balco. 2014. "Diffusion Kinetics of 3He and 21Ne in Quartz and Implications for Cosmogenic Noble Gas Paleothermometry." *Geochimica et Cosmochimica Acta* 142: 186–204. https://doi.org/10.1016/j.gca.2014.08.010.

Trull, T.W., M.D. Kurz, and W.J. Jenkins. 1991. "Diffusion of Cosmogenic3He in Olivine and Quartz: Implications for Surface Exposure Dating." *Earth and Planetary Science Letters* 103 (1–4): 241–56. https://doi.org/10.1016/0012-821X(91)90164-D.

Uppala, S. M., P. W. Kallberg, A. J. Simmons, U. Andrae, V. D. Bechtold, M. Fiorino, J. K. Gibson, et al., 2005. "The ERA-40 Re-Analysis." *Quarterly Journal of the Royal Meteorological Society* 131 (612): 2961–3012. https://doi.org/10.1256/qj.04.176.

Vasconcelos, Paulo M., Kenneth A. Farley, John Stone, Thiago Piacentini, and L. Keith Fifield. 2019. "Stranded Landscapes in the Humid Tropics: Earth's Oldest Land Surfaces." *Earth and Planetary Science Letters* 519 (August): 152–64. https://doi.org/10.1016/j.epsl.2019.04.014.

Vermeesch, Pieter. 2018. "IsoplotR: A Free and Open Toolbox for Geochronology." *Geoscience Frontiers* 9 (5): 1479–93. https://doi.org/10.1016/j.gsf.2018.04.001.

Vermeesch, Pieter, Greg Balco, Pierre-Henri Blard, Tibor J. Dunai, Florian Kober, Samuel Niedermann, David L. Shuster, et al., 2015. "Interlaboratory Comparison of Cosmogenic 21 Ne in Quartz." *Quaternary Geochronology* 26 (February): 20–28. https://doi.org/10.1016/j.quageo.2012.11.009.

Williams, A.J., F.M. Stuart, S.J. Day, and W.M. Phillips. 2005. "Using Pyroxene Microphenocrysts to Determine Cosmogenic 3He Concentrations in Old Volcanic Rocks: An Example of Landscape Development in Central Gran Canaria." *Quaternary Science Reviews* 24 (1–2): 211–22. https://doi.org/10.1016/j.quascirev.2004.07.004.

Wittmann, H., and F. von Blanckenburg. 2009. "Cosmogenic Nuclide Budgeting of Floodplain Sediment Transfer." *Geomorphology* 109 (3–4): 246–56.

https://doi.org/10.1016/j.geomorph.2009.03.006.

Wolf, R A, K A Farley, and D M Kass. 1998a. "Modeling of the Temperature Sensitivity of the Apatite ž U–Th/ RHe Thermochronometer," 10.

Wolf, R.A, K.A Farley, and D.M Kass. 1998b. "Modeling of the Temperature Sensitivity of the Apatite (U–Th)/He Thermochronometer." *Chemical Geology* 148 (1–2): 105–14. https://doi.org/10.1016/S0009-2541(98)00024-2.

Wood, Bernard J., Jonathan D. Blundy, and J.Andrew C. Robinson. 1999. "The Role of Clinopyroxene in Generating U-Series Disequilibrium during Mantle Melting." *Geochimica et Cosmochimica Acta* 63 (10): 1613–20. https://doi.org/10.1016/S0016-7037(98)00302-0.

Yokochi, Reika, Bernard Marty, Raphaël Pik, and Pete Burnard. 2005. "High 3 He/ 4 He Ratios in Peridotite Xenoliths from SW Japan Revisited: Evidence for Cosmogenic 3 He Released by Vacuum Crushing." *Geochemistry, Geophysics, Geosystems* 6 (1): n/a-n/a. https://doi.org/10.1029/2004GC000836.

York, D. 1966. "Least-Squares Fitting of a Straight Line." *Canadian Journal of Physics* 44: 1079–86.

Zeitler, Peter K. 2014. "U-Th/He Dating." In *Encyclopedia of Scientific Dating Methods*, edited by W. Jack Rink and Jeroen Thompson, 1–14. Dordrecht: Springer Netherlands. https://doi.org/10.1007/978-94-007-6326-5_131-1.

Zerathe, Swann, Pierre-Henri Blard, Régis Braucher, Didier Bourlès, Laurence Audin, Julien Carcaillet, Fabrizio Delgado, Carlos Benavente, Georges Aumaître, and Karim Keddadouche. 2017. "Toward the Feldspar Alternative for Cosmogenic 10Be Applications." *Quaternary Geochronology* 41 (August): 83–96. https://doi.org/10.1016/j.quageo.2017.06.004.

Ziegler, James F., M.D. Ziegler, and J.P. Biersack. 2010. "SRIM – The Stopping and Range of Ions in Matter (2010)." *Nuclear Instruments and Methods in Physics Research Section B: Beam Interactions with Materials and Atoms* 268 (11–12): 1818–23. https://doi.org/10.1016/j.nimb.2010.02.091.

Ziegler, J.F. 1977. *Helium: Stopping Powers and Ranges in All Elemental Matter*. Pergamon Press.

Zimmermann, Laurent, Guillaume Avice, Pierre-Henri Blard, Bernard Marty, Evelyn Füri, and Peter G. Burnard. 2018. "A New All-Metal Induction Furnace for Noble Gas Extraction." *Chemical Geology* 480 (March): 86–92. https://doi.org/10.1016/j.chemgeo.2017.09.018.

Zimmermann, Laurent, and David Bekaert. 2020. "Analyse des gaz rares par spectrométrie de masse statique - Théorie et instrumentation," 30.